Holographic Imaging and Iterative Phase Optimization Methods for Focusing and Transmitting Light in Scattering Media

by
Michael James Purcell

A dissertation submitted in partial fulfillment
of the requirements for the degree of
Doctor of Philosophy
(Applied Physics)
in the University of Michigan
2016

Doctoral Committee
Professor Stephen C. Rand, Chair
Professor Cagliyan Kurdak
Professor Vasudevan Lakshminarayanan, University of Waterloo
Professor Mary-Ann Mycek
Associate Professor Jennifer P. Ogilvie

Dedication

This is for you, Mom and Dad. Thanks for teaching me the value of education. Dad, don't stop trying to prove Einstein wrong. You'll get him.

Acknowledgements

I would like to gratefully acknowledge the following sources of support that made this dissertation possible:

Dr. Stephen Rand for his financial support, guidance, and patience during my research and writing, for helping to prepare me for my defense, and for serving as committee chairperson.

Dr. Manish Kumar for his hands-on guidance and research contributions and for providing his extensive expertise in holography.

My labmates Elizabeth Cloos, Alex Fisher, and Theresa Chick for all of the helpful discussions.

My committee members for their time and patience: Doctors Vasudevan Lakshminarayanan, Mary-Ann Mycek, Jennifer Ogilvie, and Cagliyan Kurdak.

The Applied Physics Program at the University of Michigan for giving me the opportunity to attend graduate school and providing an atmosphere of encouragement and support throughout.

Preface

The experiments and results presented in section 3 are original work which I performed with Dr. Manish Kumar, Post-Doctoral Fellow from the India Institute of Technology – Delhi, in the laboratory of Dr. Stephen Rand, Professor of Electrical Engineering at the University of Michigan. Section 3.1 is an adapted version of our paper published in JOSA A (Purcell, M.J., Kumar, M., Rand, S.C., Lakshminarayanan, V. "Holographic imaging through a scattering medium by diffuser-assisted statistical averaging," J Opt Soc Am A. 2016 Jul 1;33(7):1291) on which I am the first author.

Several figures throughout this dissertation have been reused from copyrighted materials with permission from the respective journals and authors. Acknowledgment of the source of these figures is included in each caption.

Table of Contents

List of Appendices

List of Figures

List of Acronyms

SLM – Spatial light modulator

EOM – Electro-optical modulator

CCD – Charge coupled device

OPC – Optical phase conjugation

DOPC – Digital optical phase conjugation

OPSL – Optically pumped semiconductor laser

SNR – Signal to noise ratio

CW – Continuous wave

EMCCD – Electron multiplying charge coupled device

AO – Adaptive optics

FWHM – Full-width half max

CBS – Coherent backscattering

SSIM – Structural similarity index

MSSIM – Mean structural similarity index

Abstract

Existing methods for focusing and imaging through strongly scattering materials are often limited by speed, the need for invasive feedback, and the shallow depth of penetration of photons into the material. These limitations have motivated the present research into the development of a new iterative phase optimization method for improving transmission of light through a sample of strongly scattering material. A new method, based on the detection of back-scattered light combined with active (phase-only) wavefront control was found to be partially successful, decreasing the power of backscattered incident light at 488 nm wavelength by approximately 35% in a 626 μm thick sample of Yttria (Y_2O_3) nanopowder (mean particle size 26 nm) in clear epoxy with transport mean free path length ~116 μm. However, the observed transmitted power did not show simultaneous improvement. The conclusion was reached that scattering to the sides of the sample and polarization scrambling were responsible for the lack of improved transmission with this method. Some ideas for improvement are discussed in the thesis. This research subsequently led to the development of a lensless holographic imaging method based on a rotating diffuser for statistical averaging of the optical signal for overcoming speckle caused by reflection from a rough surface. This method made it possible to reduce background variations of intensity due to speckle and improve images reflected from rough, immobile surfaces with no direct path for photons between the object and camera. Improvements in the images obtained with this technique were evaluated quantitatively by comparing SSIM indices and were found to offer practical advances for transmissive and reflective geometries alike.

Chapter 1: Introduction

1.1 Overview

In disordered or highly scattering media, attempts to use electromagnetic waves at optical wavelengths for imagery are met with serious challenges. The one-to-one correspondence necessary to relate input to output in practical imagery applications cannot be preserved unless the path of photons through the system is predictable. Generally speaking, when the straight line (ballistic) path through a scattering medium is disrupted by random scattering events, predictable propagation, focusing and imaging of light is expected to be severely hampered. Optical wavelengths of light have been very useful for applications in many materials that disrupt the one-to-one relationship between input and output of the optical system, including multiple types of biological tissues, turbulent atmosphere, ground glass diffusers, and many others.

Imaging deep within body tissue is important for observing objects such as tumors [1], [2]. Focusing optical wavelengths at these depths may contribute to the development of treatment techniques such as thermal ablation of cancerous cells, without the added risk of ionizing radiation [3]. However the propagation of light in tissues must be corrected when precise focusing and imaging is needed. This requires wavefront control of one form or another, a topic that usually involves adaptive optics (in the form of a deformable mirror) or phase modulators (such as a reflective spatial light modulator, which controls the phase of reflected light). An early example of adaptive optics was the invention of the laser ‘guide star’ concept which was introduced to assist astronomers in observing celestial bodies. It operated by creating a point source of light above the atmosphere, measuring the distorted image of the point at the earth’s surface, and applying corrections to deformable mirrors that corrected the distortion in real time. By applying the same corrections to a deformable telescope mirror, high resolution imagery through the atmosphere became possible. The use of a laser ‘guide star’ is a method of adaptive

optics which is assisting astronomers in observing celestial bodies by understanding and correcting for the effects of the turbulent atmosphere on photons traveling to earth [4]. Although the atmosphere's effects on the viewing of celestial bodies are mainly the result of refraction (not scattering), the guide star concept has been demonstrated as an equally effective technique in strongly scattering biological tissues. Military applications of adaptive optics include the use of directed energy weapons which can experience significant scintillation effects due to turbulence in the atmosphere [5], imaging through smoke [6], and optical communications [7]. Another important application of optical imaging through scattering media is in the area of fluorescence mapping of brain functions. Recent work allows imaging of neurons directly through the skulls of rodents [8]–[10].

Several advances in the area of focusing and imaging in disordered media will be discussed in Chapter 2, such as the use of optical phase conjugation [11], [12], guide stars [4], wavefront phase optimization [13]–[15], and time-reversed ultrasonic encoding (TRUE) [1], [16]. Though there are many more techniques than could be effectively discussed here, these developments have been selected for their relevance to the new results within this dissertation. Introductory materials of this dissertation conclude at the end of Chapter 2.

Despite the proliferation of many sophisticated methods for focusing and imaging in strongly scattering media [1], [4], [13], [16], there is no technique that is without limitations. For example, some methods of focusing are effective in materials with relatively static scattering centers and may require several minutes or longer to achieve the desired result. These same methods may be impractical in highly dynamic environments in which the persistence time of scattering centers is on the order of milliseconds. Living biological tissues and smoke drifting through the atmosphere are good examples of such a dynamic environment. A practical method of focusing or transmitting light in these and other dynamic scattering media would therefore need to be capable of converging to a solution within milliseconds. As another example, some methods require feedback from within or behind the scattering material to determine the effect of control methods on the desired application (a 'guide star' for atmospheric applications; a "beacon" for in vivo applications), but feedback from such locations is not always practical to collect.

With such limitations in mind, in order to expand the availability of focusing and imaging methods to ever-broader circumstances, it is necessary to continue finding new ways to build on previous methods for focusing and imaging in scattering media. In this dissertation, the results of three experiments (one of which is a type of lensless Fourier transform holographic imaging, and the other two wavefront phase optimization methods) are presented. Each of the experiments described in Chapter 3 expands upon previously published focusing and imaging methods for scattering media.

In Section 3.1, lensless holographic imaging is demonstrated in reflection from a disordered reflecting surface with the assistance of statistical averaging by using a rotating diffuser [17]. This experiment is also an extension of a previously demonstrated technique in which holographic imaging was demonstrated in reflection from a disordered reflecting surface [18]; however, in the original experiment, the statistical averaging was accomplished by small vibrations of the reflecting surface. In order to extend this method for use in realistic scenarios in which the reflecting surface is something which cannot be easily moved, such as a wall, the statistical averaging was accomplished by moving a diffuser at a location in the experimental setup that was physical separated from the reflecting surface [17]. This is a novel and practical way of statistical averaging which makes use of a rotating ground glass diffuser to nullify the adverse effects caused by speckle introduced by a first static diffuser / aberrator [17], [19]. The approach is a Fourier transform-based, holographic approach which demonstrates the ability to recover detailed images and shows promise for further remarkable improvement [17], [19]. The present experiments were performed with 2D flat images, but this method could be easily adapted for recovery of 3D extended object information [17], [19]. The simplicity of the approach makes it fast, reliable, and potentially scalable as a portable technology [17], [19]. Since imaging through a diffuser has direct applications in biomedicine and defense technologies this method may augment advanced imaging capabilities in many fields [17], [19].

Section 3.2 covers a major portion of the research effort that was dedicated to enhancing the amount of light transmitted through thin samples of strongly scattering media by iterative wavefront phase optimization. This experiment differed from previously published experiments

which made use of wavefront phase optimization by providing a means of addressing the phases of every spatial mode of the incident wavefront at the same time, creating the potential for a much faster system capable of keeping pace with the changes within a dynamic scattering sample. It combines this rapid optimization method with a robust feedback control loop which only requires data from backscattered light which can always be conveniently collected. The speed and robustness of such a method may increase the utility of focusing and imaging techniques in situations which involve a dynamic scattering sample and those in which the collection of feedback from within the sample is considered invasive or is impractical. The results of this experiment show that a significant decrease in measured backscattered light was achieved, although there was no measurable increase in transmitted light. Despite the latter, these results show that the effects of the system's scattering matrix on the incident light were controlled in a predictable manner, and with future research this may still lead to enhanced transmission.

In another new result presented in Section 3.3, wavefront phase optimization was again used to focus coherent light backscattered from an illuminated sample. The light was focused to an arbitrarily selected spot within the backscattered speckle pattern, resulting in a significant increase in the power delivered to the focal point. This was an expansion upon the results of a previous experiment published in 2007 by I.M. Vellekoop and A.P. Mosk, in which light was focused within and through a disordered, strongly scattering medium by a similar method of phase optimization [13].

Principles of holography were used extensively in these experiments. The discussion of Section 3.1 is based on lensless Fourier transform holographic imaging. In Section 3.2, the wavefront optimization method for transmission enhancement makes use of digital optical phase conjugation (DOPC) which requires the recording and reproduction of a wavefront by holographic means. Due to the importance of holography in these experiments, it is essential to understand the underlying principles of holography in order to fully understand the methods used for each. In order to facilitate a more complete understanding of the experiments, a brief review of these principles follows this introduction in Section 1.2.

Finally, Chapter 4 lays out a summary of the contributions of the three new experimental results and a discussion of potential future work.

1.2 Review of Holographic Principles

Holography is a critical component in many of the experiments in the field of imaging through strongly scattering media and within this thesis. In the imaging experiment discussed in Section 3.1, the setup is a form of lensless Fourier transform holographic imaging. In addition, phase-shifting digital holography was used extensively to record the phase of backscattered wavefronts in the transmission enhancement experiment discussed in Section 3.2. In order to foster a deeper understanding of these two experiments, a brief review of the principles of holography is first presented here.

A review of holography would not be complete without mentioning both Dennis Gabor, the inventor of holography [20], and Emmett Leith and Juris Upatnieks [21], who ushered holography into modern times with critical advancements in the field.

Dennis Gabor proposed in 1948 that an object could be imaged using coherent light by "wavefront reconstruction" [22]. What Gabor meant by this is that when an object is illuminated with coherent light, the light scattered from the object produces a complex wavefront that can be defined at a location in space by its amplitude and phase. These pieces of information completely describe the image forming properties of the light. Re-creating this wavefront's amplitude and phase information at the same location would therefore result in an image of the original object even without the presence of the object, when observed from the proper angle.

Although Gabor called this technique "wavefront reconstruction", today it is commonly known as "holography", which comes from the concept of "complete imaging" [22]. Holography grew rapidly as a field of study and is now an integral concept in imaging systems for applications from entertainment to microscopy [22]. This brief review of holography is intended to set the stage for its use in two different experimental methods discussed in later sections.

$$a(x,y) = |a(x,y)|e^{i\psi(x,y)} \tag{1}$$

$$A(x,y) = |A(x,y)|e^{i\phi(x,y)} \tag{2}$$

The essence of holography is to record the phase and amplitude of a wavefront produced by coherent light scattered from an object intended to be imaged. This involves the use of interferometry between the object wave and a coherent reference wave, described by equations (1) and (2), respectively. Both the object wave and the reference wave originate from the same coherent light source.

1.1.1 Recording a Gabor Hologram

Gabor's original method of recording the phase and amplitude of this wavefront involved the use of an emulsion that absorbs the energy from incident light, altering its transmission properties [22]. Initially it may appear that the information encoded into the emulsion is only amplitude data. However, with the use of a reference wave with known amplitude and phase an interference pattern can be created between the reference and the source that combines the amplitude and phase information of the source [22].

In the original holograms created by Gabor, the source also formed the reference wave in "on-axis" geometry. In Gabor's original geometry, the light from a point source object is collimated

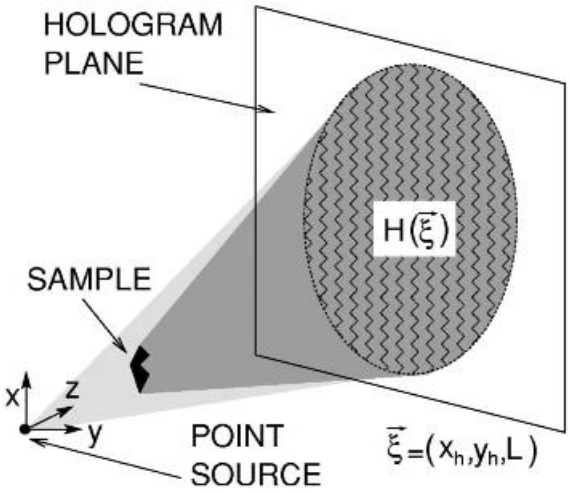

Figure 1. (Repetto *et al.*, 2004) Schematic of the Gabor hologram geometry. Reproduced from Repetto L, Pellistri F, Piano E, Pontiggia C. Gabor's hologram in a modern perspective. Am J Phys. 2004;72(7):964, with the permission of the American Association of Physics Teachers.

by a lens before illuminating a transmissive image object, as in figure 1 [22], [23]. Because the image object has a DC level of transmission, there is a uniform plane wave that passes through the object along with the amplitude modulated wave. The uniform plane wave serves as a reference wave to record the hologram of the object at the recording plane.

The interference between the reference and source is described by equation 3. The relationship between the transmission of the recording and its exposure to light is described by equation 4.

$$I(x,y) = |A(x,y)|^2 + |a(x,y)|^2 + \frac{1}{2}|A(x,y)||a(x,y)|\cos[\phi(x,y) - \psi(x,y)] \quad (3)$$

$$T = T_0 + \beta(a^*a + A^*a + Aa^*) \quad (4)$$

It is important to note that the coefficient β governs the slope of the transmission versus exposure curve [22]. Typically, β is chosen at a point on the curve where the slope is linear [22]. When a reference wave is applied to the holographic recording (passes through the recording), its phase and amplitude are modulated by multiplying by the transmission *T* listed in equation 4. The four terms on the right side of the equation bear evaluation. The T_0 exposure term is a result of the intensity of the reference wave (assumed constant over the recording surface) [22]. This term adds no information to the recording (beyond noise) and is therefore ignored henceforth. The second term in this series of terms is proportional to the intensity of the original object wave, but it contains none of the phase information that defines the original wavefront from the object. It also contributes noise to the image reconstruction, but not necessarily uniform noise [22].

The terms of interest are the final two. The third term is proportional to the original wavefront. The amplitude of the reference wave is assumed to be constant over the recording plane, which means that this term is essentially a "copy" of the original wavefront produced by the object [22]. An observer from the +z direction along the optical axis would see a wavefront that appears to be diverging from the original object, from the –z side of the recording. This makes the image a virtual image.

The final term is proportional to the phase conjugate of the object wavefront. This term refers to a wavefront that converges at a distance z_0 on the +z side of the recording. When observed from the +z direction, this wavefront forms a real image [22].

All of these terms refer to wavefronts that travel in the +z direction along the optical axis, so that an observer would see both the virtual image and the real image overlapping with two noise terms. This can make the images difficult to retrieve. For this reason, a different geometry for holographic recording and reconstruction was developed which allowed the two images and the noise terms to be separated from each other. This geometry (known as "off-axis" holography) will be discussed briefly in the next section.

Since the relationship between transmission and exposure is linear for the two terms of interest, the fields at each transverse coordinate location at the recording plane can be understood as a linear superposition of the contributions of many point sources [22]. Each image object can be considered a collection of point sources, so that the contribution of all of these points at a given location can be found by integrating over the image object. For this reason, it is only necessary to first consider a point source image object in order to understand the holographic recording as it applies to extended objects.

1.1.2 Off-Axis Holography

The discovery of a geometry that would allow the four terms of the holographic reconstruction to be easily separated from one another is credited to Emmett Leith and Kelly Upatnieks (14). Rather than use a reference wave that also passed through the object, the reference was placed at an angle from the optical axis. Using a plane wave as a reference, this imparts a phase to the reference wave as it strikes the recording plane that is a function of the transverse coordinate lying within the plane defined by the optical axis of the system and the k-vector of the plane wave [22].

$$\vec{k} = \frac{2\pi}{\lambda}\,(\hat{x}\sin\theta + \hat{z}\cos\theta) \tag{5}$$

$$A(x,y) = |A_0|\exp(ikx\sin(\theta) + i\phi) \tag{6}$$

Now consider the light from a point source. Mathematically, it can be described at a particular location in space by equation 7, where a_0 is the complex amplitude of the source, z is the position along the optical axis, x and y are transverse coordinates at z, and x_0 and y_0 are the transverse coordinates at the position of the point source.

$$a(x,y,z) = a_0 e^{ik_0\sqrt{z^2+(x-x_0)^2+(y-y_0)^2}} \tag{7}$$

$$I(x,y) = |a_0|^2 + |A_0|^2 + \frac{1}{2}|a||A|\cos(k(x\sin\theta - \psi)) \tag{8}$$

The expanding spherical wave from the point object has a phase spatial frequency at the recording plane that increases in magnitude as a function of the radial distance from the optical axis [22].

1.1.3 Lensless Fourier Transform Holography

In this geometry, a point source is again used to provide a reference which interferes with light from the object source. The term "lensless" here does not mean that no lenses may be used in the setup (in fact it will be shown that several lenses were used to perform this type of holography for one of the experiments upon which this dissertation is focused). This term refers to the fact that no collimation of the reference or the object waves is required to produce the interference pattern which contains all of the information about the hologram [22]. The information that is stored in the interference pattern is in frequency space, and must be Fourier-transformed in order to produce the object image. Before the advent of CCD camera sensors, the holographic recording was accomplished by exposing a light-sensitive substrate to the interference pattern, as mentioned above, and the wavefront that results from passing the point source reference through

this recording was transformed using a lens [22]. In modern times, the recording is typically accomplished using a digital camera sensor and the Fourier transform is performed programmatically. This is the method employed in the holographic imaging experiment discussed in section 3.1.

Chapter 2: Recent Advances in Focusing and Imaging Through Scattering Media

In this section, several experiments representing the cutting edge of knowledge in the area of focusing and imaging in the presence of disordered media are reviewed. The area of optics dealing with focusing and imaging in the presence of scattering media is large, and a small sampling of the work in this area cannot cover every type of technique that has been developed. This small sample of experiments represent three areas of particular interest to the author and with relevance to the new experiments presented in later sections, but by no means are they the only relevant works.

The experiments reviewed here are divided into three categories: wavefront optimization in 2.1, optical phase conjugation in 2.2, and guide stars for astronomy and biomedical imaging in 2.3. The purpose of this section is to give a brief offering of the many types of focusing and imaging techniques that have recently been developed while pointing out that each of these methods has a limitation of some kind. Since there is no single method of focusing and imaging in scattering media that is effective in every conceivable scenario, there is room to build on almost every experimental result that has been published. Despite the proliferation of sophisticated methods, this section serves to help motivate the new research presented in section 3 which builds upon previously published results in holographic imaging, focusing, and enhancing transmission of light in strongly scattering media.

The wavefront phase optimization methods used in the experiments discussed in 2.1 are very closely related to the new research presented in 3.2 and 3.3 in particular. The work published by Vellekoop and Mosk in 2007 which used sequential wavefront phase optimization for focusing in a strongly scattering sample was a jumping off point for the new research presented here [13].

Limitations of the 2007 work by Vellekoop and Mosk are specifically addressed by the research presented in 3.2, including the speed of convergence to a solution using wavefront optimization methods and the invasive nature of the feedback needed for the methods of Vellekoop and Mosk in their work [13].

2.1 Focusing With Wavefront Control

Scattering events limit the ballistic movement of photons to about one mean free transport length within a sample of strongly scattering material. The disruption of ballistic photon trajectories is what makes these materials appear opaque. Imaging and focusing with ballistic photons is therefore limited to about one mean free transport length. A landmark advancement for focusing and imaging in the presence of a scattering material that is composed of randomly distributed, closely packed scattering centers (body tissue, as one example) is an experiment that demonstrates the ability to focus through a sample by "shaping" a wavefront of incident light using a phase delay mechanism, as shown in figure 2 [13]. The experiment in question was discussed in a 2007 paper by Vellekoop and Mosk [13]. While previous work suggested the

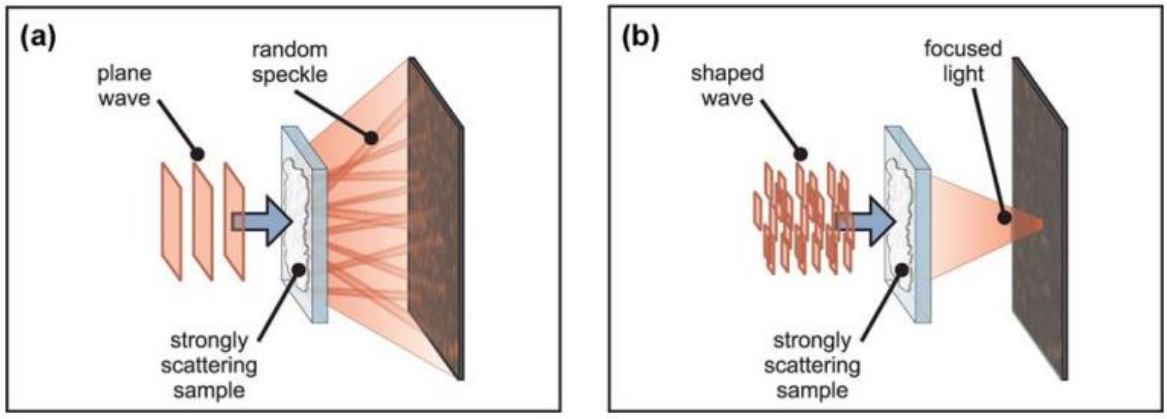

Figure 2. (Vellekoop and Mosk, 2007) Design of the experiment. (a) A plane wave is focused on a disordered medium, and a speckle pattern is transmitted. (b) The wavefront of the incident light is shaped so that scattering makes the light focus at a predefined target. Copyright © 2007 by Optical Society of America.

existence of highly-transmitting Eigen-channels through strongly scattering materials [24], the 2007 work of Vellekoop and Mosk showed that incident light may be guided into these modes by controlling the phase of the incident spatial modes of light [13].

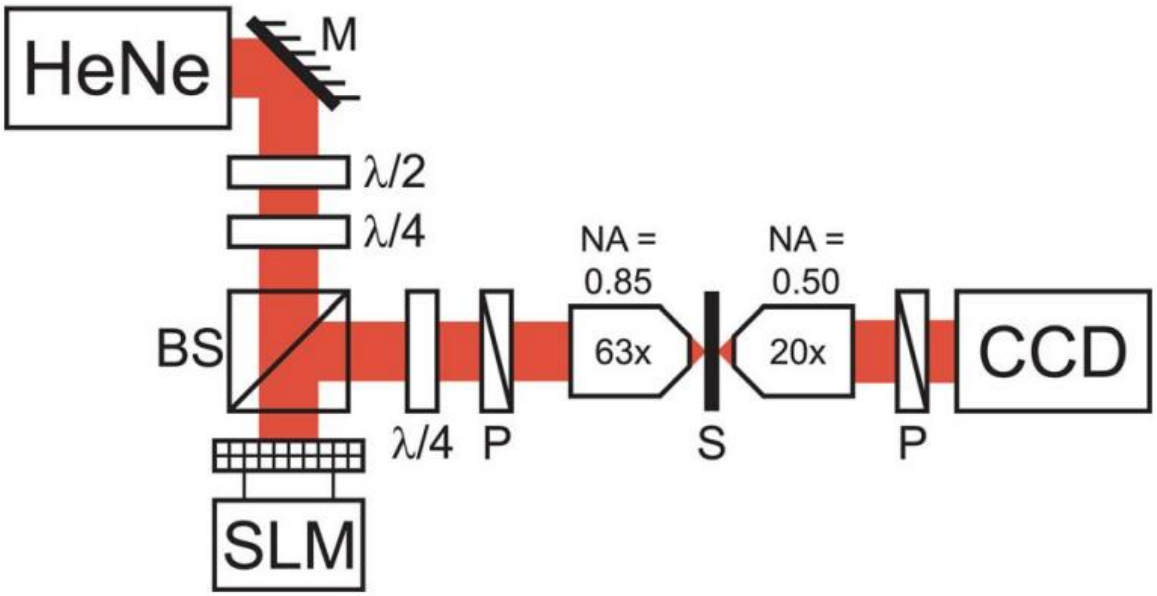

Figure 3. (Vellekoop and Mosk, 2007) Schematic of the apparatus. A 632.8 nm HeNe laser beam is expanded and reflected off a Holoeye LR-2500 liquid crystal spatial light modulator (SLM). Polarization optics select a phase mostly modulation mode. The SLM is imaged onto the entrance pupil of the objective with a 1:3 demagnifying lens system (not shown). The objective is overfilled; we use only segments that fall inside the pupil. The shaped wavefront is focused on the strongly scattering sample (S), and a CCD camera images the transmitted intensity pattern. $\lambda/4$, quarterwave plate; $\lambda/2$, half-wave plate; M, mirror; BS, 50% nonpolarizing beam splitter; P, polarizer. Copyright © 2007 by Optical Society of America.

Though scattering events may appear to be random and chaotic within a material such as body tissue, they are actually deterministic as long as the time period between observations is sufficiently short and the parameters of the spatial modes of incident light (phase and amplitude) are not altered. This time period is referred to as "persistence time" and is different for every material; it is representative of the speed at which the scattering centers move within the sample [13], [14], [25]. This time period is particularly short for fluids, in which scattering centers are constantly in motion, and can be quite long (on the order of hours or more) for more solid objects (a rock, for example).

For a single photon scattering event, the probability of scattering in any one direction is described by a probability distribution, and the photon cannot be expected to scatter in the same direction each time such an event is observed. Given a large number of incident photons, however, the incident power is divided into a relatively steady time-average at each scattering angle which is directly proportional to the value of the probability distribution at that angle. This

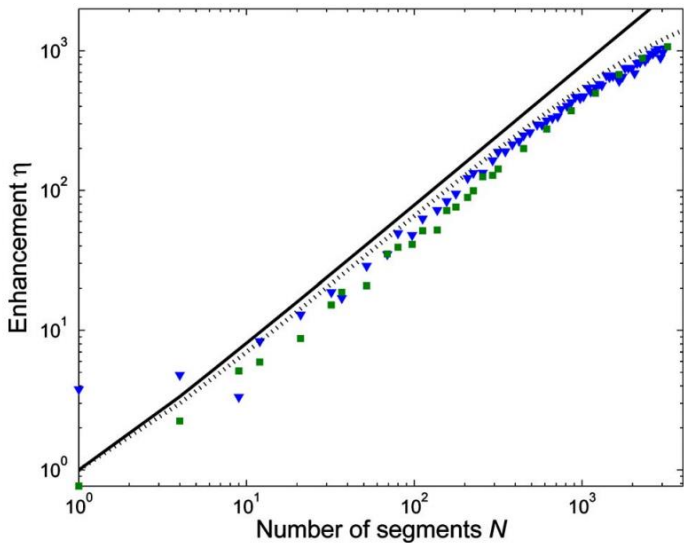

Figure 4. (Vellekoop and Mosk, 2007) Measured intensity enhancement as a function of the number of segments. Squares, sample in focus; triangles, sample 100 m behind focus; solid curve, ideal enhancement [Eq. (2)], dotted curve, corrected for residual amplitude modulation and finite persistence time of Tp=5400 s. The experimental uncertainty is of the order of the symbol size. Copyright © 2007 by Optical Society of America.

makes manipulation of the scattering possible, even to the point that it can be used to focus the light.

In the earliest version of this experiment, the light source was a helium-neon laser (632 nm) which was expanded to cover the face of the reflective SLM (setup shown in figure 3) [13]. The reflected light was imaged onto the surface of the sample using a microscope objective. A second microscope objective imaged the intended focusing plane onto a CCD sensor. The intensity at the intended focus was monitored via the CCD camera's recorded information.

The SLM face was divided into segments which were independently controlled to impart a phase delay on the incident wavefront. The SLM pixel size was ~8 microns, but these pixels could be binned together to produce a larger "superpixel". This point is critical, since the SLM had approximately 2 million pixels, and optimizing the phase for each of the pixels would be a very lengthy process. In binning together multiple pixels, the number of operations required to optimize the intensity at the focus was greatly reduced. However, as the number of binned pixels increased, the fine control of the wavefront would erode and the quality of the focus would diminish. Figure 4 shows the effect of the increasing number of segments on the ideal and experimental optimization [13]. The "knee in the curve" was found to be about 1000 segments. It

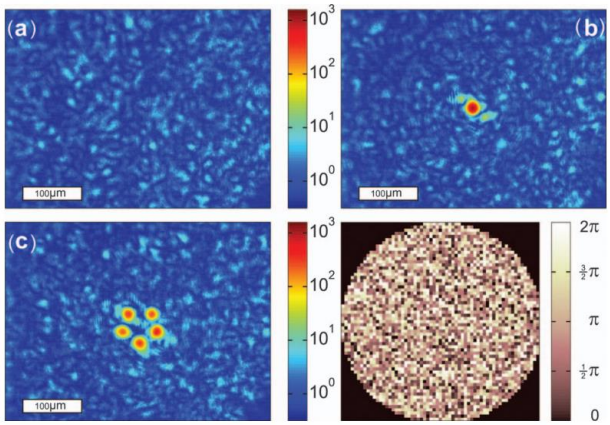

Figure 5. (Vellekoop and Mosk, 2007) Transmission through a strongly scattering sample consisting of TiO2 pigment. (a) Transmission micrograph with an unshaped incident beam. (b) Transmission after optimization for focusing at a single target. The scattered light is focused to a spot that is 1000 times brighter than the original speckle pattern. (c) Multibeam optimization. The disordered medium generates five sharp foci at the de- fined positions. (a)–(c) are presented on the same logarithmic color scale that is normalized to the average transmission before optimization. (d) Phase of the incident wavefront used to form (c). Reprinted with permission. Vellekoop IM, Mosk AP. Focusing coherent light through opaque strongly scattering media. Opt Lett. 2007 Aug 15;32(16):2309–11. Copyright 2007 by Optical Society of America.

is worth noting that when the wavefront is imaged onto the sample with a microscope objective, the magnification of the objective greatly shrinks the size of the segments; it is not advantageous to have control over segments that are much smaller than the spatial frequency of the scattering centers distributed within the material. There was a balance to strike between the amount of time taken to converge upon a solution and the quality of that solution.

The first experiments moved individually from segment to segment of the SLM and optimized the phase of that section of the wavefront with regard to the intensity measured at the focus. Later experiments moved on to finding the best algorithm for optimizing these segments in the most timely manner [14], [25].

The initial results of this experiment were reported using several different types of sample materials, though the bulk of the data reported was recorded while using a 10 micrometer thick sample of TiO_2 (rutile) deposited on a microscope slide [13].

Improvements in power delivered to the intended focus were reported to be as large as 1000 times greater than initial measurements (see figure 5) [13]. It is interesting to note that more than one focus can be produced; figure 5 shows several foci being produced at once [13]. Focusing

light to one or more locations is only a matter of selecting the desired location of the intensity measurements that are used as feedback for the optimization. If it is desirable to produce multiple focal points, then feedback intensity information is gathered from those points and the optimization process will bear out improvements in power delivered to those locations.

Although focusing within and behind a sample were successfully demonstrated, this method requires feedback from behind or within the sample material and a large number of optimization operations. These are disadvantages for practical use in some situations. For example, if the desired result is focusing through turbid water for communication, it is impractical to get intensity feedback from the desired focus because the target is likely far away (and if this were practical, communicating over a distance would not be necessary in the first place). For dynamic systems, particularly those composed of fluids, persistence time may also be on the order of milliseconds. In order to focus through such materials, it is highly desirable to converge to a solution very rapidly (milliseconds) while getting all required feedback from the incident side of the sample. This motivates one of the experiments discussed in this dissertation, namely improving transmission of light strongly scattering media using only backscattered light as feedback and by optimizing all segments of the incident wavefront at once (to improve the speed of the solution).

2.2 Optical Phase Conjugation

Optical Phase Conjugation (OPC) is the time-reversal of an optical signal which results in the signal traveling back along its original trajectory. Despite the appearance that scattering occurs randomly within a strongly scattering material, the scattering events and the paths taken by light through the material are deterministic. This means that OPC may be used in the presence of a scattering material to return light along a multiple-scattering trajectory through the material, returning it to its source. In a sense, this can be thought of as counteracting the effects of a diffusive media on a propagating optical signal. When combined with other techniques (such as ultrasonic encoding of light), OPC can be used for focusing and imaging within the material [1], [16]. The earliest known use of OPC for this purpose was by Emmett Leith and Juris Upatnieks in 1965, when they demonstrated that holographic imaging could be accomplished through a diffuser [26] using OPC.

To illustrate the concept of OPC, consider the experimental setup from reference [26], shown in figure 6. A diffuser sits between an object and a recording plane. The diffuser adds a spatially dependent phase to the light passing through it, $e^{i\phi(x,y)}$where x and y are transverse coordinates. The hologram is recorded in off-axis geometry. The real image is reconstructed from this recording but has phase $e^{-i\phi(x,y)}$(see section 1.1 for a brief review of holography). If the diffuser is placed at the plane of this image, the phase that is imparted by the diffuser will cancel the

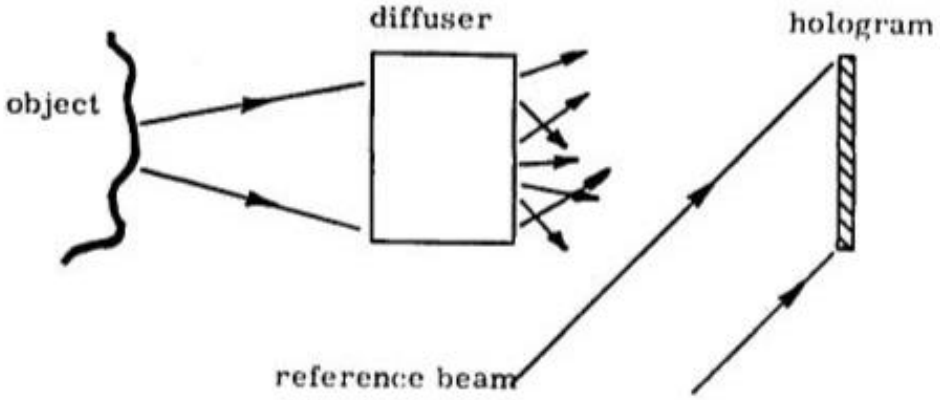

Figure 6. (Leith and Upatnieks, 1966) A diffuser is placed between the object and the recording plane. Copyright © 1966 by the Journal of the Optical Society of America.

phase differences in the real image, leaving only the image of the object behind the diffuser. This is highly dependent on the diffuser location and orientation, however, as it must precisely match in all six degrees of freedom (rotation and translation) its original location in order for this to be effective.

More recently, OPC has developed into a powerful tool that has been incorporated into many sophisticated imaging experiments, several of which will be briefly discussed here.

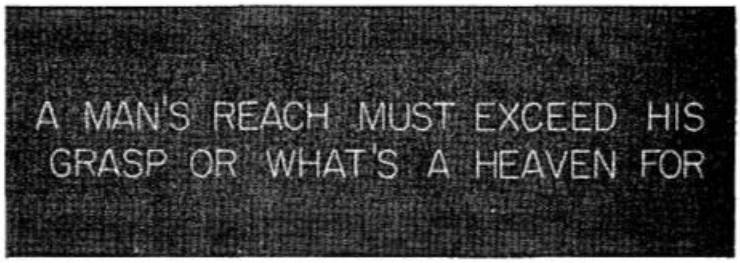

Figure 7. (Leith and Upatnieks, 1966) The object successfully imaged through a diffuser was a set of transmissive letters. Copyright © 1966 by the Journal of the Optical Society of America.

2.2.1 Focusing into scattering media using ultrasound-encoded light

As discussed previously, a central theme of this writing is the control of focusing within a media composed of densely packed, randomly distributed scattering centers. Traditional focusing techniques are only effective to a depth of around one mean free transport length [1], [16]. Until recently, experiments in which focusing was attempted at greater than this depth within tissue typically made use of only the ballistic component of light; scattered light was treated as noise and discarded. In the case of time-reversed ultrasonically encoded focusing (TRUE), the scattered light is critical to focusing. This experiment demonstrates the use of focused ultrasound and optical phase conjugation (OPC) on multiply scattered light in order to achieve a focusing solution deep within a sample, in particular a sample of body tissue. The focused ultrasound is used to create a ‘guide star’ for focusing the coherent light from the laser source. This type of focusing is of particular interest in biological tissues in which scattering of ultrasound is on the order of 1000 times weaker than the scattering of light in the optical wavelength range [16].

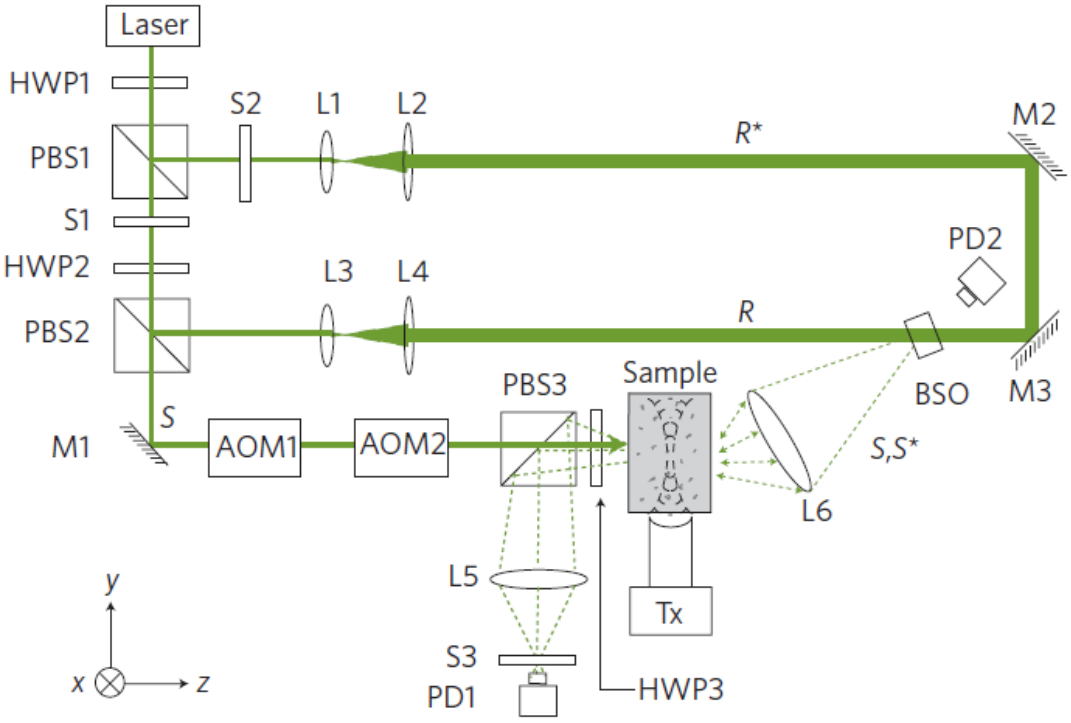

Figure 8. (Xu *et al.*, 2011) Schematic of the experimental setup for TRUE optical focusing. The time-reversal procedure consisted of recording and readout of a hologram. To record a hologram, shutter S1 was opened, and S2 and S3 were closed for 190 ms; to read the hologram, S1 was closed, and S2 and S3 were opened for 10 ms. HWPi, ith halfwave plate; PBSi, ith polarizing beamsplitter; Si, ith shutter; Mi, ith mirror; AOMi, ith acousto-optic modulator; Li, ith lens; PDi, ith photodiode; R, reference beam; R*, conjugated reference beam; S, signal light; S*, time-reversed signal light; BSO, Bi12SiO20; Tx, ultrasonic transducer with centre frequency fa = 3.5MHz, focal length = 38 mm, focal width = 0.87 mm. Coordinates: x-sample scanning axis, y-acoustical axis, and z-optical axis. Adapted by permission from Macmillan Publishers Ltd: Nature Photonics [16], copyright 2011.

Setup of this experiment is shown in figure 8 [16]. The source is split into three beams, two reference beams and a sample beam. The two reference beams, which are conjugated versions of each other, are used in the holographic recording and phase conjugation of the signal when it first exits the tissue. The sample beam is directed into the tissue. Making use of the acousto-optic effect, acoustic ultrasound waves are then focused to the desired focal point of the incident light. Incident light propagates diffusively in many directions within the tissue due to multiple scattering events. Despite these scattering events, some of the light makes its way to the ultrasound focal point. It is then frequency shifted by $\pm f_{acoustic}$ by the acousto-optic effect [16]. The focus of the ultrasound becomes a source of frequency-shifted light, creating the guide star that is necessary to facilitate focusing within the tissue. Some of this light then makes its way back (via multiple scattering) out of the tissue to a phase conjugate mirror.

In order to achieve time-reversal of this light, it is first necessary to make a holographic recording of its phase profile. One of the two reference beams is used to interfere with the light from the guide star point in the sample in order to make the recording. Then the hologram is read using the conjugate reference beam (recall from the holography review section that this results in a wavefront that forms a focus), focusing the light back at the guide star location after making its way through the multiple scattering events on the conjugate path that it took to exit the sample on its way to the recording plane [1], [16].

The amount of energy delivered to the focus is initially no more than the energy that made it there by propagating diffusively through the sample [16]. However, once focusing is achieved the gain of the delivered power can be increased by several methods, the most simple of which is to increase the intensity and shorten the duration of the conjugate reference beam used to read the hologram recording [1], [16].

The TRUE method of focusing has already been used to perform very sophisticated fluorescence imaging of tumors and other objects at depths of 2.5 mm, a significant improvement over previously demonstrated imaging up to 1 mm in depth [1].

2.2.2 Digital Optical Phase Conjugation

Development of biomedical imaging techniques is a common motivation for experiments dealing with the propagation of light through a turbid medium. Scattering is the dominant interaction in biological tissues when compared with absorption. Scattering events limit the distance of travel of ballistic photons, so that focusing and imaging are disrupted. However, elastic scattering is known to be a deterministic process so that after transmission through tissue, time-reversed signals are able to retrace their path through the tissue while experiencing scattering at the same locations. In a 2008 experiment, it was demonstrated that digital optical phase conjugation (DOPC) can be successfully used to counteract the effects of diffusive propagation through thin strips of cooked chicken breast [27].

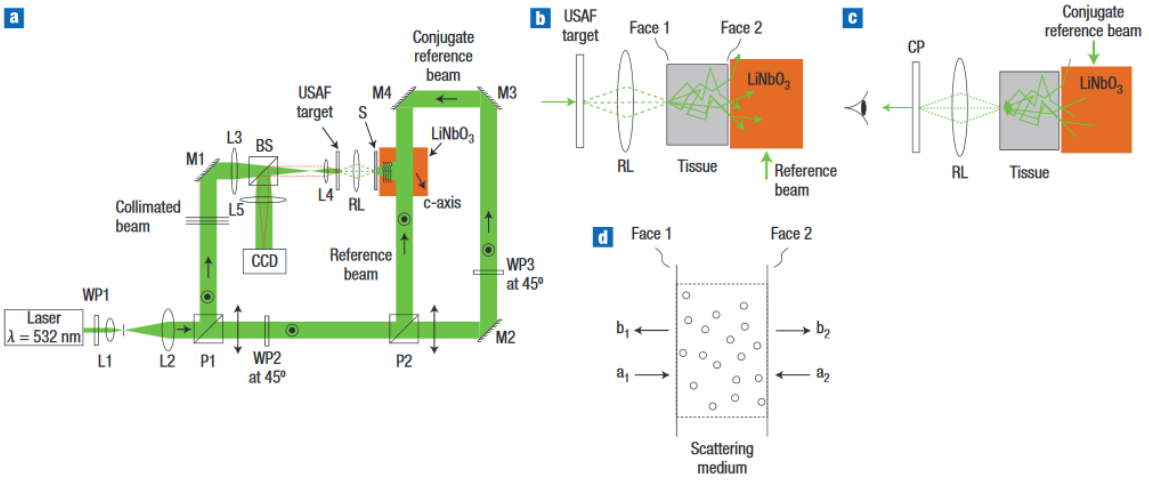

Figure 9. (Yaqoob et al, 2008) Schematic for TSOPC setup and scattering medium. (a) Experimental setup to confirm TSOPC in biological tissues. (b) (c) Schematic for the holographic recording (using the reference beam) and reproduction (using conjugate reference beam). (d) Scattering sample with incident and scattered light. Reprinted with permission. Cui M, Yang C. Implementation of a digital optical phase conjugation system and its application to study the robustness of turbidity suppression by phase conjugation. Adapted with permission from Nature Photonics [27], Copyright © 2008.

The setup for this experiment is shown in figure 9 [27]. The source is split using a polarizing beamsplitter to create a signal beam and a reference beam. The reference beam was also used to produce a conjugate reference beam. The signal beam was used to image a transparent Air Force Resolution Target in three configurations. For comparison, the first images were taken with a 0.46 mm thick sample of Agarose (transparent gel) in the position of the sample. Then a 0.46 mm thick sample of chicken breast tissue was placed in the sample position, and the target was imaged again. The resulting image was severely degraded. Finally, the target was imaged again using DOPC to time-reverse the signal beam through the chicken tissue sample before being recorded [27]. These results are displayed in figure 10 [27]. From these images, it is clear that DOPC was able to nearly completely reverse the effects of the diffusive propagation through the tissue [27]. Phase conjugate imagery has limited resolution. There is of course a diffractive limit and other limitations arise from inelastic or particle scattering processes and absorption by the sample.

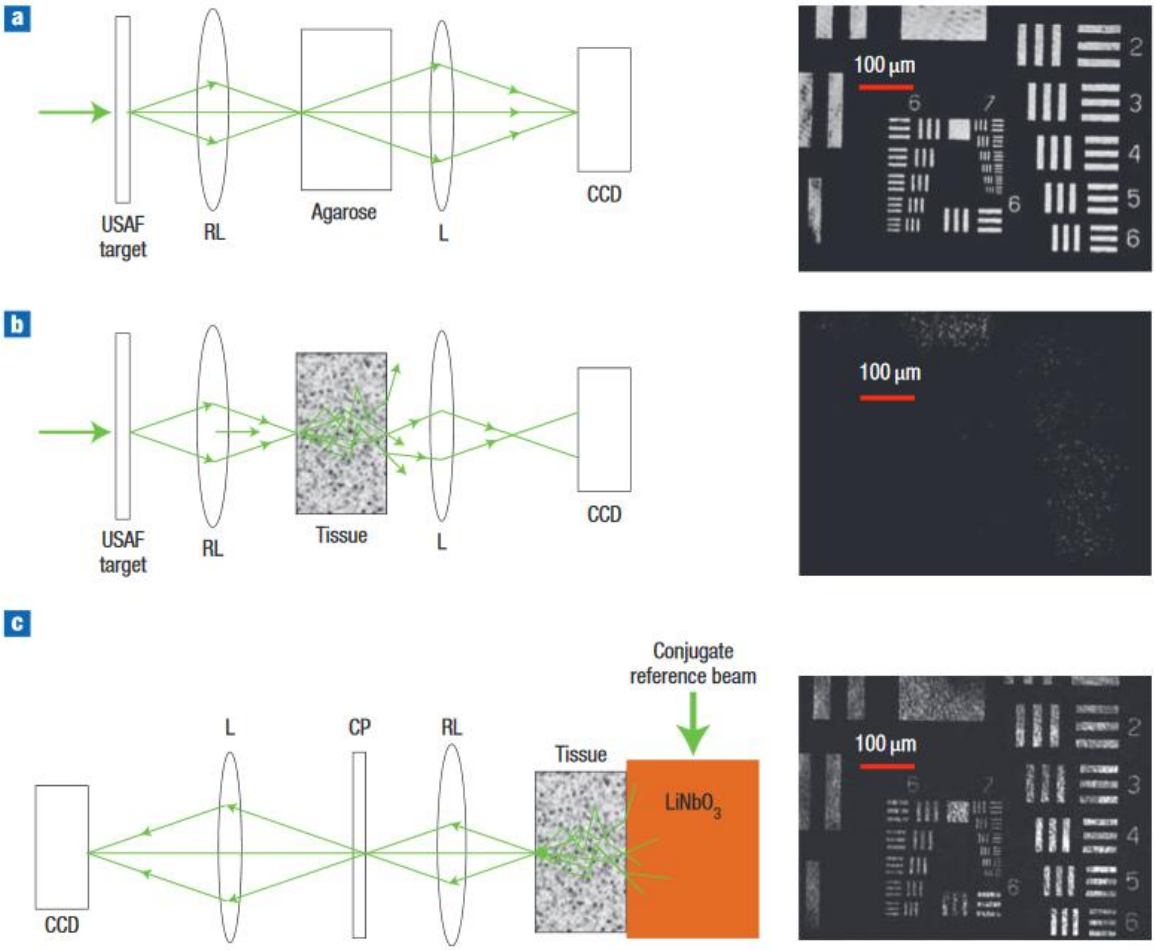

Figure 10. (Yaqoob et al, 2008) An Air Force Resolution Target was imaged using this optical system three times. In (a), the sample was a 0.46 mm thick piece of Agarose. In (b), the sample was a 0.46 mm thick sample of chicken breast tissue. In (c), the CCD camera was instead positioned to capture the image after passage through the chicken breast tissue sample twice; the second passage occurred after DOPC of the signal. The quality of the final image has been greatly enhanced in comparison with the middle image. Adapted with permission from Nature Photonics [27], Copyright © 2008.

Holographic recording and wavefront reproduction is a critical component of this technique. The signal wavefront exiting from the chicken tissue sample must be recorded and reproduced, which is accomplished using holographic methods discussed in 1.2. The reference beam is necessary to produce the interference pattern used to record the phase of the wavefront in the phase conjugate mirror ($LiNbO_3$ crystal doped with Fe), and the conjugate reference beam which enters the PCM from the opposite direction is used in reading the recorded hologram (this is another example of off-axis holography) [27]. It is worth noting that any displacement of the tissue sample between

recording and reconstruction will degrade the image. The sample must be static in all six degrees of freedom (rotation and translation) to make use of OPC, although *very small* movements of the sample will result only in degradation of the image; as the displacement of the sample from its location during recording increase, the image will continue to rapidly degrade until is completely destroyed.

In a second experiment by the same authors, a modified version of the experiment setup shown above imaged a point source of light [27]. In comparison to the Agarose control image, the image returned through a sample of chicken tissue 0.69 mm thick still had a peak intensity 17% of the incident light intensity peak, more than three orders of magnitude above background [27]. When the total collected light was measured instead of the peak intensity, it was found that 3.8 times as much light energy was collected using the a microscope objective at the front face of the sample as was collected without using DOPC [27]. These results suggest that DOPC may be useful in the medical field for a wide range of applications involving light delivery beneath the surface of the tissue.

2.3 Guide Stars and Beacons in Astronomy and Biology

Guide stars are another powerful tool for determining the detrimental effects of a sample on focusing and imaging, and compensating for it in order to facilitate focusing and imaging. A guide star is a signal within the sample (the sample may be the earth's atmosphere or biological tissue, as in the two examples discussed in this chapter, 2.3) that is measured by the observer for the purpose of creating a feedback control loop that compensates for detrimental effects of the sample on focusing and imaging. The control portion of the loop uses some form of adaptive optics (such as a deformable mirror) to impart corrections to the wavefront. The guide star acts like a "Trojan Horse" within the material to provide the information necessary to the observer for focusing light and imaging at or near the guide star location.

One of the major advantages of using a guide star is speed. Guide stars provide a continuous source of information about the changing sample so that the imaging system can keep up with the changing detrimental effects on imaging. There are limitations on the speed of converging to a solution (limited by the number of operations required to measure the distortion caused by the sample, the speed of the processing system, and the speed of the adaptive optics used), but in comparison with methods of sequentially performing wavefront phase optimization for focusing the use of guide stars and adaptive optics is orders of magnitude faster and can be effective when the sample is dynamic, with changes occurring over short periods of time. In air, these changes can be caused by changing weather patterns [4]. In biological tissue, changes can be caused by breathing, circulation and movement of the subject itself [9].

Naturally occurring guide stars have the disadvantage of being immobile. Any imaging that is to be done using corrections based on a specific guide star must be done in a very small area near the guide star. If a guide star does not exist in the area of interest, a different method of imaging must be used (if a virtual guide star cannot be created). In the case of astronomy, natural guide stars can be actual stars or other celestial bodies that reflect large amounts of light [4]. Within biological tissues, guide stars can be proteins which fluoresce at a given wavelength [8]–[10]. Guide stars may also be created by the observer, as in the case of laser guide stars (LGS) in astronomy. In biological tissues, guide stars can be introduced into the tissue which have a

preference for the type of tissue being imaged (such as cancerous tumors) [2] or they may be produced using ultrasonic devices [16]. Unfortunately, only the ultrasonic guide stars are mobile in tissue.

2.3.1 Guide Stars for Astronomy

Images of celestial objects taken by observatories on the ground are subject to distortions caused by traveling through the earth's atmosphere due to refraction as well as diffraction of light through the observing aperture of the telescope. If an optical system is free of aberrations due to imperfect lenses and other components, it is said to be diffraction-limited. However, the limitations on imaging through the atmosphere tend to be much more severe than the limitations of diffraction, as shown in figure 11 [4]. Optical systems whose most limiting source of error is the distortion caused by the atmosphere are said to be "seeing"-limited [4]. These limits can be quantified in terms of angular resolution.

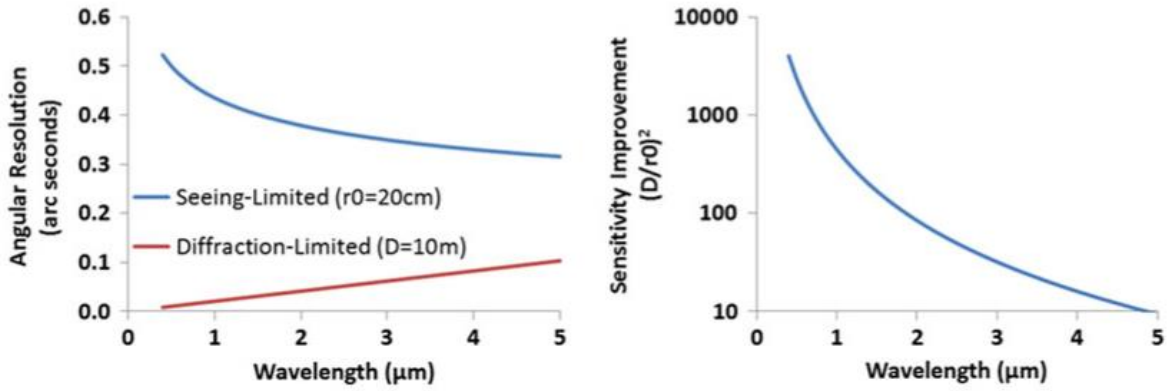

Figure 11. (Wizinowich, 2015) Left: Angular resolution of an optical system. D – diameter of the telescope aperture, r0 – turbulence correlation length in the atmosphere. Right: The sensitivity improvement in an optical system by going from seeing-limited to diffraction-limited. Adapted with permission from Taylor and Francis [4], Copyright © 2015.

Seeing is effected by small differences in the index of refraction throughout the atmosphere. As the images of celestial objects travel through space, the image wavefronts are flat and undisturbed. As they enter the atmosphere, however, they are subjected to the index of refraction of air which varies with location within the atmosphere [4]. These changes in the index of refraction cause sections of the wavefront to travel a slightly different optical path length between the edge of the atmosphere and the observer's telescope, giving portions of the wavefront a phase delay or advance relative to the rest of the image.

Adaptive optics systems are used to correct for these distortions and restore the quality of the images. Figure 12 shows the general setup of adaptive optics for distortion correction [4]. The signal is reflected from a deformable mirror (or other corrective optics) and then a portion of the signal is split off using a beamsplitter to a wavefront sensor. The wavefront sensor and the corrective optics form a feedback loop; if the wavefront sensed is not flat, a signal is sent to the corrective optics to alter its shape. Figure 13 depicts improvement in the quality of an image of the planet Neptune using this process [4].

A 'guide star' is necessary for this process. The guide star must be aligned with the telescope and

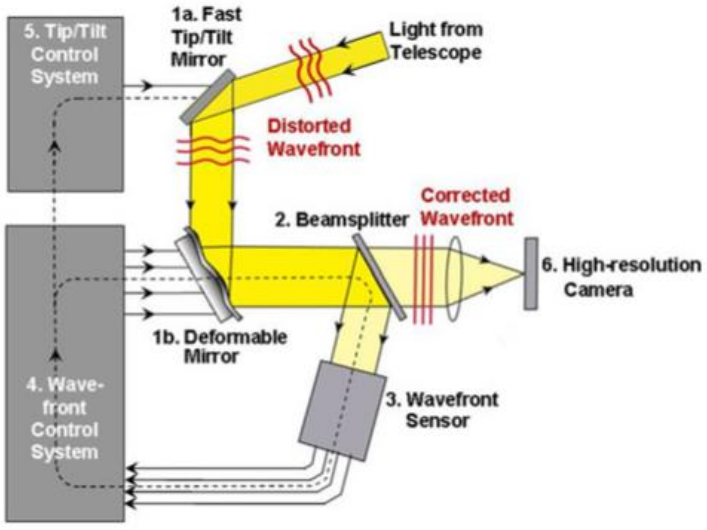

Figure 12. (Wizinowich, 2015) Schematic showing the concept of an AO system. A deformable mirror provides wavefront correction. Image credited to C. Max, Centre for Adaptive Optics. Adapted with permission from Taylor and Francis [4], Copyright © 2015.

the celestial object so that the path from both the guide star and the object is the same through the atmosphere to the telescope. Guide stars provide a reference by which atmospheric distortions can be observed and can either be natural (NGS) or created within the atmosphere using a laser (LGS). Natural guide stars are typically stars, but may also be planets or other objects within the solar system as long as they provide a compact image (small angle). The disadvantage of using NGS is that they must be bright enough for this purpose, and only about 1% of the sky has coverage by a bright enough NGS. LGS are created in the atmosphere using a laser and have the advantage of being placed at any location in the sky. They may be one of two types, either sodium or Rayleigh. Sodium LGS use a laser of the correct wavelength to excite sodium atoms suspended high in the atmosphere (up to about 90 km) (figure 14) [4]. Rayleigh LGS use Rayleigh scattering in the atmosphere between 10 and 35 km. Rayleigh LGS require range gating in order to produce a compact image but can be significantly cheaper than sodium LGS.

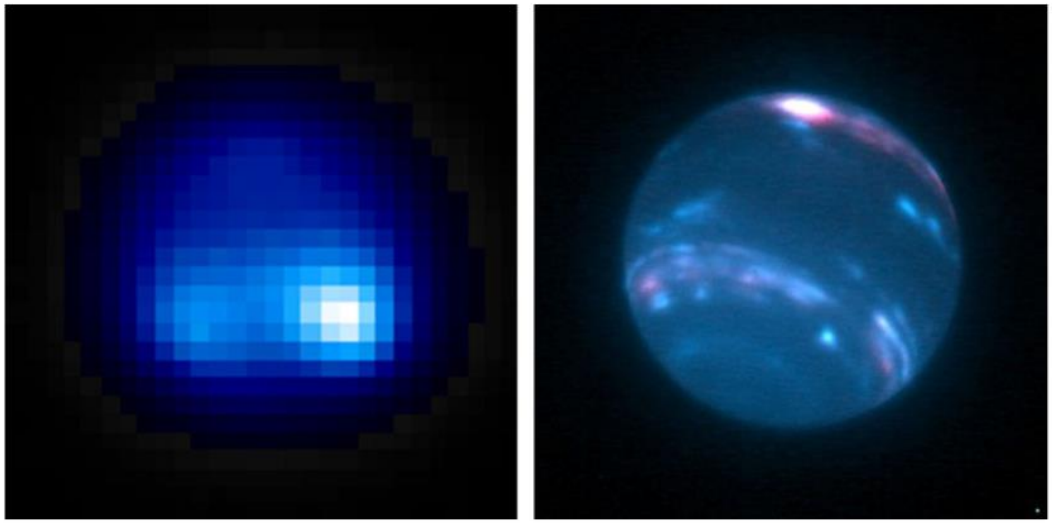

Figure 13. (Wizinowich, 2015) Images of the planet Neptune taken from the Keck Observatory 10m telescope. The left image is taken without the application of the adaptive optics to correct atmospheric distortions. The right image is a false color image taken with the aid of adaptive optics. Images credited to M. van Dam, E. Schaller, and WM Keck Observatory. Adapted with permission from Taylor and Francis [4], Copyright © 2015.

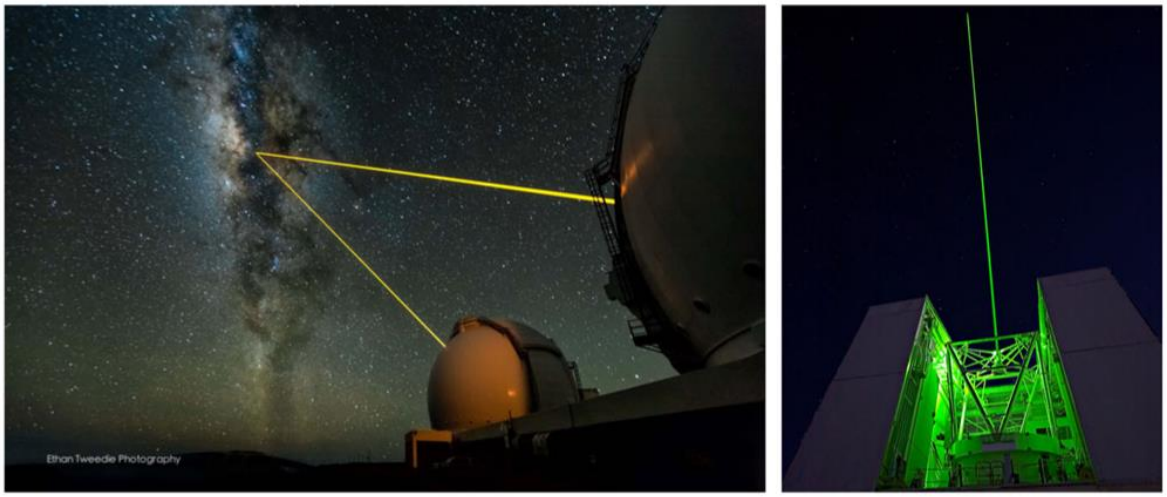

Figure 14. (Wizinowich, 2015) Sodium-wavelength lasers projected from the two W.M. Keck Observatory telescopes being used to observe the centre of our galaxy (left; courtesy Ethan Tweedie Photography). A green-wavelength Rayleigh laser projected from the MMT (right; courtesy T. Stalcup). In both images, only the Rayleigh scattered light is seen. The Rayleigh scattering ends as the atmosphere thins around 30 km from the ground. The sodium LGS is produced in the 10–20 km thick sodium layer at 90 km altitude. Adapted with permission from Taylor and Francis [4], Copyright © 2015.

Adaptive optics have greatly improved astronomical imaging from the earth's surface, allowing images to taken in the diffraction limit rather than the seeing limit caused by atmospheric turbulence. The combination of AO and LGS allows diffraction-limited imaging of celestial objects in any part of the sky.

2.3.2 Guide Stars for Biomedical Imaging

In-vivo imaging of biological tissue is also particularly problematic beyond a mean free transport length in depth because of the dynamic nature of living tissue. This includes imaging neurons in the brains of mice, which has recently been demonstrated by Kong and Cui (2016) using fluorophores in the brain tissue as a guide star [9]. They combined iterative wavefront phase optimization with fast deformable mirrors to measure and correct the refractive effects of the tissue on the light as it propagated to the desired focal point, in a method known as Iterative Multi-Photon Adaptive Compensation Technique (IMPACT) [8], [9]. By measuring the non-linear signal as they performed parallel wavefront segment optimization, they were able to achieve diffraction-limited focusing using IMPACT microscopy, which facilitated imaging

mouse neurons through a skull at a high resolution. Furthermore, the non-invasive nature of the technique allowed them to make observations of the same mouse over extended periods of time.

The schematic for the experiment setup is shown in figure 15 [9]. A NIR source of light was reflected from a deformable mirror before being directed into the tissue. Fluorescence in the guide star protein doubled the frequency of the light, shifting it into the visible range. Backscattered light was collected by the microscope objective and directed to a photo-multiplier tube (PMT) by use of a long-pass dichroic beam splitter. The total power of the fluorescence signal was maximized using a parallel wavefront optimization technique in which half of the

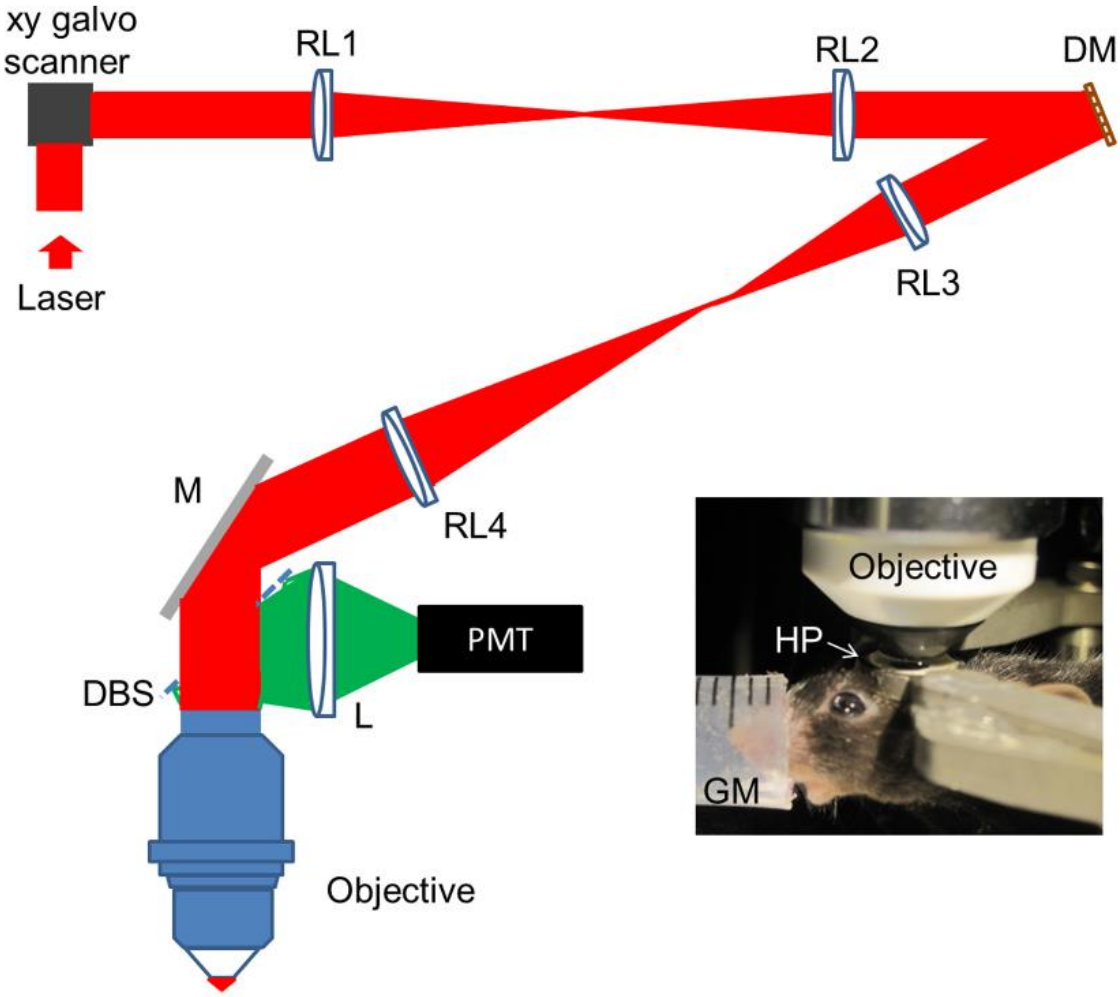

Figure 15. (Kong and Cui, 2016) Schematic of IMPACT microscopy. The NIR source was frequency-doubled by fluorescent proteins. Through use of a dichroic beam splitter (DBS), the strength of the fluorescence was measured by the photo-multiplier tube (PMT) during wavefront optimization. By integrating the IMPACT method with a microscope, neurons at a depth of approximately 149 micron depth beneath the skull were imaged. Copyright 2016 by IEEE.

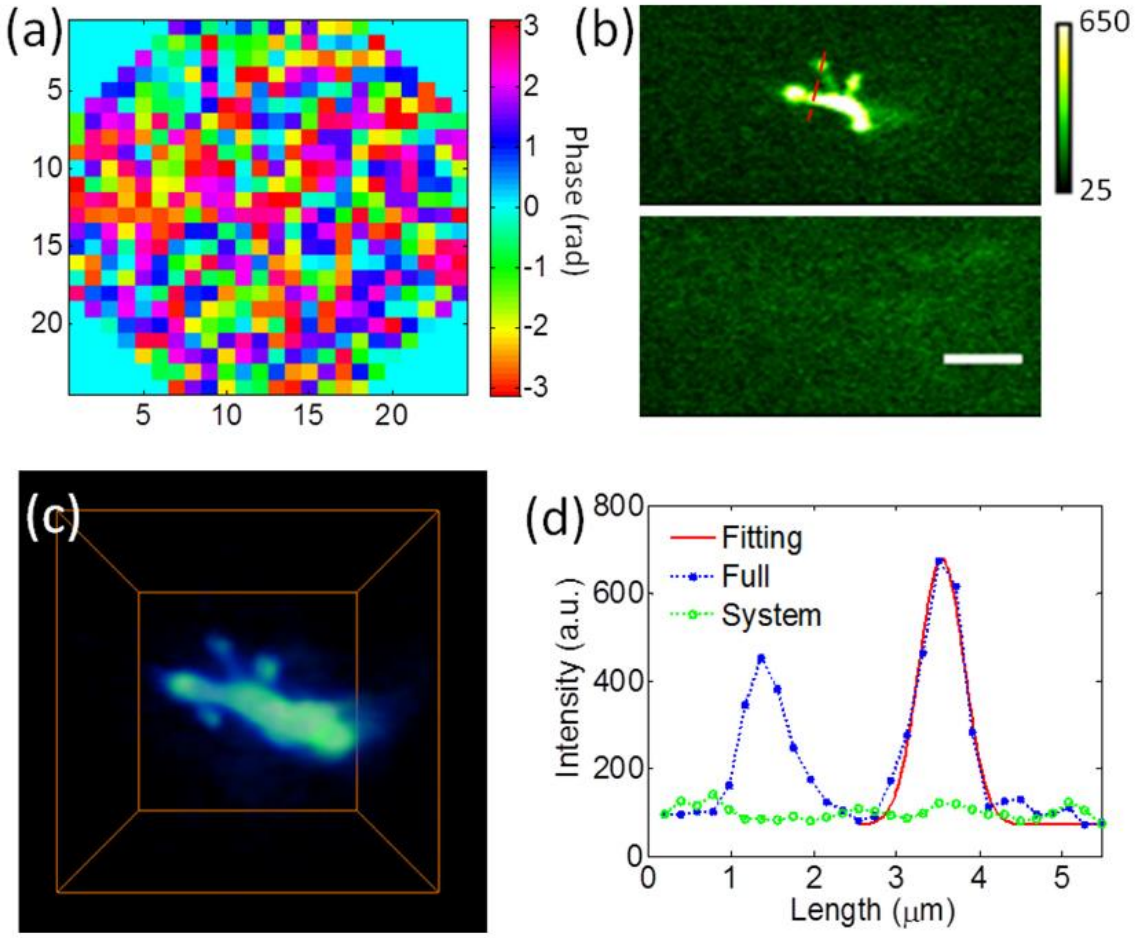

Figure 16. (Kong and Cui, 2016) Images of a dendrite (and spines) in a mouse brain through an intact skull. Thickness of the skull is about 100 microns. (a) Phase pattern for correction of both imaging system aberrations and tissue effects on propagation. (b) Image of a dendrite and spines at ~149.5 micron depth beneath the skull. (c) Volume image of the dendrite between 142-156 micron depth beneath the skull. Applied laser power was ~145 mw at 935 nm. (d) Intensity measured along the red dashed line in (b), showing the effects of wavefront correction. The green line is for correction of only the system aberrations, and the blue line is for correction of both the system aberrations and the scattering and refraction effects of the tissue. The red line is a Gaussian fit with a FWHM of about 0.64 micron. Copyright 2016 by IEEE.

segments of the deformable mirror were held constant to be used as a reference beam while the other half of the segments were phase modulated at unique frequencies. The collected fluorescence signal was Fourier transformed so that the effect of each individual segment on the signal could be uniquely identified, allowing the optimal phase of each segment to be identified. The compensating phase was then applied to the incident beam using the deformable mirror. The technique converged rapidly to a solution, in about three iterations of this technique.

Neurons within a mouse's brain were imaged using this method. The results are shown in figure 16 [9]. A dendrite and its spines were imaged through an intact mouse skull about 100 microns thick using a 935 nm source, both as a cross-section (149.5 microns beneath the skull) and in volume (142-156 microns beneath the skull) [9]. Part of the cross-section image of the dendrite was fitted with a Gaussian curve with a FWHM of about 0.64 microns in order to demonstrate the resolving power of the imaging technique [9].

IMPACT microscopic imaging and astronomical guide star imaging show that the use of guide stars can be another effective way of compensating for the effects of a scattering or refractive medium on the propagation of light used for focusing and imaging [4], [8]–[10]. Guide stars combine with adaptive optics such as deformable mirrors to create relatively high-speed imaging systems which can compensate for changing conditions as they occur. As depth of intended focus within a material increases, the severity of the image distortion effects also increases [8]–[10]. Guide star methods, which originated for the purposes of astronomy, have been effective in increasing the depth of imaging in biological tissues because of their effectiveness in quickly compensating for such severe distortions [8]–[10]. As mentioned previously, like other techniques guide star adaptive optics methods have both advantages and disadvantages. While they are useful in quickly converging to a solution, the solution is only good for focusing within a short distance of the guide star [4]. Naturally occurring guide stars are not controllable and are therefore immobile, meaning that unless an artificial guide star can be produced, these methods are not effective at an appreciable distance from the guide star location [4], [9]. Virtual guide stars can be produced for astronomical imaging using lasers [10], but within body tissue ultrasonic waves are much more effective for this purpose (due to the much smaller effect of scattering on these waves when compared with light) [16]. Guide stars in biological tissue are sometimes created by using nanoparticles or other small particles which are preferentially deposited in the tissue of interest (such as gold in cancerous tissues [2]), but these are also immobile once they have been deposited.

2.4 Summary of Recent Advances in Focusing and Imaging in Scattering Media

In summary of this brief review, there have been many recent advances in the development of techniques which effectively compensate for the detrimental effects of strongly scattering media on focusing and imaging. These include (but are not limited to) iterative wavefront phase optimization (2.1), optical phase conjugation (2.2), and guide star methods for focusing and imaging (2.3). These techniques span a very broad conceptual range, the breadth of which cannot be adequately represented in this brief review. However, the methods discussed here have interest to the author for their relevance to the research that will be presented in section 3. This review is intended not only to showcase some of the interesting methods that have been developed over the years, but also to highlight that each of these methods, while sophisticated and effective in their own ways, has a limitation of some kind. There is no "ultimate" imaging and focusing method that presently exists which is effective in every possible material, geometry, or scenario conceivable. There is still room in the field of focusing and imaging in the presence of scattering media for expanding the breadth of circumstances for which these methods can be effectively used. This is the motivation for the new experiments presented in section 3, each of which is an attempt to expand upon previously published methods of focusing and imaging in scattering media. A holographic imaging method is presented in 3.1 which uses a rotating diffuser to compensate for the effects of speckle created by reflecting a signal from a rough surface, building upon an experiment by in which the compensation for this speckle was performed by small movements of the reflecting surface. In 3.2 and 3.3, two new iterative wavefront phase optimization experiments are discussed. Focusing backscattered light to an arbitrary location with the speckle was performed by a wavefront optimization method first published by Vellekoop and Mosk in 2007 [13], but it was performed in a new experiment using backscattered light. Enhanced transmission of light through a strongly scattering sample by the analysis of backscattered light, combined with a form of phase-conjugate mirror and a new iterative algorithm (Jin *et al.*(2012)) was attempted. This method will require future work in order to successfully achieve enhanced transmission, but the experimental results laid the groundwork by demonstrating that suppression of backscattered light is possible using this method. If successful enhanced transmission is achieved, this will be another effective method for improving the depth of transmission through scattering media which is fast and non-invasive

and uses non-ionizing electromagnetic waves. Speed and non-invasiveness are still sought-after characteristics of new focusing and imaging methods, despite the number of methods that have already been developed. This concludes the introductory material of this dissertation.

Chapter 3: Original Experiments

In this section, three experiments are discussed in depth. The goal of each of these experiments is to understand and compensate for the effects of scattering media on focusing and imaging with light. The first of these experiments is a lensless Fourier transform holographic imaging method which makes use of statistical averaging to compensate for the random phase imparted on the signal during reflection from a rough surface. The second and third experiments are both iterative, phase-optimization methods of compensating for the effects of scattering by strongly scattering media. Though the experiments are all related by the presence of scattering media, the phase-optimization experiments share a common setup and mode of control of light (a reflective, phase-only SLM).

Each of the three experiments presented here in 3.1-3.3 has a separate introduction, theory, methods, results and discussion. They can be read as stand-alone pieces of writing without loss of understanding, or in order. Some of the components of the transmission enhancement experiment in 3.2 are particularly technical, and although they are critical for understanding how to undertake such an experiment, they have been moved into the appendices to prevent their rigor from getting in the way of a broader understanding of the experiment approach and results.

3.1 Holographic imaging through a scattering medium by diffuser-assisted statistical averaging

3.1.1 Introduction

Inhomogeneous media composed of randomly distributed scattering centers present a challenge for imaging techniques. Traditional imaging can be very difficult or even impossible within or through such a medium, with scattering causing haziness at best and at worst complete loss of the image. The desire to image through turbid or opaque materials has applications in multiple real-world scenarios that span areas from biomedical imaging to covert military communications to astronomy. Due to the broad range of potentially impactful (and lucrative) applications, this area has been a hotbed of research that has produced countless scientific papers and techniques even in the last ten years.

A number of techniques have been developed with the goal of focusing or imaging through an opaque, strongly-scattering sample: holographic wavefront reconstruction techniques [28], [29]; pulsed lasers and high-speed shutters for ultrafast gating purposes to extract the first-arriving light [30]; enhanced gating based on beams with reduced spatial or temporal coherence [29], [31]–[33]; ultrafast parallel wave-front optimization and adaptive compensation [8], [34]; guide star methodology [4], [35]; ultrasonically encoded time-reversed light [1], [16, p.], [36]; two photon nonlinear microscopy [37] and wave-front optimization [14]. These earlier methods either make use of specialized ultrafast lasers or tend to be computationally intensive. Recently, many non-invasive imaging approaches have been developed which make use of the speckle phenomena arising from the scattering layer itself [38]–[41]. In particular, there have been approaches based on speckle correlation which utilize the principle of memory effects in scattering from a thin layer of diffusing media [39], [40] or use spatial input–output correlation to identify specific back-scattered waves from objects hidden deep inside scattering media [41]. Another approach makes use of two point intensity correlation (i.e. fourth order speckle statistics) to retrieve the complex wave-field information beyond a scattering media [42]. These

correlation-based methods have been promising on many fronts as they involve one-step processes which minimize the computation required to realize the final image.

One technique for imaging in reflection from a rough surface is particularly simple yet effective. This technique takes advantage of the ergodicity of a rough reflective surface to overcome the limitations of recovering an image that is reflected from it. One of the advantages of this method is that there does not need to be a direct path between the object and the sensor; as the title of the Singh paper puts it, this allows one to "see around corners" in a sense, potentially taking advantage of reflection surfaces that are already in place within a system. The geometry of this technique is that of a coherent light image in reflection from a rough surface and imaged onto a sensor, interfering with light from a point source (which travels the same path after reflection) that allows the use of lensless Fourier transform holography to recover the image of the object. While the reflection surface is steady, the resulting image is degraded by the contrast of the speckle pattern falling on the sensor. The speckle, a randomly occurring set of constructive and destructive interference caused by differences in optical path length for the many modes of reflected light, has a high contrast meaning that some areas are very bright while others have almost no data at all. By moving the reflection surface itself during the data collection process the resulting data becomes a time-average of the rapidly, randomly changing speckle pattern. Due to the ergodicity of the surface, this reduces the time-averaged contrast of the speckle and improves the quality of the resulting image.

This statistical averaging technique is described in detail by Singh *et. al.* [18]. In their paper, both reflection and transmission geometries are discussed. It is the reflection geometry that is of particular interest here. In this geometry, Singh illuminates an object using coherent light. The light reflected from this object forms a wavefront that carries the information necessary to form an image of the object. The light scattered from the surface of this object is then reflected from a rough aluminum surface. This surface serves to randomize the phase of the incident light much the way that transmission through a diffuser would. It was shown that the statistical averaging method was effective in both the reflection and transmission geometries. In the reflection geometry, the aluminum surface was moved to provide the averaging effect.

The drawback of this method is that the reflection or transmission surface must be moved. If this surface is a part of the environment (such as a wall), movement of the surface may not be convenient or even possible. This issue motivates the method presented here. It is a holographic imaging method which requires the use of coherent light to illuminate the object to be imaged, and makes use of the reflection geometry discussed previously. Expanding upon the results of Singh et. al., this method adds a rotating diffuser that is physically separated from the reflection surface. Its rotation performs the same function as the movement of the reflection surface, in that it provides a means of reducing the speckle contrast when the light collected from the system is time-averaged. This provides the same type of improvement in image quality, but the separation of the moving part of the system from the reflection surface makes usage of this method possible in situations where movement of the reflection surface is not an option.

In this section, the method described is a lensless Fourier transform holographic imaging method with makes use of a single rotating diffuser to statistically average the speckle reflection from a spatial light modulator (SLM) to remove the drawbacks of the previous method without requiring pulsed lasers or time-gating. It will be shown that this method resulted in significant improvement of two separate images without the need for phase conjugation or any direct control of signal phase. The same experiment was then repeated with an additional static diffuser added. In this configuration, the object to be imaged is effectively between two diffusers and the results of the experiment are similar.

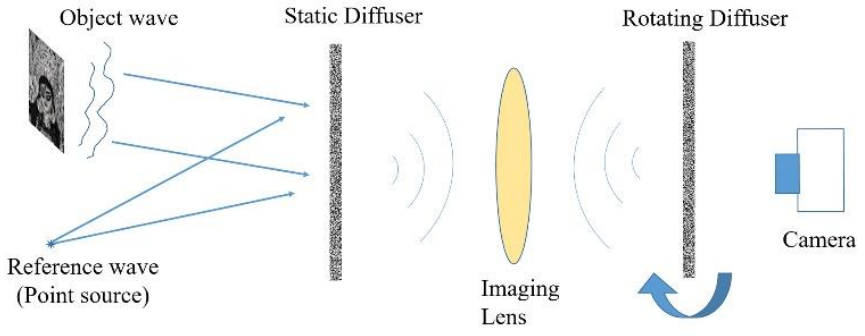

Figure 17. (Purcell *et al*., 2016) Schematic representation of the new imaging approach. Copyright © 2016 by Optical Society of America.

3.1.2 Analysis of Diffuser Assisted Holographic Imaging

A reference point source and an illuminated object form signals that combine in this lensless Fourier transform holographic imaging system (figure 19). The reference wavefront can be described in a similar manner to equation 9, where the phase is a function of the distance traveled along the optical axis and the transverse spatial variables, although for simplicity the optical axis variable z has been ignored here. The two wavefronts combine before reflection from the static diffuser (SLM) (equation 9). In these equations, ξ and η are coordinates in the plane transverse to the optical axis, immediately in front of the SLM screen. The total wavefront is the sum of the reference and object waves.

$$u(\xi,\eta) = u_{obj}(\xi,\eta) + u_{ref}(\xi,\eta) \tag{9}$$

The SLM adds a random phase which is dependent on the same transverse coordinates.

$$u_{slm}(\xi,\eta) = e^{-i\phi_{rand}(\xi,\eta)} \tag{10}$$

The field at this point is described by equation 11.

$$u_{diff} = u(\xi,\eta)u_{slm}(\xi,\eta) \tag{11}$$

It is worth noting that because the point source reference and the object wavefronts travel the same path through the optical system, there is no loss of relative phase information between the two.

This wavefront is imaged onto the surface of a second diffuser by a pair of lenses forming a 4-f system. Immediately after passing through the diffuser, the field becomes:

$$u_{diff} = \exp[-i\phi_r'(\xi,\eta)] \iint u(\hat{\xi},\hat{\eta}) \exp\left[-i\phi_r(\hat{\xi},\hat{\eta})\right] h_0(\xi-\hat{\xi},\eta-\hat{\eta})\, d\hat{\xi}d\hat{\eta} \tag{12}$$

In this equation, $\phi_r'(\xi,\eta)$ is a random phase imparted by the diffuser and $h_0(\xi-\hat{\xi},\eta-\hat{\eta})$ is a point spread function for the 4-f imaging system. When the super-pixels on the SLM are large enough, the point spread function is localized enough that $h_0(\xi-\hat{\xi},\eta-\hat{\eta})$ approaches a delta function, $\delta(\xi-\hat{\xi},\eta-\hat{\eta})$. In this case, equation 12 simplifies greatly to the following:

$$u_{diff} = u(\xi,\eta)\exp[-i\phi_{tot}(\xi,\eta)] \tag{13}$$

Making this approximation accurate has a significant effect on the quality of the resulting images, as will be shown.

This wavefront is then imaged onto a CCD sensor and recorded. The recorded data is intensity data which is a convolution of the wavefront and the point spread function of the imaging optics, g(x-ξ,y-η).

$$u_{ccd}(x,y) = \iint u_{diff}(\xi,\eta)\mathrm{g(x\text{-}\xi,y\text{-}\eta)}\,\mathrm{d}\xi\,\mathrm{d}\eta \tag{14}$$

The intensity measured at the CCD is then $|u_{ccd}|^2$:

$$\begin{aligned} I_{ccd} &= |u_{ccd}(x,y)|^2 \\ &= \iint\iint u(\xi_1,\eta_1)u^*(\xi_2,\eta_2)e^{-i\phi_{tot}(\xi_1,\eta_1)}\,e^{-i\phi_{tot}(\xi_2,\eta_2)}h(x \\ &\quad -\xi_1,y-\eta_1)h^*(x-\xi_2,y-\eta_2)\,d\xi_1 d\eta_1 d\xi_2 d\eta_2 \end{aligned} \tag{15}$$

There is a limitation on the information that can be collected with this system, however. Due to the limited numerical aperture of the collection optics, parts of the signal that are diffracted at a large enough angle relative to the optical axis may be lost.

In order to reduce the contrast of the speckle, time-averaged information is recorded at the CCD plane. Physically, this is accomplished by rapidly rotating the second diffuser while the extended exposure takes place. Over a long enough exposure time, the CCD output is given by the time average $\langle|u_{ccd}|^2\rangle$. With the assumption that the speckle pattern from the diffuser is ergodic in

nature and delta-correlated, time averaging is equivalent to ensemble averaging [43], which changes part of equation 15 to the following:

$$\langle e^{-i\phi_{tot}(\xi_1,\eta_1,t)} e^{i\phi_{tot}(\xi_2,\eta_2,t)} \rangle = \delta(\xi_1 - \xi_2, \eta_1 - \eta_2). \quad (16)$$

When this is substituted into equation 15, it becomes clear that the signal at the CCD plane is described by a convolution of the square of the transfer function of the optics and the square of the signal wavefront magnitude:

$$< I_{ccd} >=< |u_{ccd}(x,y)|^2 >= \iint |u(\xi,\eta)|^2 \times |h(x-\xi, y-\eta)|^2 \, d\xi d\eta. \quad (17)$$

The first term here is the intensity of the signal wavefront, and the second term is the square of the transfer function of the system. Using the convolution theorem, the signal recorded at the CCD can be described as the product of the Fourier transform of the signal wavefront intensity ($F\{|u(\xi,\eta)|^2\}$) and the Fourier transform of the transfer function ($F\{|h(x-\xi, y-\eta)|^2\}$).

3.1.3 Structural Similarity Index

The structural similarity index (SSIM) was used as the criteria for quantifying the quality of the image results in this experiment. Imaging systems are frequently designed to produce an image that can be understood by the human visual system (HVS). This motivates the need for a measure of how accurately a system can reproduce an image as perceived by HVS. Until 2004, the most common of these measurements was the mean squared error (MSE) measurement [44]. If it is assumed that an image is composed of a perfect reference image overlaid with an error signal, then the error can be quantified by summing the square of the differences in signal at each pixel of a digital image and averaging them [44]. However, many practitioners of digital image processing feel that MSE is inaccurate in predicting perceptual distortion of an image [44], [45]. Figure 18 shows several images with equivalent MSE, but with very different perceived image quality [44]. The SSIM was much better at predicting the perceived quality of these images [44].

For this reason, the structural similarity index (SSIM) was developed. SSIM takes two signals as its input, x and y, to be compared with each other and assumes that one of these is a perfect reference signal. It then makes three comparisons of the second signal against the first: luminance, contrast, and structure, each of which is independent of the other two (for example, changing luminance and contrast will not affect the structure comparison function) [44].

In order to calculate the SSIM for the pair of signals, the luminance of each signal, μ, is calculated as in equation 18, where x_i is the intensity at the i^{th} pixel.

$$\mu_x = \frac{1}{N}\sum_{i=1}^{N} x_i \tag{18}$$

The luminance comparison is a function of μ_x and μ_y:

$$l(x,y) = \frac{2\mu_x\mu_y + C_1}{\mu_x^2 + \mu_y^2 + C_1} \tag{19}$$

Next, the contrast of the two signals is calculated. The luminance of each signal is subtracted from the entire signal so that the average value is zero. The standard deviation of the new values is used as an estimate of each signal's contrast. An estimate of the standard deviation is calculated as in equation 20 [44].

$$\sigma_x = (\frac{1}{N-1}\sum_{i=1}^{N}(x_i - \mu_x)^2)^{1/2} \tag{20}$$

The contrast comparison function, C(x,y), is a function of σ_x and σ_y, equation 21 [44].

$$C(x,y) = \frac{2\sigma_x\sigma_y + C_2}{\sigma_x^2 + \sigma_y^2 + C_2} \tag{21}$$

For the structure comparison function, the luminance, μ, of each signal is subtracted from the signal. Then, each signal is divided by its estimated standard deviation so that the standard deviation of each becomes unity. The correlation between the vectors resulting from this process, $(\mathbf{x}-\mu_x)/\sigma_x$ and $(\mathbf{y}-\mu_y)/\sigma_y$ forms the structure comparison function [44], equation 22.

$$s(x,y) = \frac{\sigma_{xy} + C_3}{\sigma_x^2 + \sigma_y^2 + C_3} \tag{22}$$

An estimate of σ_{xy} is shown in equation 23 [44].

$$\sigma_{xy} = \frac{1}{N-1}\sum_{i=1}^{N}(x_i - \mu_x)(y_i - \mu_y) \tag{23}$$

Finally, the three comparison functions are combined in the SSIM in the following manner:

$$SSIM = [l(x,y)]^{\alpha}[c(x,y)]^{\beta}[s(x,y)]^{\gamma} \tag{24}$$

where the three exponents α, β, and γ can be adjusted to weight the relative importance of each comparison function if desired (but may be left equal to one) [44]. There are special forms of the SSIM for some values of the constants C_1, C_2, and C_3. This is beyond the scope of this thesis, although more information can be found in reference [44].

The term SSIM may refer to this process carried out for one small window of larger images.

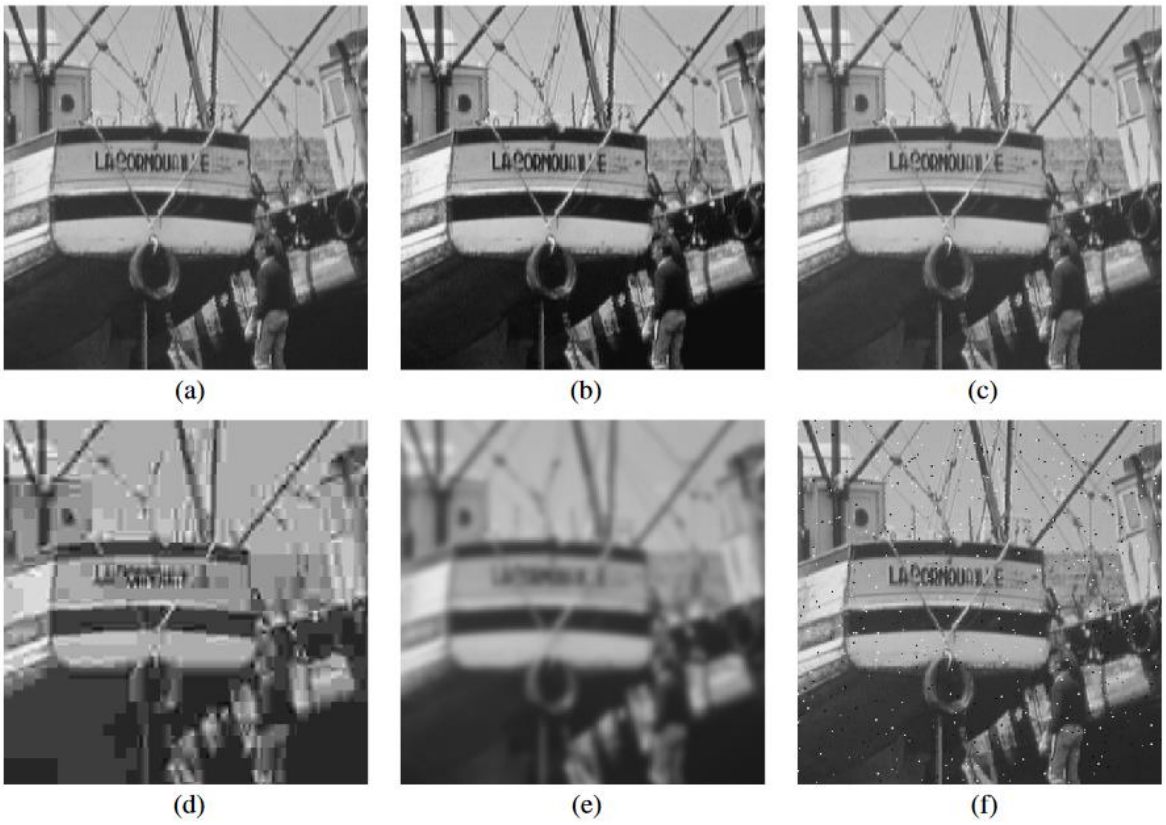

Figure 18. (Wang *et al.*, 2004) Each of the images (a) through (f) has been affected with a different type of error, but they have the same MSE value. The MSSIM value for each is very different, however. Copyright © 2004 by IEEE.

When applied to an entire image, the SSIM for each window of the image is averaged (as in equation 25) and the resulting value is called the mean structural similarity index (MSSIM) [44].

$$MSSIM = \frac{1}{M}\sum_{j=1}^{M} SSIM(\boldsymbol{x}_j, \boldsymbol{y}_j) \tag{25}$$

The MSSIM and SSIM both have the following three properties [44]:

1. They are symmetric (SSIM(**x**,**y**) = SSIM(**y**,**x**)).
2. They are bounded (SSIM(**x**,**y**) ≤ 1).
3. SSIM = 1 if and only if **x** = **y** (the signal images are identical).

The SSIM function in MATLAB [46] was used to evaluate the images. All exponents and constants were set to their default values; α, β, and γ have default values of one, and the three constants C_1, C_2, and C_3 were set to a default value based on the dynamic range of the image type, which is automatically detected by MATLAB [46].

3.1.3 Methods of Diffuser Assisted Holographic Imaging

If the hologram is recorded in the lens-less Fourier transform holographic arrangement, the object wave can be easily reconstructed by simply taking a Fourier transform of the hologram function where both real and virtual images are obtained on two sides of the central DC term [18]. We follow this same principle while recording the hologram in our experimental setup, shown schematically in figure 19. For the experiment, an image (of 'Durga') was printed on a transmissive plastic sheet (of dimension 1 inch by 1 inch) to serve as the object. A linearly-polarized, optically-pumped semiconductor laser (Coherent Sapphire) operating continuously at 488 nm served as the light source.

The beam was split into two parts with a 50-50 non-polarizing beam splitter. One part was magnified in a beam expander and passed through the object to provide the object wave. The

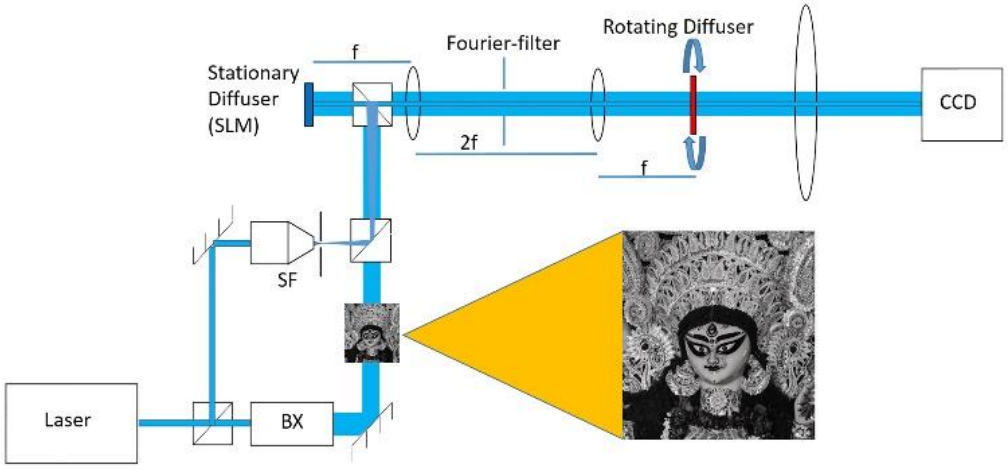

Figure 19. (Purcell *et al*., 2016) Schematic of the experimental setup for diffuser assisted lensless holographic imaging of the transmissive object, a picture of the Hindu Goddess Durga (photo courtesy of Manish Kumar Photography). SF: spatial filter, BX: Beam expander. Copyright 2016 by the Optical Society of America.

other part was directed through a spatial filter consisting of a 20x microscope objective and a 15 μm pinhole to provide a diverging wave-front as the reference wave. To implement the Fourier transform holographic recording approach, the pinhole (serving as the origin of the diverging reference wave) and the object were placed at equal distances from the reflective, phase-only SLM (Holoeye Pluto VIS). The reference and object waves were then combined with the help of a beam splitter to form a hologram on the SLM. The surface of the SLM was in turn imaged on an additional diffuser using a 4-*f* imaging system (f1 = 30 mm and f2 = 12 mm). Finally, the surface of the second diffuser was imaged on a CCD camera (Andor iXon 885 EMCCD) using another dual lens based 4-*f* imaging system. Figure 19 shows a schematic diagram of the entire experiment with the second 4-*f* system represented by a single lens. The SLM was used as a diffuser by applying random phases between 0 and 2π to its pixels. The Holoeye SLM has square pixels arranged in a rectangular matrix 1920 pixels wide and 1080 high over its active display area. Each pixel was 8 μm on a side. During the experiment, many adjacent pixels were grouped together to form square super-pixels. The size of super-pixels was varied from 1 pixel (8 μm) to 50 pixels (400 μm) per side. For each size, intensity data was captured on the camera and a 2-D Fourier transform was performed to reconstruct the image of the object. These measurements constituted a first set of results in which only one diffuser (the SLM) was inserted in the setup. To process background speckle, a 600-grit ground glass diffuser (Thorlabs DG20-600-MD) was placed at the image plane of the 4-*f* configuration. This additional diffuser was mounted on a platform normal to the optical axis of the system and rotated at around two hundred rotations per minute (200 RPM) while intensities were again recorded at the camera, providing a second set of results with longer exposure times (~0.9 seconds) corresponding to the time averaged intensity calculated in equation 17.

Since the active area of the SLM is structurally periodic, it produces multiple orders of diffraction. Hence reflected light splits into orders that travel at different angles with respect to the optical axis in the experiment. The higher orders correspond to higher spatial frequencies and make larger angles with respect to the optical axis. Since good imaging of light from the first diffuser plane onto the second diffuser is crucial for successful image retrieval by this method, it is important that multiple diffraction orders are collected by the 4-*f* imaging optics. To demonstrate this feature, we took advantage of pixel grouping to control the number of

diffraction orders accepted by the limited numerical aperture of our experiment. Smaller sized super-pixels corresponded to higher spatial frequencies, leading to larger propagation angles with respect to the optical axis. High quality reconstruction of images scattered by small scattering centers therefore calls for imaging lenses with large numerical aperture. The highest transverse spatial frequencies are generated from the smallest groupings of diffracting structures i.e. individual pixels of the SLM. Since these pixels were 8 μm on each side, the highest spatial frequency (for first order diffraction) produced by the SLM was determined by this length.

The first lens in the 4-*f* imaging system performs a Fourier transform of the intensity distribution coming from the SLM. The Fourier plane lies at the front focal plane of the lens, whereas the SLM is positioned at the back focal plane. Since SLM represents a sampled signal, it generates multiple copies of the band-limited signal in the Fourier plane and we need to select only the fundamental order of the band limited signal. For this purpose, a spatial filter was placed at this Fourier plane to exclude all copies of the sampled phase function displayed on SLM. Thus all the spatial frequencies higher than 0.5 times ±1 diffraction order for 8 μm periodicity had to be blocked. The filter was prepared by removing a square cut-out from an opaque sheet of paper. Its size was easily calculated from the following relations:

$$d \sin\theta = m\lambda, \tag{8}$$

$$\tan\theta = \frac{y}{f}, \tag{9}$$

where d = periodicity of the grating on the SLM, θ is the angle made by the m^{th} order with the optical axis, λ is the wavelength and y is the distance of the diffraction spot from the center of the Fourier plane. Using the above equations we find y=18.33 mm for the side length of the square aperture of the Fourier filter where m = 1, d = 8 μm and f = 300 mm. Since the SLM is pixelated, the field reflected from it represents sampled data, and any function displayed on the SLM gets diffracted into multiple orders. Without pixel grouping/binning, only the zero order diffraction term was allowed to pass through the Fourier filter. For 2×2 pixel binning, up to first order diffraction terms (0, ±1) were allowed and so on. The fidelity with which a phase function can be

imaged to the conjugate plane is determined by the number of diffraction orders allowed through the system since adequate sampling of the discrete signal requires the inclusion of about eight diffraction orders for good reconstruction. In our experimental setup, system performance should begin to degrade rapidly for segment sizes smaller than 16×16 pixels because this corresponds to eight diffraction orders. In the next section it is demonstrated that performance does indeed degrade for groupings of less than 15×15 pixels (16×16 pixel binning was not used).

When the SLM was addressed with random phases to act as a diffuser, the data reaching the CCD was overlaid with a speckle pattern which obscured the reconstructed image. The extent of obscuration was inversely proportional to the number of pixels grouped together in blocks on the SLM. Placing the rotating diffuser at the image plane of the 4-*f* system was intended to counteract the effects of scattering from the SLM by performing a simple statistical averaging. The importance of precisely imaging the SLM face onto the rotating diffuser cannot be overstated. For this reason, the positioning of the rotating diffuser was critical. Experimentally it was found that small offsets in diffuser position from the imaging plane caused serious degradation of system performance due to fall in the OTF in equation 17.

3.1.4 Results and Discussion

To eliminate the limitation due to numerical aperture and obtain the best image possible in our experimental setup, all the SLM pixels were binned together as one super-pixel. In this case the SLM was a blank screen with uniform phase that behaved like a plane mirror (except for the thin circuit lines around each pixel). With such a blank image on the SLM, we took a long exposure of 0.9 seconds through the rotating diffuser with the camera. By making use of a fast Fourier transform (FFT) algorithm in MATLAB we then reconstructed the image. Figure 22 shows the result, which is suitable as a point of reference in the present work. This image may also serve as a point of comparison with the results in ref. 21 since the only diffuser in the system is in motion. Note that the cropped region in figure 22 is used throughout this paper in evaluating other results.

Next, we made two sets of measurements with various groupings of SLM pixels. The first set comprised results obtained without the rotating diffuser in place. That is, the static diffuser (SLM) was in place but there was no possibility of statistical averaging. Results were recorded with bin-sizes of 5×5, 10×10, 15×15, 20×20, 25×25 and 50×50 pixels and cropped reconstructed images are shown in the top row of figure 21. A second set of results was obtained by placing a rotating diffuser at the image plane of the first 4-*f* setup. On the basis of our earlier analysis, this

Binning size	Without rotating diffuser (SSIM)	With rotating diffuser (SSIM)	Percentage improvement in SSIM
5×5	0.0816	0.0894	9.6
10×10	0.0962	0.1912	98.8
15×15	0.1166	0.2618	124.5
20×20	0.1372	0.3103	126.2
25×25	0.1680	0.3108	85.0
50×50	0.1904	0.3932	106.5

Table 1. (Purcell *et al.*, 2016) Comparison of SSIM data for assessing improvement in image recovery.

should improve the image quality. The results are shown in the bottom row in figure 21, opposite the unaveraged images for the same super-pixel sizes. A visual inspection is sufficient to conclude that, for a given bin size, inserting a rotating diffuser gives an improved result.

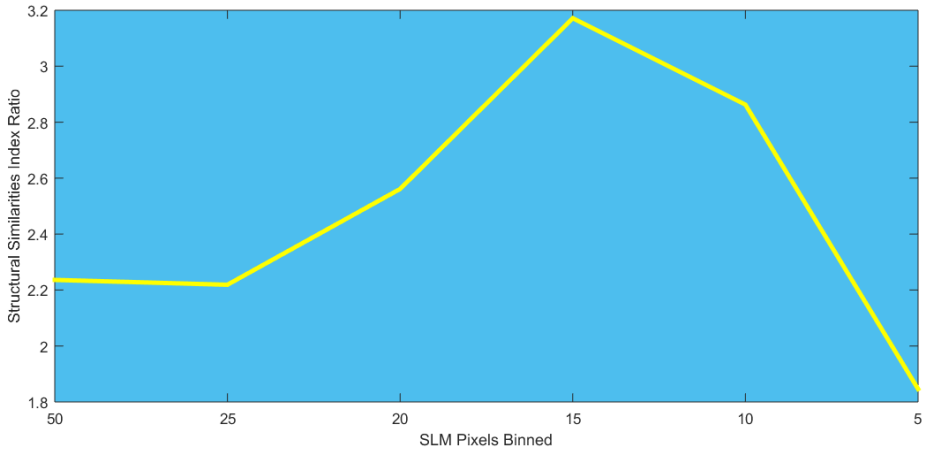

Figure 20. (Purcell *et al.*, 2016) SSIM was calculated for the images collected with rotating diffuser and without. The absolute value of the SSIM may not have intuitive meaning to the reader, so a ratio of two SSIM values was calculated and displayed here to clearly illustrate the improvement achieved with the rotating diffuser. Copyright © 2016 by SPIE.

However the quality of these results can also be evaluated more quantitatively using a numerical procedure.

The structural similarity index [44], [46] was chosen to evaluate image quality. In this method each result is compared to a reference image, such as that in figure 22 [17]. We made use of MATLAB to compute the structural similarity index (SSIM) [46] and have listed the SSIM values for all images in Table 1 [17]. In agreement with the visual impression, the SSIM data confirms that there is a significant improvement in image quality for binning of more than 10×10 pixels. This is a striking confirmation of the theory. Based on the

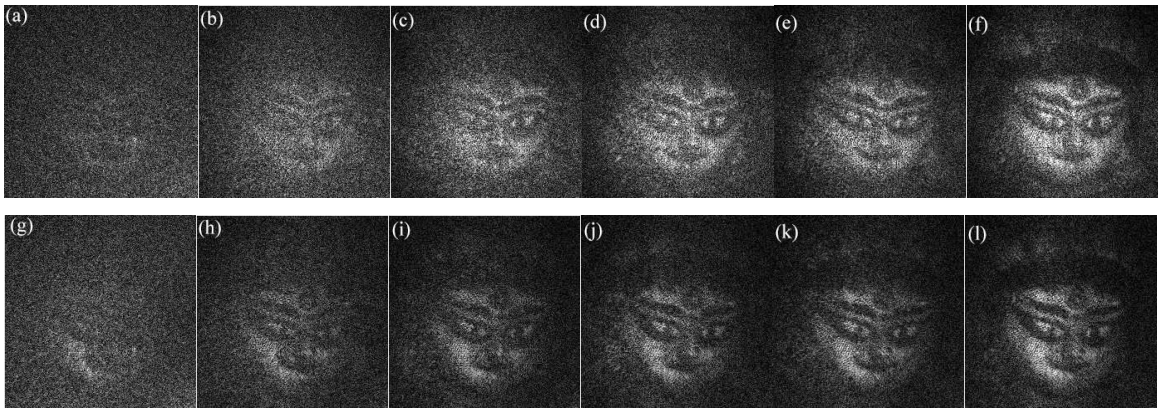

Figure 21. (Purcell *et al.*, 2016) The recovered image comparison for varied pixel binning sizes of 5, 10, 15, 20, 25 and 50 (top to bottom) for two cases: without rotating diffuser in (a)-(f) and with rotating diffuser (g)-(l) in the setup. Copyright © 2016 by Optical Society of America.

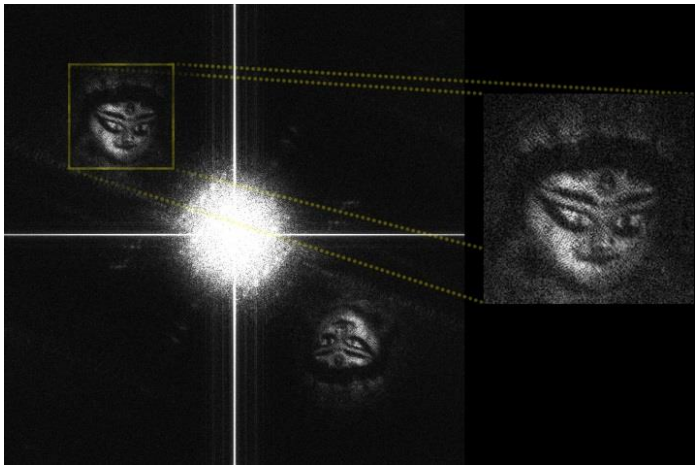

Figure 22. (Purcell *et al.*, 2016) The reconstructed image for the case of blank SLM with rotating diffuser. Inset shows the magnified view of the recovered image which serves as a reference for our analysis. Copyright © 2016 by Optical Society of America.

table, it may be noted further that when more than 10×10 pixels are binned together, the quality of reconstruction does not improve much in the case where a rotating diffuser is not employed. This conclusion is not so obvious, since the series of images presented in figure 21 appear to show substantial improvement to the eye in terms of quality of recovered image [17]. Upon closer inspection it may be verified that it is only larger features of the image which show improved recovery for pixel groupings above ten. Since the SSIM index evaluates similarities down to the individual pixel level, it provides a more globally accurate assessment of image quality than is possible with the unaided eye. One may be interested in knowing why the recovery of images even with rotating diffuser worsens with reduction in the pixel binning size. This has to do with the impulse response function $h_0(\xi, \eta)$ of the imaging optics between SLM and rotating diffuser as discussed around equation 12. As the binning size of SLM is reduced, the variation of wave-field beyond this SLM (random static diffuser) becomes fast enough in comparison to the impulse response function $h_0(\xi, \eta)$ leading to its approximation as a delta function no more valid. This in turn makes the assumption of field just after second diffuser being same as hologram function multiplied by a random phase only function (as expressed in Eq. (4)) invalid. Thus the intensity recorded by camera can no more represent the hologram accurately tending to no recovery of the object information. For this very reason the recovery of object information became negligible for binning size of lesser than 5×5 pixels. While the set of experiments helps in understanding and verifying these implications, it is pretty straight forward

to understand that the requirement of imaging through a smaller binning size would require a narrower impulse response function $h_0(\xi, \eta)$. This is achievable by using a higher numerical aperture and better aberration compensated optics.

In order to add more value to our conclusion that introduction of additional moving diffuser helps in recovery of smaller features from the object, we replaced the object with a USAF resolution target and repeated same experiments. The SLM binning size was kept at 5×5 pixels. The setup was kept the same and the Fourier holograms were captured in the camera with exposure time of 0.23 seconds. Here, a relatively lower exposure time was possible due to the choice of ND filters in the setup which ensured the availability of sufficient light intensity even at lower exposure time. Once again the images were reconstructed by a single fast Fourier transform (FFT) operation on the recorded images. Figure 23 shows the reconstructed images of this experiment [17]. It is clearly seen that for a given bin size, introduction of a rotating diffuser leads to improved imaging and recovery of smaller feature size.

In addition to the experiments described above, we attempted image recovery after sandwiching the object between static diffusers. This situation closely resembles that of an object embedded within a scattering medium where plane wave illumination is not possible. Figure 24 shows the schematic representation of this setup. Another 600-grit ground glass diffuser (Thorlabs DG20-600-MD) was introduced in such a way that the object lies between static diffuser 1 and the SLM which again serves as a reconfigurable static diffuser 2. The rest of the setup was unaltered and

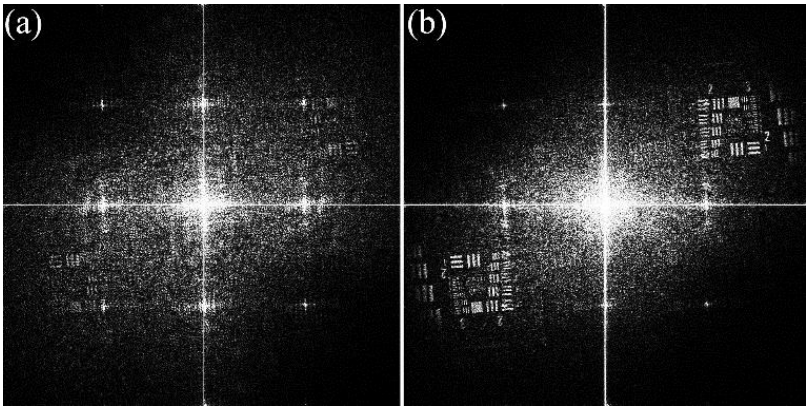

Figure 23. (Purcell *et al.*, 2016) The reconstructed image for the case of blank SLM with rotating diffuser. Inset shows the magnified view of the recovered image which serves as a reference for our analysis. Copyright © 2016 by Optical Society of America.

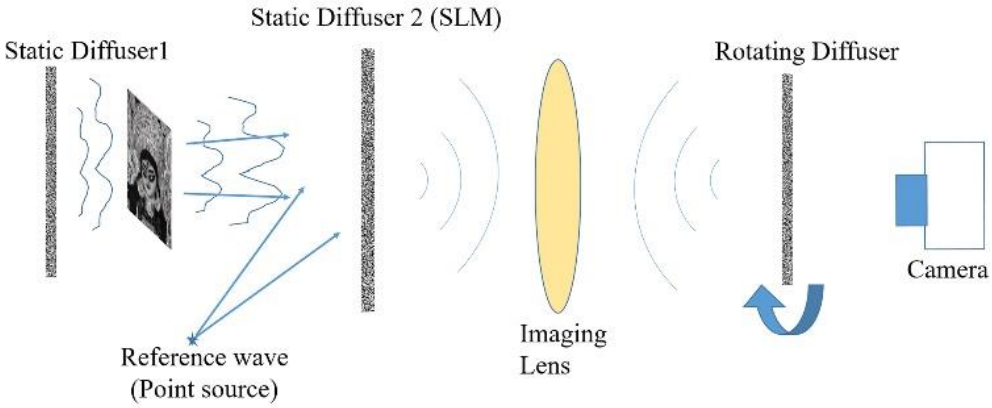

Figure 24. (Purcell *et al.*, 2016) Schematic of the experiment for imaging an object sandwiched between two static diffusers. Copyright © 2016 by Optical Society of America.

the detection and image processing remained the same. Images were again recorded for different pixel bin sizes on the SLM. A trend similar to that obtained in the previous case was found. Figure 25 shows the result associated with a bin-size of 15×15 pixels. The SSIM index evaluation of recovered images in this case gave values of 0.0260 without the rotating diffuser and 0.0345 with the rotating diffuser. It is clear that introduction of a rotating diffuser again improves the results through statistical averaging although overall image quality noticeably worsens when compared with recovered images from experiments with a single static diffuser (listed in Table 1). This is to be expected, since in the case of an object sandwiched between diffusers the illumination is by a speckle field. Hence it is illuminated non-uniformly. However, this is not an insurmountable or fundamental issue, because modulation of the incident beam could be used to make the object illumination more uniform whenever data collection is time-averaged. While all the improvements in imaging reported here are purely due to the advantages of the optical method itself, it is obvious that additional improvements in the technique could result from further computer processing.

The main limitation of the technique reported here arises from the challenge of precisely imaging the static diffuser onto the rotating diffuser. In practice, this limits the binning size of pixels in our experiments. We were able to work only with pixel groupings down to about ten pixels while maintaining acceptable image recovery. The size of a super-pixel containing ten pixels on our SLM corresponds to scattering centers with approximate diameters of 80 μm. As a limiting grain size of scattering centers, this is much bigger than what is representative of standard diffusers or

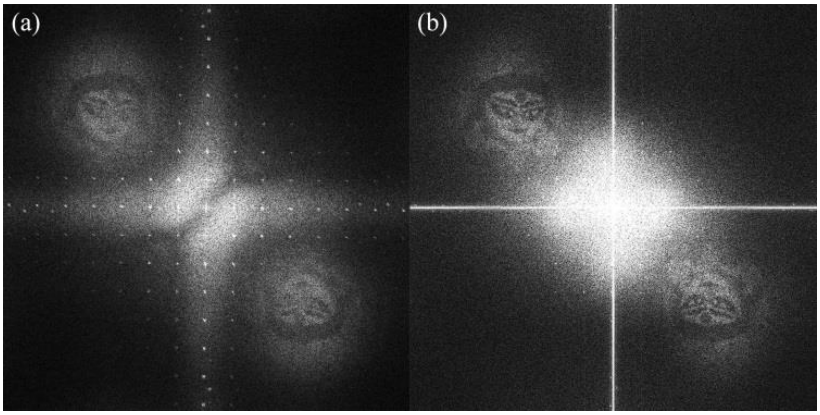

Figure 25. (Purcell *et al.*, 2016) The recovered image comparison for 15×15 pixel binning size in case of object sandwiched between two-diffuser configuration. Two cases: without additional rotating diffuser in (a) and with additional rotating diffuser (b). Copyright © 2016 by Optical Society of America.

tissue phantoms. On the other hand this is a limit which can readily be overcome to allow one to image through a regular diffuser. For example the imaging optics in our setup can be replaced with high numerical aperture lenses/microscope objectives to make the technique practical in scattering media with smaller effective scattering centers.

Only the imaging system situated between the static and rotating diffuser needs to be perfect. The camera itself does not need to incorporate high numerical aperture optics. Moreover, it is possible to combine our approach with one proposed by Goodman [28] to improve it further. As shown by Goodman, for Fourier transform based holographic recording, as the distance to the sensor (photographic film in his case) is reduced, it is possible to record the hologram perfectly. This effect could be adapted in our approach to overcome the limit on optical imaging outlined above. By placing the rotating diffuser very close to the static diffuser and imaging the rotating surface on a camera with low numerical aperture optics, the need for high numerical aperture imaging could be eliminated altogether. In this scenario additional unanticipated applications would even be enabled. For example, the use of a sacrificial rotating diffuser might make it possible to image through corrosive or adverse environments where the placement of a sensor next to a containment wall might not be feasible. Unlike several recent imaging methods which utilize high order correlations or memory effects [39, p.], [40], the general approach described here is capable of imaging macroscopic objects. Other advantages of this approach include its speed, which is limited only by the speed of rotation of the diffuser and amount of available light. In our experiments, the diffuser was rotated at 200 RPM and no direct effort was made to

maximize the light throughput. This resulted in an exposure time of approximately 0.23 second (for the results with USAF resolution target in figure 23). At higher rotation speeds and higher light intensity, the required exposure time can be greatly reduced. It is possible to extend the method for non-holographic imaging as well where one uses the object wave alone. But in such a case the phase information of the object wave is lost and one would need to make use of a Fienup-type iterative algorithm to reconstruct the object which is time consuming. In our holographic imaging approach, since the reconstruction process involves only a single FFT operation on the acquired data, imaging at video refresh rates should be possible. The holographic approach opens up the possibility of imaging phase part of objects as well along with its amplitude. Finally, our method has no wavelength-dependence, so it could be implemented at microwave, radio or acoustic frequencies, enabling new applications in many fields.

3.2 Enhancing Transmission of Light in Scattering Media by Iterative Phase Optimization

3.2.1 Introduction

A new method for iterative improvement of transmission through a strongly scattering sample is presented. This method uses a phase-conjugate mirror and a steepest descent algorithm for converging to the optimum wavefront for transmission. Backscattered light is analyzed to provide feedback for improving the wavefront phase profile, which makes the method non-invasive. Control over the wavefront is applied using a reflective spatial light modulator. While enhanced transmission was not successfully demonstrated using this method, suppression of backscattered light by over 35% was achieved using a 626 μm thick sample of Yttria (Y_2O_3) nanopowder (mean particle size 26 nm) in clear epoxy with transport mean free path length of ~116 μm. These results open the door for future work which may lead to a high-speed, non-invasive method for improving the depth of light transmission in strongly scattering media. The theory, methods, and results for this experiment are presented here in a streamlined manner, with the more technical (but still critical) details of calibration and setup of equipment in the appendices of the dissertation to facilitate an easier reading experience.

The enhancement of transmission in strongly scattering media is motivated by the need for focusing and imaging in materials such as biological tissue, in which straight-line propagation of light can only be expected over a very short distance. Long-range propagation of light is also an important issue in free space optics communication and imaging. Such propagation can be easily imagined in glass or vacuum, but is difficult to fathom in materials that are considered opaque. In such materials, densely packed scattering centers deflect the passage of photons so that very few are able to pass through ballistically, and many of the photons may also be absorbed. It is the disorder in the distribution of scattering centers and the variation in the dielectric constant that cause the direction of propagation of individual photons to become randomized. As the ratio of the thickness of the material (in the original direction of propagation) to the transport mean free path length increases, the likelihood of ballistic photons passing through the material becomes

small [47]. Without ballistic photons, there is not a simple one-to-one correspondence between input and output of the optical system which facilitates imaging. Methods for imaging within body tissue have been established, but many of these are limited by the depth of light penetration. Improving the penetration depth of photons may increase the availability of certain techniques for imaging or therapy.

In this new iterative method of enhancing transmission of light, an iterative wavefront phase optimization algorithm addresses all spatial modes of incident light at once and searches for the optimum wavefront phase profile by a steepest-descent search, an algorithm first proposed by Jin

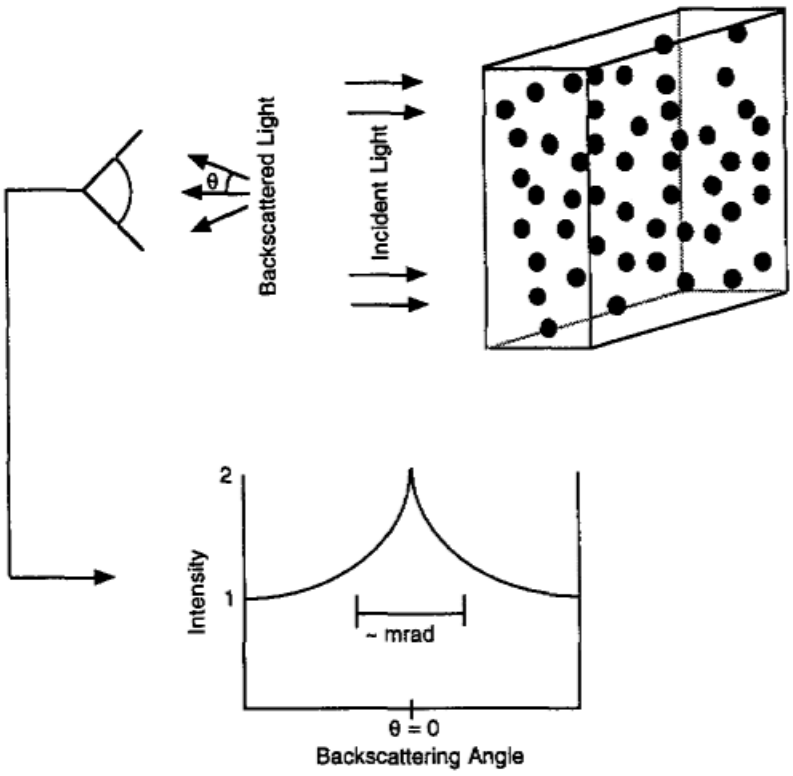

Figure 26. (Corey *et al.*, 1995). A backscattered photon takes a path through the scattering sample which has a special conjugate path, a time-reversed version of its trajectory of scattering events. Another photon following this conjugate path exits where the first photon entered on an anti-parallel trajectory (and vice versa). The phase delay difference between the conjugate paths is a function of the angle of the incident photons with respect to the optical axis and drops to zero for a path parallel to the optical axis, and increases sharply with angle. When photons traverse conjugate paths in this manner, they constructively interfere with one another near the backscattering angle anti-parallel to the optical axis in a phenomenon known as coherent backscattering (CBS). Reproduced from R. Corey, M. Kissner, and P. Saulnier, "Coherent backscattering of light," *Am. J. Phys.*, vol. 63, no. 6, pp. 560–564, Jun. 1995, with the permission of the American Association of Physics Teachers.

et al. (2012) [48]. Feedback for this transmission enhancement method is gathered from backscattered light which can always be collected (unlike some other methods which require feedback from within the sample or behind it). This feedback is not a direct observation of the transmitted power. Instead, backscattered light provides the feedback which makes the method non-invasive to the sample. It has been theorized that decreasing the backscattered power will result in increasing the transmitted power without requiring directly observing it, in the case of perfectly elastic scattering and a unitary scattering matrix [15], [48], [49].

Additionally, the iterative optimization is used on coherently backscattered (CBS) light due to the large portion of photons backscattered near the CBS intensity peak which are multiply scattered. The speckle of the backscattered light has been shown to have a strong intensity peak centered at zero degrees (with respect to the optical axis) and dropping off sharply within a small angle of the optical axis, as shown in figure 26 [50]. The photons contributing to this peak are those which travel the greatest distance within the sample [50]. Suppression of the intensity near the CBS peak is theorized to have the greatest likelihood of enhancing transmission.

3.2.2 Analysis of Enhancement of Transmission of Light in Strongly Scattering Media by Iterative Wavefront Control

The theoretical treatment here was first performed by Jin *et al.* (2012). Consider a two-dimensional slice of a material that is composed of randomly distributed scattering centers. These scattering centers can be thought of as infinitely long cylinders which appear as circles in two-dimensions. A wavefront incident upon the surface of this theoretical sample can be thought of as a vector with phase and amplitude comprising two degrees of freedom describing each of its spatial modes [15], [49]. The scattering matrix of this sample determines how the incident light is scattered and ultimately how it is transmitted and backscattered. The hypothetical sample is infinitely long in the vertical direction and only exists in two dimensions, transmission and backscattering are the only two possibilities [15], [49].

In this series of experiments, the controlling component was a phase-only reflective spatial light modulator (SLM) (Holoeye Pluto VIS – Phase Only) with a liquid crystal display. There was no

Figure 27. (Jin *et al.*, 2012) The scattering system used in development of the iterative transmission enhancement algorithm. The scattering sample is assumed to repeat infinitely in the up and down directions. Photons can only enter or leave the system from the right or left. Light incident from the left is set to zero because all incident light is controlled during the experiment. Copyright © 2012 by IEEE.

direct control over the amplitude of the wavefront, so a phase-only version of the theory upon which the experiments were based was used for wavefront optimization [15], [49].

Given a sample in which all photon scattering is perfectly elastic (no absorption), the existence of transmission pathways which allow all incident energy to pass through the sample has been theorized [24], [51]. In other words, if incident light is guided into the proper channels within the medium, 100% of that power will exit the medium on the far side. Furthermore, there is a connection between incident light which is backscattered and light which is transmitted which makes it possible to predict the amount of the incident light that is guided to these highly transmissive channels by observing the behavior of the backscattered light [15], [48], [49].

In a paper entitled "An Iterative Backscatter-Analysis Based Algorithm for Increasing Transmission Through a Highly-Backscattering Random Medium," (Jin *et. al.*, 2012) the problem was approached using a scattering matrix approach as follows here. Consider a wavefront at a point in space, $\vec{r}$, that is composed of a series of plane waves:

$$a_1^+(\vec{r}) = \sum_{n=-N}^{N} a_{1,n}^+ e^{-i\vec{k}_n \cdot \vec{r}} \tag{26}$$

The incident wavefront can be thought of as a vector with each element of the vector equal to a sum of plane waves multiplied by their modal coefficients, as in equation 26. Using this

formalism, the scattering in the sample can be represented by the scattering matrix, *S*, which is composed of four sub-matrices. Light which exits the sample is considered the output, and light which is incident on the sample from either side is considered the incident light. Equation 27 describes the relationship between the vectorized wavefronts and the scattering matrix (refer back to figure 27 for a physical description of the different vectors).

$$\begin{pmatrix} \vec{a}_1^- \\ \vec{a}_2^+ \end{pmatrix} = \begin{pmatrix} S_{11} & S_{12} \\ S_{21} & S_{22} \end{pmatrix} \begin{pmatrix} \vec{a}_1^+ \\ \vec{a}_2^- \end{pmatrix} \tag{27}$$

This is equivalent to the following, which more clearly indicates the physical nature of the scattering:

$$\vec{A}_{out} = S\vec{A}_{incident} \tag{28}$$

The transmitted light, $\vec{a}_2^+$, is dependent on $\vec{a}_1^+$ (the light incident from the negative z-axis on the sample) and the submatrix S_{21} as shown in equation 29. The power of the transmitted light can be maximized by finding $\vec{a}_{opt}$(the incident wavefront) which maximizes the norm of $S_{21}a_1^+$.

$$\vec{a}_2^+ = S_{21}a_1^+ \tag{29}$$

$$\vec{a}_{opt} = argmax\|S_{21}a_1^+\|_2^2 \tag{30}$$

The sources of light are controlled so the light incident from the positive z-axis on the sample, $\vec{a}_2^-$, is negligible and is treated as zero. The elements of S_{12} and S_{22} are also zero, so the only two submatrices that must be considered are S_{11} and S_{21}. In a material with no absorption (perfectly elastic scattering), the scattering matrix *S* is unitary,

$$S^H S = S_{11}^H S_{11} + S_{21}^H S_{21} = I \tag{31}$$

In the case of a unitary scattering matrix, maximizing the norm of $S_{21}a_1^+$ is equivalent to minimizing the norm of $S_{11}a_1^+$.

$$\vec{a}_{opt} = argmin\|S_{11}a_1^+\|_2^2 \tag{32}$$

Combining this with equation 33, this shows that in order to maximize transmitted power, it is sufficient to minimize the power of the backscattered light, $\vec{a}_1^-$.

$$\vec{a}_1^- = S_{11}\vec{a}_1^+ \tag{33}$$

Theory suggests that there is always an incident wavefront which will transmit perfectly through the sample. These wavefronts are known as Eigen modes of the S_{21} matrix. Taking the singular value decomposition of the S_{11} matrix,

$$S_{11} = \tilde{U}\tilde{\Sigma}\tilde{V}^H \tag{34}$$

It is evident that the set of right singular vectors of S_{11} is a set of vectors each associated with the singular values of S_{11}. The singular values can be thought of as the factor by which the length of the singular vectors is changed by S_{11}. The length of the resulting vector is representative of the

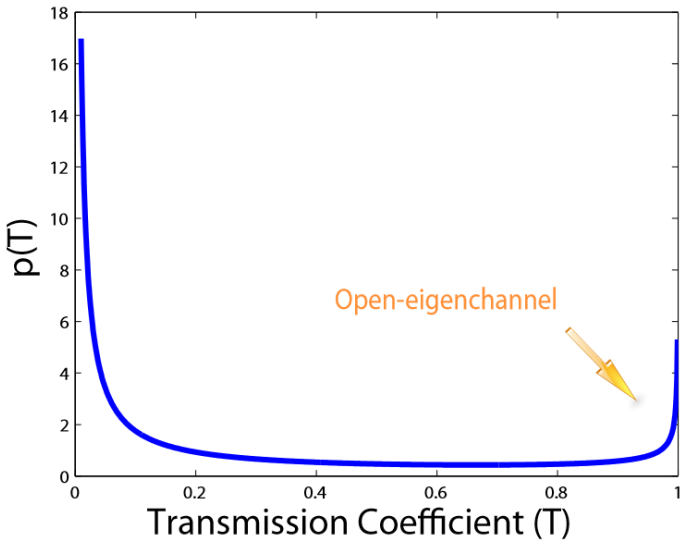

Figure 28. (Jin *et al.*, 2012) Transmission coefficient distribution of a slab of strongly scattering material. Most of the coefficients are small, but there are some coefficients near one. Copyright © 2012 by IEEE.

power stored in the fields of the scattered light. Finding the incident wavefront represented by the right singular vector associated with the smallest singular value of S_{11} will minimize the power of backscattered light, thereby maximizing the transmitted power. Figure 28 shows the theoretical distribution of the singular values of the forward scattering matrix, S_{21} (also known as transmission coefficients) [48]. Although the exact distribution of the transmission coefficients is dependent upon several factors such as the depth of the sample and the transport mean free path length of the material, the "bathtub" shape of the curve remains the same for all strongly scattering samples. Despite a large number of transmission coefficients that are near zero and many that are much smaller than one, there are always some which approach one. This implies that there always exists an incident wavefront that will be transmitted completely through each sample (assuming no absorption), although it should be noted that as the thickness of the sample increases and the transport mean free path length decreases the fraction of wavefronts with transmission coefficients close to one becomes very small.

Since it has been established that the optimum wavefront is the smallest right singular vector of S_{11}, the optimum wavefront could, in principle, be found by calculating the singular value decomposition of S_{11}. This would require the elements of S_{11} to be known, but experimentally the process of finding these elements would be very lengthy. It would require one measurement of the backscattered light for each element of the matrix, and it would require the incident light vectors for each measurement to be orthogonal with respect to each other. If the target for transmission enhancement is a dynamic medium with a short persistence time, this approach would not be effective. Instead of calculating the optimum wavefront directly, a more practical method is to perform an efficient iterative improvement of the wavefront that requires much fewer measurements than the number of elements in the scattering matrix and converges rapidly to the optimum wavefront. A steepest descent algorithm was used, which was first proposed for the purpose of enhancing transmission by Jin *et al.* (2012). A detailed description of the algorithm is included in appendix 1. The physical implementation of the algorithm is described in the following subsection, 3.2.3.

3.2.3 Methods for Enhancing Transmission of Light

Iterative transmission enhancement was experimentally implemented as the physical analog of the steepest descent algorithm presented by Jin *et al.* (2012) [48], which is displayed in table 2 in appendix 1. The steepest-descent search for the optimum incident wavefront for transmitting light through the sample can be simplified to several steps which are repeated until a satisfactory result (suppressed backscattered power and improved transmission) is achieved. First, a random wavefront phase profile is generated and imparted to the signal beam by the SLM (this only happens once, at the beginning of the process). The wavefront is then incident on the sample, and backscattered light from the sample is sensed by the camera. The camera and the SLM form a type of phase conjugate mirror, which measures the phase profile of the backscattered light and generates a time-reversed version of the wavefront, sending it back to the sample. The backscattered light from the sample again falls on the camera, its phase profile is measured and a time-reversed wavefront is generated and directed to the sample. The final backscattered light is recorded. The information recorded during this process is then used to update the original wavefront (which began as a randomly generated phase profile), taking one "step" toward the optimal phase profile along the steepest slope of the optimizing function (the gradient of the total backscattered power as a function of the incident wave vector elements). This updated wavefront becomes the starting part for the next iteration of the process. As each iteration is completed, the measured backscattered light decreases and the transmitted light is measured. The details of this process follow.

The scattering sample was a 626 μm thick layer of Yttria (Y_2O_3) nanopowder in clear epoxy with average particle size of ~26 nm and transport mean free path length of ~116 μm, deposited on a microscope slide and covered with a glass slip. The source was a 200 milliwatt CW OPSL (Coherent Sapphire) centered at 488 nm. The output of the laser was vertically polarized and single mode (TEM_{00}). The phase control method was a reflective SLM (Holoeye Pluto-VIS) which was calibrated and tested first (see appendix 2 for details of this process). An electro-optic modulator was used to control the phase of the reference beam and was also calibrated and tested extensively (see appendix 3). The calibration and testing process for these pieces of equipment was not trivial, but that portion of the setup has been relegated to the appendices to facilitate a

better understanding of the experiment first without allowing the details to make for an unnecessarily difficult read.

The setup is shown in figure 29. A half waveplate rotates the polarization of the laser output to the desired angle to balance power between the signal and reference beams. The signal and reference beams were created by passing the beam through a polarizing beamsplitter, which transmitted horizontally polarized light (signal beam) and rejected vertically polarized light (reference beam). The signal beam passed through a beam expander so that it would fill the face of the reflective SLM. The SLM imparted a random phase profile to the signal beam at the beginning of the experiment.

The signal beam was directed into a 4f imaging system in order to reduce the size of the beam before entry into a microscope objective. Any signal beam falling outside of the objective's entrance aperture was unused for the experiment; reducing the size of the beam maximized the number of controllable segments of the wavefront that were imaged onto the surface of the sample.

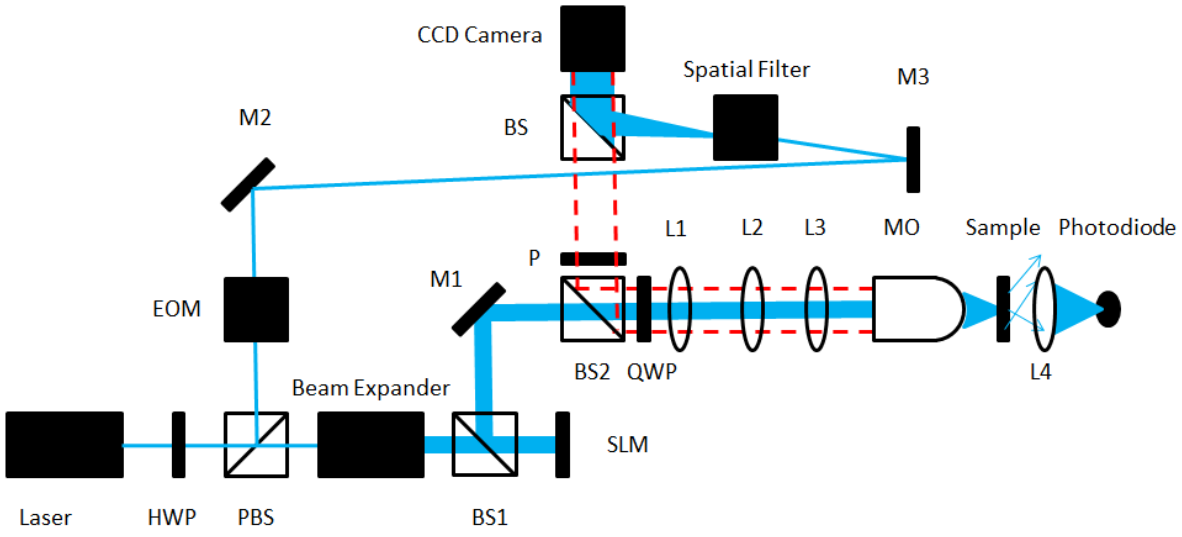

Figure 29. Experiment setup for transmission improvement. The dashed red lines indicate the path of backscattered light from the sample. HWP – half waveplate; QWP – quarter waveplate; SLM – spatial light modulator; BS – non-polarizing beamsplitter; EOM – electro-optical modulator; M – aluminum mirror; L – converging lens; MO – microscope objective; P – polarizer; PBS – polarizing beamsplitter.

Transmitted light was collected by a lens with large numerical aperture to the extent possible (although collection of all light was not practical). The lens focused the light onto a photodiode so that the power could be measured with a digital multimeter (DMM).

Backscattered and reflected light was collected by the microscope objective (40x) and traveled back through the 4f imaging system. Part of the backscattered light was directed toward the CCD camera (Andor iXon 885 EMCCD) via a beamsplitter. This beam combined with the reference beam on the CCD sensor to form an interference pattern which facilitated the measurement of the phase profile of the backscattered light. In order to measure the phase information, it was necessary to provide a flat reference wavefront at four different phase delays with respect to the signal beam. This process is known as phase-shifting digital holography (see appendix 4 for greater detail regarding this process). The phase delay was imparted by an electro-optical modulator (EOM) which the reference beam passed through. The reference beam was then passed through a spatial filter and subsequently collimated so that the beam was large enough to cover the CCD sensor and uniform in intensity.

A quarter wave plate and polarizer combination was used to isolate the portion of the signal beam that experienced multiple scattering within the sample, which helped to mitigate light reflected from optics and from single scattering events (see appendix 5 for greater detail).

The propagation distance from the SLM to the second beamsplitter (see figure 29) was made to match the distance between the beamsplitter and the CCD sensor, so that differences in propagation distance did not have to be accounted for between the measured wavefronts at the CCD and the phase conjugate wavefronts produced at the SLM. Ultimately, the wavefront traveled the same distance from the sample to the CCD as from the SLM to the sample. Should such an experiment be designed without this consideration built into its geometry, the difference in wavefront propagation would need to be accounted for, since the wavefront evolves as it moves (see appendix 6 for more detail). The goal of measuring and phase-conjugating the wavefront was to produce a time-reversed signal at the surface of the sample, so if the wavefront had propagated a different distance its shape would have changed and it would no longer meet the parameters of time-reversal.

A brief side-track was taken to test whether overall transmission could be improved using the iterative phase optimization methods of Vellekoop and Mosk (2007). Rather than maximizing power delivered to a focal point, however, the total power was maximized. This was done using the same setup that was used for enhancing transmission of light by steepest descent algorithm, and resulted in a transmission improvement through the Yttria powder sample by as much as 13%.

3.2.4 Results and Discussion

Iteratively increasing transmission of light through a sample of Yttria powder in clear epoxy (~26 nm mean particle size, ~116 μm transport mean free path length, ~626 μm thick) by analyzing backscattered light was attempted 20 times. Measured backscattered power was reduced by as much as 35% with no corresponding increase in transmitted power. Randomized polarization of the scattered light may be a significant factor in the lack of increased transmission. Still, a measure of control over the scattering of light within the sample was demonstrated by analysis of backscattered light alone, and this may open the door to improving transmitted power in future experiments by a very similar method.

During each run of the experiment, the physical implementation of the steepest descent algorithm based on phase-only wavefront modulation presented by Jin *et. al.* (2014) was performed in multiple iterations, with the wavefront phase output from the first iteration used as the input to the next iteration. Each run resulted in decreased backscattered intensity measured at the camera, but there was no measured increase in transmitted intensity at the photodiode where the transmitted light was focused by a collecting lens. The rate of intensity decrease seemed to match the simulated data by Jin *et. al.* (2012, 2013, 2014). Experimental results showing measured backscattered power agreed well with simulation of Jin *et al.* (2012, 2013, 2014), which predicted that most of the changes in backscattered power would occur in the first four iterations in each experiment. The differences may be accounted for by using a non-optimal step size, μ, in the steepest descent algorithm. Experimental data shows that backscattered intensity as a function of number of iterations of the steepest descent algorithm has a positive second

derivative, which is in agreement with predictions. However, the decrease in backscattered intensity did not result in a measurable increase in transmitted intensity during any run of the experiment.

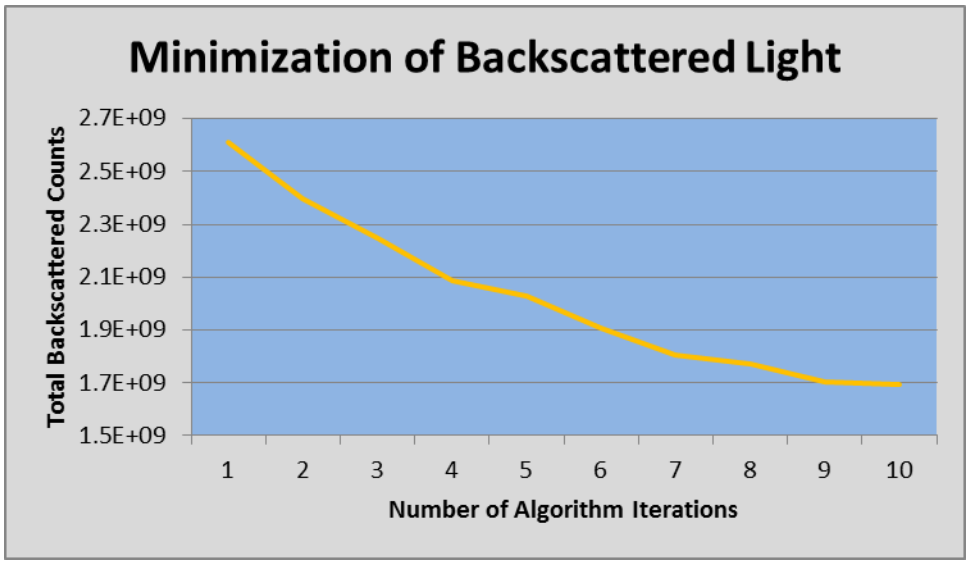

Figure 30. Total backscattered counts on the CCD sensor. The total counts decreased with each iteration of the steepest descent algorithm.

There are several possible explanations for these observations. The experiment differs in many aspects from theory. Practical implementations of the theory [15], [48], [49] have problematic shortcomings in light collection. For example, large portions of the light exiting the sample cannot be collected, and polarization randomization of scattered light presents a major hurdle as discussed below.

The theory that is the basis for this work is developed from a two-dimensional system which is infinite in two directions; the only places that light can enter or exit the theoretical scattering medium is on one side or the other of the infinite slab. It is assumed that all of the backscattered light is measured, and that all of the light transmitting through the system is also measured.

In the lab environment, it is impossible to collect all of the light that exits the sample. A lens which could collect all of the backscattered light would need to have a very large aperture and a nearly perfect numerical aperture. If the lens is not large enough in aperture, the backscattered

light can exit the medium far from the optical axis of the collection lens and well outside of the lens aperture. It may also be propagating at any angle as it exits the medium. When the light exits the medium near the optical axis of the lens some of it exits at a sharp angle away from the lens. Light that does travel toward the lens from a point that is relatively far from the optical axis of the lens does so at a large angle, such that a lens with a small acceptance angle will not capture it. The same problem occurs on the transmission side of the medium. In real samples, however, there is also the possibility that light can escape on a side that is perpendicular to a radial line from the optical axis. These faces are not considered in the theory, where the sample is instead sandwiched between two infinite planes normal to the optical axis. In the theoretical model, all of the light must exit the sample at some point.

In theory, perfectly elastic scattering is also assumed. Most real world media are not composed of perfectly elastic scatterers, though many materials are considered strongly scattering, meaning that the scattering length is much shorter than the absorption length for a given wavelength of light. As the number of scattering events increases for each photon, the probability of being absorbed increases. This means that as photons are forced to go deeper into a sample, they are more likely to be absorbed than photons which travel short distances and only experiences a few scattering events. Although this is not likely to have been the most significant factor in failing in increase transmitted power, it does bear consideration since it is a departure from theoretical assumptions.

The theory presented by Jin *et. al.* (2012) is predicated on conservation of energy [48]. Given an arbitrarily thick sample, the total power being transmitted through the sample is the difference between the total power incident upon the sample and the total power of the backscattered light. This assumption allows manipulation of the depth of transmission of light within the material. Since there is a finite amount of light energy entering the sample during a given time period (an amount which can reasonably be assumed to be constant over time), changes in the amount of backscattered power theoretically have a direct effect on the transmitted power. Decreasing the backscattered power should cause the transmitted power to increase, and increasing the backscattered power should cause the transmitted power to decrease. It follows that minimizing the backscattered power will result in maximizing the light that is transmitted.

When it is not possible to collect all of the light exiting the sample, however, the assumption that energy is conserved in this system breaks down because the system is not closed. Open systems do not necessarily obey the conservation of energy principle. If our system is an open system, decreasing the power of the backscattered light does not necessarily result in increasing transmitted power.

To add to this, the backscattered light from the sample in this experiment has been selected for photons that go deeper within the sample and undergo a larger number of scattering events. This was accomplished by using a quarter waveplate and a polarizer. The light entering the sample was RHCP. As light propagated into the sample, the photons which were backscattered in a single scattering event experienced a shift to LHCP (as well as those that were reflected from the surface of the sample and the optical elements). By traveling back through the quarter waveplate, the light was converted to linearly polarized (see section) and filtered through a polarizer, which eliminated the linear polarization associated with LHCP light from the sample (or reflected from the surface of system optical elements).

The assumption that circularly polarized light maintains its polarization for multiple scattering events is not absolutely correct. Circularly polarized light maintains its polarization *for a greater number of scattering events, on average* when compared to linearly polarized light [52]. If the light experiences enough scattering events, even light which began as circularly polarized will eventually have a randomized polarization [52]. This has significant meaning for the transmission experiment: the light contributing to the measurement of backscattered power is limited to light of only one polarization, even though much of the light that is of interest has been polarized in a different manner. As the backscattered light is minimized, it is really only the power of one polarization which is being minimized. There is no way to know how the power in the backscattered light is affected in total. As measured backscattered power is decreased, it is possible for the power of the unmeasured light to increase.

Looking again at the results of this experiment, if the measured backscattered power is minimized without being accompanied by an increase in transmitted power, it follows that there

must be more power in the uncollected light exiting the system and the backscattered light which is unaccounted for due to its randomized polarization. To put this in the wording of the theory of Jin *et al.* (2012), the scattering matrix representing the system under consideration is not unitary due to the energy which escapes the system.

If polarization presents so many problems for measurement, is it really necessary to filter out some polarization of backscattered light? Unfortunately, using a polarization filter is necessary. Polarized light is necessary for measuring the phase of the light. Interference between the reference beam and the signal is necessary to measure the phase of the backscattered light using phase-shifting digital holography. Interference requires the light reaching the CCD to have the same polarization as the reference beam. Reflections from optics in the setup can also be very problematic by overpowering the relatively dim backscattered signal, and these reflections can be significantly reduced with polarization selection. Hence we conclude that polarization selection is a necessary ingredient of digital holography which unfortunately prevents image correction in the presence of polarization scrambling from strongly scattering samples.

Despite measuring no increase in transmitted power in this experiment, earlier experimental results using the same setup showed that improvement in overall transmitted power is possible by wavefront phase modulation. Maximizing overall transmission using classic wavefront optimization and feedback from the transmission side of the sample resulted in an improvement in transmission of up to 13%. These results suggest that the present implementation of the theory presented by Jin et.al. (2012) fails to converge to a high transmission solution although one apparently exists [48]. This failure is most likely due to polarization scrambling in the experiments performed here. On the other hand the theory does predict a reduction of backscattered intensity in a small number of iterations, consistent with the experimental observations.

3.3 Focusing Backscattered Light by Iterative Phase Optimization

3.3.1 Introduction

During the course of pursuing enhanced transmission of light in the primary experiment of this dissertation (discussed in 3.2), it was necessary to establish that the methods of controlling a reflective spatial light modulator (SLM) and the phases of the wavefront of light incident upon the samples used were effective. The most definitive way to do so was to ensure that the phase control was precise enough to reproduce the phase optimization experiment of what has become a highly-regarded and often-cited paper entitled "Focusing Coherent Light Through Opaque Strongly-Scattering Media" by Vellekoop and Mosk (2007) [13]. The work of Vellekoop and Mosk (2007) demonstrated that incident light could be guided into preferential channels within a strongly scattering sample by controlling its phase. In that experiment (which was reviewed in section 2.1) the authors demonstrated the ability to focus coherent light through a sample composed of densely packed scattering centers by iterative phase optimization.

During the successful reproduction of the Vellekoop and Mosk experiment (2007), a new geometry for focusing coherent light was also demonstrated [13]. In the original experiment, light was focused within or behind a sample. Expanding upon these results, it was proposed that focusing through phase optimization should be possible using backscattered light as well. This discussion will concentrate on the results of establishing iterative wavefront phase optimization for focusing of backscattered light.

The characteristic speckle pattern of coherent light is well-established [53]. This speckle pattern is a result of randomly occurring constructive and destructive interference. The interference is a result of the coherent light experiencing small differences in optical path length as it travels toward the point of observation. The power from the source is divided into multiple spatial modes which combine with different phase. Control over the phase of each of the modes can be used to create constructive interference between these modes. Instead of randomly distributed pockets of constructive and destructive interference, the modes can be phase-delayed in a strategic manner so that they each contribute to a much stronger instance of constructive

interference in an arbitrary location. In order to understand the effect of phase changes in each of the modes on the strength of the constructive interference, the intensity at the intended focus is observed while varying the phase. Each of the spatial modes is controlled by a segment of a reflective SLM; these segments can be varied sequentially or in groups to find the phase mask that results in the greatest observed intensity. Due to the repetitive nature of this process, it is known as an iterative optimization method.

Iterative phase optimization focusing of backscattered light is a process which varies the phase of a portion of the control segments of the wavefront at once using a reflective SLM. The intention of this experiment was to demonstrate a previously published method for focusing within a scattering sample [13], but in a new geometry in which it is the backscattered light which is brought to focus. The phase optimization is accomplished by treating segments of the SLM individually or in groupings which include no more than half of the total number of segments, while directly observing how changes in the phase of these segments affects the intended outcome (the power delivered to the focus location). This experiment was a byproduct of preparation for enhancing transmission through a scattering sample, as it was necessary to demonstrate precise control of the SLM. Reproducing the results of Vellekoop and Mosk (2007) was determined to be a good means of demonstrating control over the phases of the wavefront segments. However, an opportunity arose to build upon this previous result with a modification to the geometry of the setup. Since this experiment was performed with the intention of verifying proper operation of the SLM, a more sophisticated phase optimization algorithm was not required.

During the course of pursuing enhanced transmission of light by wavefront phase optimization, it was necessary to establish that the methods of controlling the SLM and the phases of the wavefront of light incident upon the samples used were effective. The most definitive way to do so was to ensure that the phase control was precise enough to reproduce the phase optimization experiment of what has become a highly-regarded and often-cited paper entitled “Focusing Coherent Light Through Opaque Strongly-Scattering Media” [13]. This was the seminal work upon which many experiments and papers have built since its publication in 2007. In that experiment (which was reviewed in section 2.1) the authors demonstrated the ability to focus

coherent light through a sample composed of densely packed scattering centers by iterative phase optimization.

The characteristic speckle pattern of coherent light is well-established [53]. This speckle pattern is a result of randomly occurring constructive and destructive interference. The interference is a result of the coherent light experiencing small differences in optical path length as it travels toward the point of observation. The power from the source is divided into multiple spatial modes which combine with different phase. Control over the phase of each of the modes can be used to create constructive interference between these modes. Instead of randomly distributed pockets of constructive and destructive interference, the modes can be phase-delayed in a strategic manner so that they each contribute to a much stronger instance of constructive interference in an arbitrary location. In order to understand the effect that phase changes in each of the modes has on the strength of the constructive interference, the intensity at the intended focus is observed while varying the phase. Each of the spatial modes is controlled by a segment of a reflective SLM; these segments can be varied sequentially or in groups to find the phase mask that results in the greatest observed intensity.

3.3.2 Analysis of Iterative Phase Optimization for Focusing Backscattered Light

Assume that all of the light reaching the observation point originates from the coherent source in this experiment. In the geometry in question, the light is scattered backward from a sample along the same direction from which the source beam is incident. The field at the observation point can be described mathematically as a sum of spatial modes exiting the sample with phases independent of one another. When a perfectly flat wavefront enters the sample, the phase differences upon exiting are the result of the different path length that each of the spatial modes experiences during multiple scattering events within the sample.

$$E_{tot} = \sum_{n} A_n e^{i\varphi_n} \tag{35}$$

The intensity of this field is what is actually measured at the observation point,

$$I_{obs} = E_{tot}{E_{tot}}^{*}, \tag{36}$$

where ${E_{tot}}^{*}$ is the complex conjugate of the field.

$$I_{obs} = \sum_n |A_n|^2 + 2\sum_{m,n(m\neq n)} A_m A_n \cos(\varphi_m - \varphi_n) \tag{37}$$

Equation 37 may be re-written for a more intuitive understanding as in equation 38.

$$I_{obs} = \sum_n I_n + 2\sum_{m,n(m\neq n)} (I_m I_n)^{1/2} \cos(\varphi_m - \varphi_n) \tag{38}$$

From this equation, it is clear that the observed intensity has a complicated dependence on the phases of the spatial modes. These phases can be changed systematically while observing the intensity until the global maximum is achieved. However, as the positions of the scattering centers within the sample change, the paths of the spatial modes within the sample are changed and the relative phase ϕ of each mode is altered.

In phase space, the observed intensity I_{obs} is a function of the vector $\boldsymbol{\phi}$. A global maximum of this function exists since it is a bounded, continuous function which can be limited to the interval $[0, 2\pi]$ in each dimension of its range. This global maximum value can be approached one step at a time in each dimension of the vector $\boldsymbol{\phi}$ by observing the intensity while holding the phase delay in each other dimension constant. Changes to the phase will result in an increase, a decrease, or no change in I_{obs}. Changes that maximize the increase are saved. The phase in this dimension (which corresponds to one segment of the SLM) is then held constant while another dimension changed.

Random changes in the phase delay of each segment that are not intentionally imparted by the SLM are unwanted because they tend to increase the distance from the global maximum (as in a random walk). Since the phase changes imparted by the moving scattering centers within the sample are completely random, they are detrimental to the optimization process. These random

changes make it necessary to complete the optimization process in a time that is short in comparison with the persistence time of the sample.

3.3.3 Methods of Iterative Phase Optimization for Focusing Backscattered Light

The source was a 200 mW, CW OPSL (Coherent Sapphire) with a central wavelength of 488 nm. The sample was a sheet of standard, white printer paper. The output from this laser was vertically polarized TEM00 transverse mode. The source was split using a polarizing beamsplitter after passing through a half-waveplate. The half-waveplate rotated the vertically polarized output of the laser so that the polarizing beamsplitter transmitted horizontally polarized light and rejected vertically polarized light at a 90 degree angle, where it was used as a reference. Horizontally polarized light was necessary for imparting phase delay on the signal beam using the SLM (which would have no effect on light polarized perpendicular to the long axis of the screen). The half-waveplate could be rotated to change the balance of power between the signal and the reference.

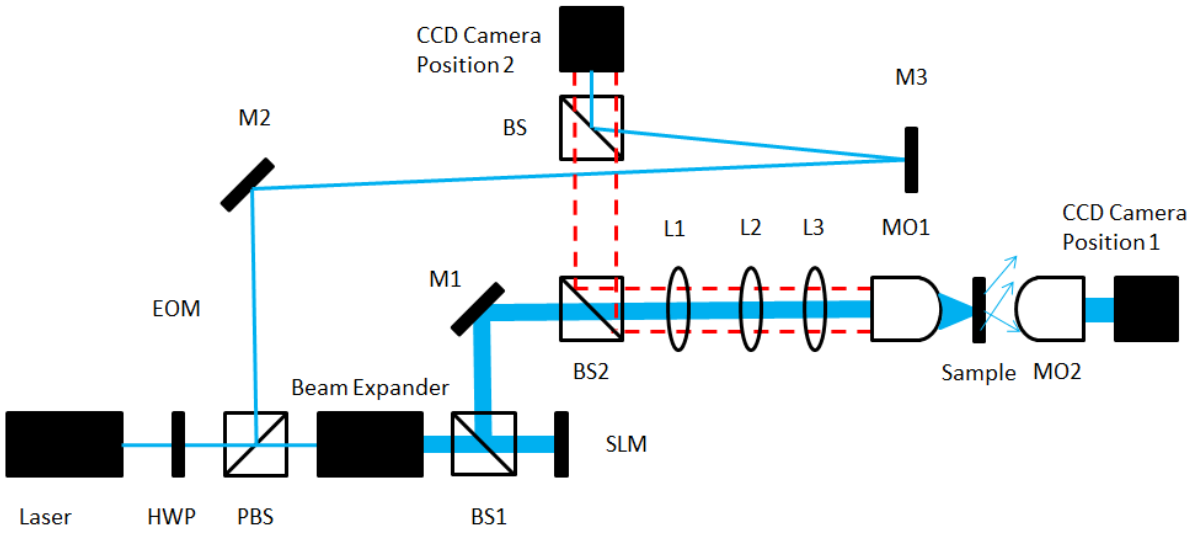

Figure 31. Setup for iterative phase optimization focusing through a strongly scattering sample (camera position 1) and for focusing backscattered light from the sample (camera position 2). The sample was a sheet of standard printer paper. HWP – half wave plate, PBS – polarizing beamsplitter, BS – unpolarized beamsplitter, SLM – spatial light modulator, EOM – electro-optical modulator, M – mirror, L – lens, MO – microscope objective.

The signal beam entered a beam expander so that it was able to fill the face of the reflective SLM. The light reflected from the SLM was directed to a microscope objective where it was imaged onto the surface of the sample. The samples used in this experiment were standard white printer paper, compressed Yttria powder, and a 600 grit ground glass diffuser.

Backscattered light passed back through the microscope objective and was directed to a CCD camera (Andor iXon 885 EMCCD), which was used to provide the feedback for the experiment. A portion of the backscattered signal was blocked so that part of the CCD sensor remained dark. The reference beam was directed to this dark section of the CCD.

The screen of the SLM was divided into segments which were composed of several pixels binned together. While observing intensity at a given location with the backscattered signal beam falling on the CCD sensor, the phase delay imparted by each of these segments was varied between 0 and 2π in several steps. The phase resulting in the greatest observed intensity value was saved for each segment.

The reference beam was needed because of small, random changes in the measured intensity at

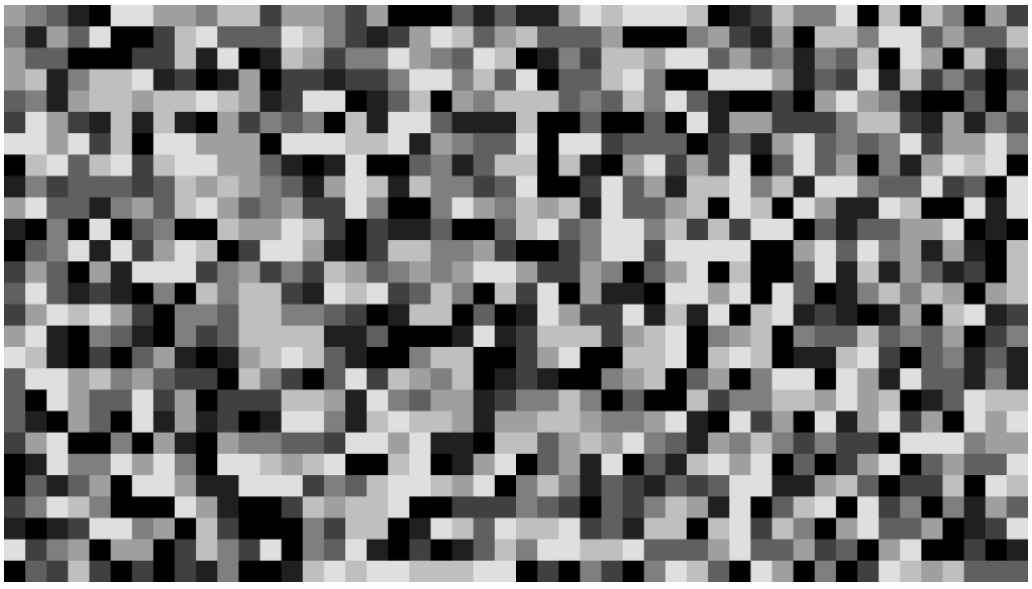

Figure 32. The face of the SLM, divided into segments. The shade of gray is an indication of phase delay imparted on the reflected signal at that location. The SLM was controlled by displaying a bitmap; the value of the grayscale was converted to an applied voltage by means of a look up table stored on the device's EEPROM.

the CCD, which were the result of many factors in the experimental environment such as laser output power fluctuations. Optimization decisions were made based on this observed intensity, and since the power delivered in each segment was small relative to the total power of the signal beam, the expected changes in measured intensity were small relative to the total measured intensity. These small intentional changes in the intensity were frequently within the noise level of the observed signal. Improving the signal-to-noise-ratio was critical to the optimization process, so a reference beam was added. The measured intensity was then divided by the intensity of the reference beam, so that as the power fluctuated the ratio between the two beams remained steady. This allowed the observation of small intentional changes only to the signal beam, which changed the ratio between the signal and the reference.

Phase changes were implemented in two different methods. Using the first method, each segment was altered individually while all other segments were held constant. This method had the disadvantage of a lengthy optimization process. The second method was to randomly select half of the pixels on the SLM face and change them together. Phase changes were again stepped from 0 to 2π in several steps, but this phase value was added to the previous value of each of the randomly selected segments. The observed intensity was maximized, the new values of all of the

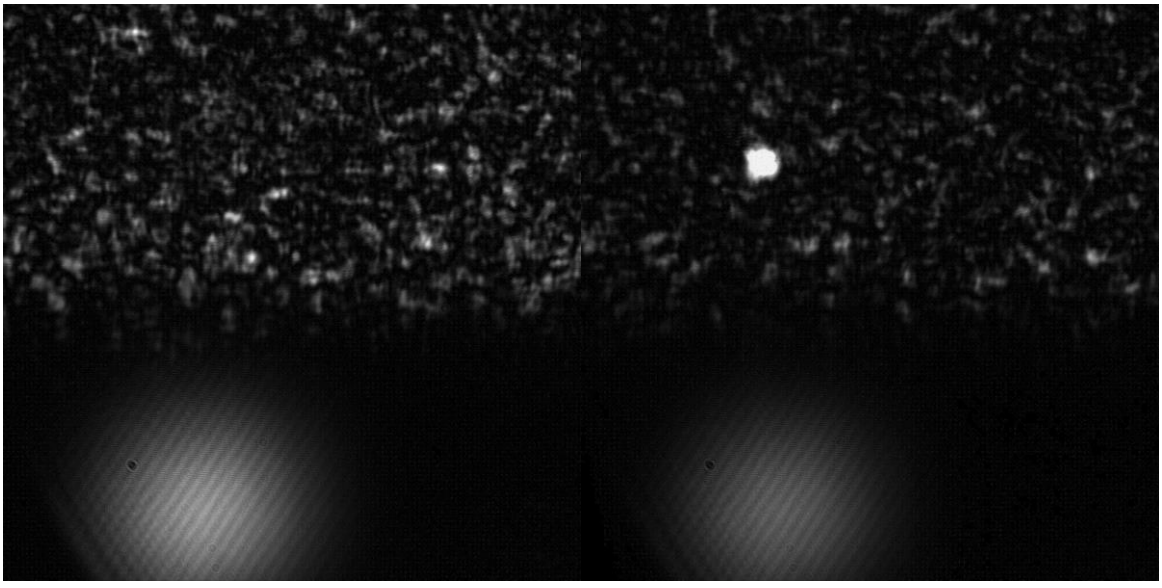

Figure 33. The recorded intensity of backscattered light on the CCD sensor. Left: The SLM displays a blank screen (no phase delay). The backscattered light was blocked from the bottom half of the sensor so that the reference beam could be applied. Right: A bright focus appears after optimization of the SLM segments.

pixels were set to the optimum values, and the process was repeated. This process could be continued if desired until the changes in intensity from one iteration to the next were less than some pre-determined epsilon value. This method had the advantages of speed and large SNR. The improvement in SNR resulted from controlling half of the SLM segments at once. Phase changes were implemented over segments delivering approximately half of the signal beam power, which made them much larger than changes occurring from controlling only one segment at a time.

3.3.4 Results and Discussion

Using iterative wavefront phase optimization, transmitted light and backscattered light were successfully focused from a sheet of standard, white printer paper. Focusing through the sheet of paper was a reproduction of their 2007 results which demonstrated the process using many different types of strongly scattering samples, including a thin layer of TiO_2, an egg shell, a tooth, and more. The focusing of backscattered light by iterative phase optimization was an original result, distinct from the geometry of Vellekoop and Mosk (2007) in which focusing was accomplished within or through several samples.

Backscattered light had never before been focused using phase optimization. Focusing by iterative phase optimization is very robust, although the time required to converge to a solution can be very lengthy (roughly 45 minutes for best results). The phase optimization process was performed in two distinct manners, one in which each segment of a reflective SLM varied the phase of the incident wavefront in sequence, and another in which parallel optimization was performed. During parallel optimization, half of the control segments were varied while the other half were held constant. This greatly improved the signal-to-noise ratio of the intensity changes at the focus. The use of a reference beam on the camera sensor was also critical to improving the SNR so that random intensity noise at the focus was not mistaken for changes caused by the variation of the control segment phase. It was found that the ideal number of phase delay steps for optimization was 8 (the number of steps over which each control segment was varied in phase from 0 to 2π). This allowed for the greatest improvements in power delivered to the intended focus in a reasonable time. Decreasing the size of the phase delay steps beyond $\pi/4$ had

no significant effect on the increase in power delivered to the focus other than significantly increasing the optimization time.

Despite the success of reproducing the Vellekoop and Mosk (2007) experiment, the improvement in intensity was not as great. During the 2007 experiment, an improvement of up to 1000 times the intensity was achieved at the intended focus (above the background speckle intensity). In this reproduction, the maximum improvement above speckle background intensity was around a factor of five. The reason for this was a lack of dynamic power reduction of the source. During the optimization process, the camera pixels saturated after an improvement of roughly five times background, which prevented further increases in intensity due to variations in phase of control segments.

Although the quantitative results of this experiment are worth consideration, the intention of this experiment was to demonstrate control of the signal beam with the SLM while attempting focusing of the backscattered light by phase optimization. Despite limited intensity gain during the focusing process when compared with the 1000 times improvement achieved by Vellekoop and Mosk (2007), the experiment was successful [13]. This experiment was a precursor to enhancing total transmitted power through a strongly scattering sample using iterative wavefront phase optimization, designed to ensure proper operation of the reflective SLM.

Chapter 4: Conclusion and Future Work

Imaging and focusing through strongly scattering media remains a hotbed of research activity. Although the development of many new methods has greatly expanded the availability of imaging and focusing in many scenarios involving scattering media, it is also clear that each of these methods has its disadvantages and limitations. For example, holographic imaging in reflection from a diffusive surface was presented as a novel method by Singh *et. al.*(2014) but was limited by the requirement that the diffusive reflecting surface must be moved for imaging [18]. As another example, time-reversed ultrasonically encoded (TRUE) imaging in biological tissues has been demonstrated as a very effective method, but the imaging depth is limited by the depth of penetration of photons in the tissue [1], [16].

The results of three new experiments were presented in this dissertation as an enhancement of modern methods for focusing and imaging through strongly scattering media. "Focusing Backscattered Light by Iterative Phase Optimization" demonstrated the ability to focus light backscattered from a strongly scattering sample, a new geometry for a method first demonstrated by Vellekoop and Mosk (2007) [13]. "Holographic imaging through a scattering medium by diffuser-assisted statistical averaging" was the second of these experiments which demonstrated the use of a rotating diffuser to mitigate the requirement to move a diffusive reflecting surface in order to image from it. This built upon a previous result in which the reflecting surface was moved in order to perform averaging of the speckle pattern [18]. Finally, in the third experiment "Enhancing Transmission of Light in Scattering Media by Iterative Phase Optimization", enhancement of photon transmission through a thin, strongly scattering sample was attempted using a wavefront shaping algorithm with feedback from backscattered light. This method may work well in conjunction with another technique such as the aforementioned photo-acoustic imaging.

The results of "Focusing Backscattered Light by Iterative Wavefront Optimization", while only a geometrical deviation from previous method which focused through strongly scattering media using wavefront phase optimization, were definitive. Focusing in reflection from three samples including paper, compressed Yttria nano-powder, and a ground glass diffuser was successfully demonstrated. Considering the previous results of Vellekoop and Mosk (2007), it has now been demonstrated that focusing by wavefront optimization can be achieved essentially anywhere that the speckle pattern coherent light can be seen scattering from a sample of strongly scattering media [13].

The results of "Holographic imaging through a scattering medium by diffuser-assisted statistical averaging" show that it is possible to perform lensless holographic imaging in reflection from a diffusive surface without the need for moving the reflection surface. In this experiment, a rotating diffuser was used to provide the statistical averaging that had previously been demonstrated by small movements of the reflection surface. The use of the rotating diffuser for this purpose expands this method of holographic imaging to scenarios where the reflecting surface cannot be moved by performing the statistical averaging at a location that is physically separated from the reflecting surface.

Finally, in the third experiment discussed ("Enhancing Transmission of Light in Scattering Media by Iterative Phase Optimization"), enhanced transmission of light through a strongly scattering sample was not successfully demonstrated. However, reduction in the backscattered power by 35% was demonstrated using a physical implementation of the steepest descent algorithm discussed by Jin *et. al.* (2012, 2013, 2014). It has previously been demonstrated that focusing of light through strongly scattering media is possible by phase optimization of a wavefront [13], [14], [25]. These previous experiments used feedback from behind the sample and did not optimize the phase of the entire wavefront simultaneously. In contrast to this, the results of "Enhancing Transmission of Light in Scattering Media by Iterative Phase Optimization" showed that it is possible to have some measure of control over the scattering of the light within a strongly scattering sample while using backscattered light as the only means of feedback, and to consider the phase of the entire wavefront while doing so. While transmission was not enhanced, the results suggested that the lack of success may be mitigated by addressing

the issue of polarization randomization of scattered light with the sample. If true, this would result in a robust transmission enhancement method that relies only upon backscattered light and converges rapidly. Rapid convergence is a necessity for exploration of media composed of dynamic scattering centers with short persistence times, such as smoke drifting through the atmosphere.

In the transmission enhancement experiment, backscattered light was successfully diminished from a sample of Yttria powder suspended in clear epoxy (~26 nm mean particle size, ~116 μm transport mean free path length, ~626 μm thick) over several iterations of the steepest descent algorithm. It is suspected that this did not result in enhanced transmission in part due to the randomization of polarization of scattered light. Polarized light is used to select the photons that travel deepest into the sample, to facilitate phase measurement by holographic methods, and to mitigate reflections. However, polarization selection means that only a part of the backscattered signal can be measured. Conservation of energy was one of the assumptions of the theory upon which the transmission enhancement experiment is based. If energy is conserved in a system which includes only forward scattering of light and backscattered light, then reduction of backscattered light would necessarily result in an increase in transmitted light. However, conservation of energy is only a valid assumption for a closed system, and backscattered light that cannot be measured is a significant loss in the system that allows energy to escape.

Rather than reject all of the light that is polarized in the wrong direction, this light could be directed to a second camera and filtered by a polarizer set at 90 degrees to the polarizer in the original path. Although this is not enough information to completely determine the Stokes parameters of the light (which completely describe the polarization), the two polarizations would provide a method for measuring the power in all forms of linearly polarized light when combined with a second reference beam matching the polarization of the second light path.

It is also possible that the issue of polarization scrambling could be overcome with a combination of time-gating and angular selection of back-scattered light, although this suggestion goes far beyond the scope of the present work. Similar to the method demonstrated with forward scattering by A. Kuditcher *et al.* (2001), the selection of delayed pulses having a

single exit angle selected by a doubling crystal in the detection arm would be expected to retrieve a signal with a fixed polarization [54]. A bundle of rays with the desired polarization could then be selected by simply rotating the doubler to maximize the signal in the case of a static diffuser. By subsequently applying phase changes on the wavefront controller to minimize the signal, increased transmission could in principle be achieved.

The three new experimental results presented in this dissertation each have some advantages, but are saddled with limitations as well. The new lensless holographic imaging technique provides a very effective method of improving image quality, but the optical system will always have a finite numerical aperture which will limit spatial frequencies that can be captured. Put simply, a significant portion of light will be lost when the reflecting surface has very small features. The new geometry for focusing backscattered light using iterative phase optimization has the disadvantage of requiring feedback from the intended focusing location. The feedback requirement means that the focusing method cannot be used to focus light to an arbitrary point within the backscattered speckle unless a sensor is first placed in that location. Clearly, this places speed and convenience limitations on the technique. Also, using this method, light cannot be focused to a location that does not fall within the backscattered speckle. Light cannot simply be focused to a series of completely arbitrary locations. Finally, the iterative phase optimization method for increasing transmitted power through a scattering sample has several limitations. As discussed, this method has (until the present) not resulted in increased transmitted power. Although there are ways that this might be rectified with future work (also discussed previously), this technique may not lead to the level of fine control that will allow focusing to a specific location within a sample. The increase in transmitted power is more likely to be an effective method for combining with another method that has depth limitations, such as photo acoustic imaging in biological tissue. Still, of these three new results, enhancing the transmission of light through a scattering sample seems to hold the most promise for impacting future research and practical applications.

Imaging and focusing light in or through scattering media is an important goal for many practical applications, including biomedical imaging, astronomy, military applications, and many others. Classic imaging and focusing methods that are effective in vacuum are not effective in scattering

media because frequent scattering events disrupt the ballistic trajectory of almost all incident photons, motivating the development of new methods for imaging and focusing light in these materials. Three new experimental results are presented here which expand upon the current collection of methods for imaging and focusing in the presence of scattering media. Though there have been many important developments in this area, there is no focusing or imaging method that is without limitations and it is necessary to continue to build upon these methods to increase their effectiveness. A lensless Fourier transform holographic imaging method was demonstrated in reflection from a rough surface which uses a rotating diffuser to statistically average the signal. Significant image quality improvement of two images was achieved as measured by the structural similarity index (SSIM), including a maximum of approximately 126 percent improvement in SSIM for images of the Hindu Goddess Durga which were measured with this parameter for comparison. An Air Force Resolution Target was imaged as well, successfully achieving a vast improvement in fine detail that is visible after imaging with this method. In another experiment, focusing of backscattered light by an iterative wavefront phase optimization method was also achieved. With this method, intensity at the intended focus was increased by a factor of approximately five times the speckle intensity at the same location before focusing. This method may easily be extended to generate a much greater increase in intensity at the focus. In the final experiment, a significant decrease in backscattered light from a strongly scattering sample was achieved without feedback from within or behind the sample. In future work, it is possible that this discovery may lead to rapid methods of increasing the transmission of light through a dynamic, strongly scattering sample which makes use of backscattered light as its only necessary feedback.

Appendix 1: Steepest Descent Algorithm

The steepest descent algorithm includes the following steps by Jin *et al.* (2012):

Algorithm Steepest descent for finding $\vec{a}_{opt}$
1: Input: $\vec{a}_{1,(0)}^{+}$= Initial random vector with unit norm
2: Input: $\mu > 0$ = step size
3: **for** $k = 0,1,2,3,\ldots$ **do**
4: $\tilde{\vec{a}}_{1,(k)}^{+} = \vec{a}_{1,(k)}^{+} - \mu S^{H} S \vec{a}_{1,(k)}^{+}$
5: $\vec{a}_{1,(k+1)}^{+} = \tilde{\vec{a}}_{1,(k)}^{+} / \left\| \tilde{\vec{a}}_{1,(k)}^{+} \right\|_{2}$
6: **end for**

Table 2. (Jin *et al.*, 2012) Steps necessary for the steepest descent algorithm. Copyright © 2012 by IEEE.

Table 2 represents the purely mathematical operations required in the steepest descent algorithm. According to Jin *et al.* (2012), the physical equivalent of the vector operations of this algorithm are as follows [48]:

Vector Operation	**Physical Operation**
1: $\vec{a}_1^{-} = S_{11}\vec{a}_{1,(k)}^{+}$	1: $\vec{a}_{1,(k)}^{+} \xrightarrow{Backscatter} \vec{a}_1^{-}$
2: $\vec{a}_1^{+} = F \cdot (\vec{a}_1^{-})^{*}$	2: $\vec{a}_1^{-} \xrightarrow{PCM} \vec{a}_1^{+}$
3: $\vec{a}_1^{-} = S_{11}\vec{a}_1^{+}$	3: $\vec{a}_1^{+} \xrightarrow{Backscatter} \vec{a}_1^{-}$
4: $\vec{a}_1^{+} = F(\vec{a}_1^{-})^{*}$	4: $\vec{a}_1^{-} \xrightarrow{PCM} \vec{a}_1^{+}$
5: $\tilde{\vec{a}}_1^{+} = \vec{a}_{1,(k)}^{+} - 2\mu\vec{a}_1^{+}$	5: $\tilde{\vec{a}}_1^{+} = \vec{a}_{1,(k)}^{+} - 2\mu\vec{a}_1^{+}$
6: $\vec{a}_{1,(k+1)}^{+} = \tilde{\vec{a}}_1^{+} / \left\| \tilde{\vec{a}}_1^{+} \right\|_{2}$	6: $\tilde{\vec{a}}_1^{+} \xrightarrow{Normalization} \vec{a}_{1,(k+1)}^{+}$

Table 3. (Jin *et al.*, 2012) The physical method of implementing each vector operation of the steepest descent algorithm for iterative phase optimization for transmission enhancement. The step size, μ, must be selected and has a value between 0 and 1. Copyright © 2012 by IEEE.

In order to implement the steepest descent algorithm, the physical operations listed in the right-hand column in table 3 (Jin *et al.*, 2012) must be performed in the laboratory [48]. A single

iteration of the algorithm consists of steps 1-6 performed to completion. According to theory, if the correct value of the step size μ is selected, the algorithm should converge to 95% of the maximum possible transmission within 5 iterations [48]. The setup used for the physical implementation is discussed in 3.2.3.

Appendix 2: Calibration and Testing of Spatial Light Modulator

Signal phase delay was controlled using a reflective spatial light modulator (SLM) (Holoeye PLUTO VIS – Phase Only). The SLM is a liquid crystal display which has a varying phase delay proportional to a voltage applied across each pixel along the optical axis.

In order to ensure full control of the wavefront, it was first necessary to establish an accurate relationship between applied voltage and phase delay. This was done using interferometry. The source for this calibration was an OPSL (Coherent Sapphire 488 nm). The beam from this source

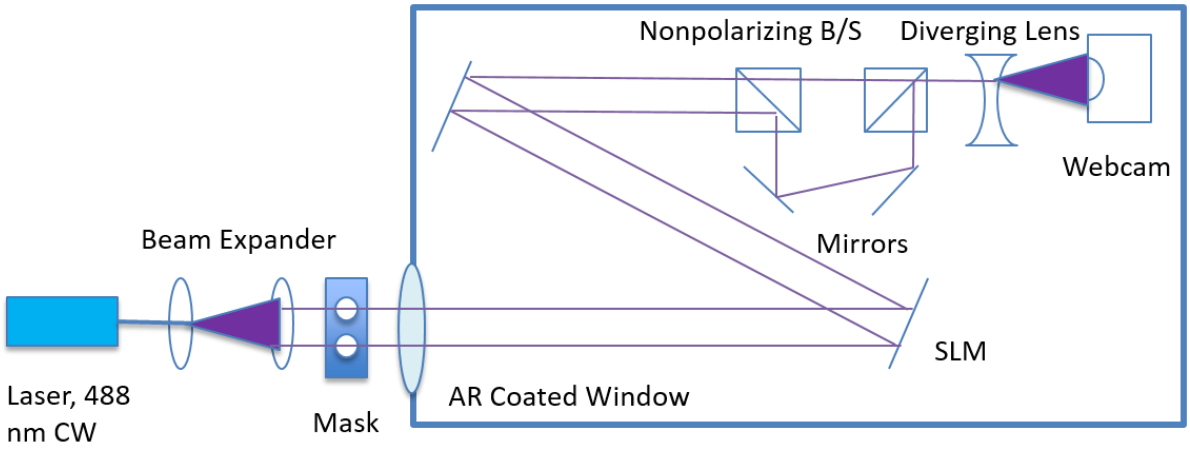

Figure 34. SLM calibration setup. Light reflecting from both halves of the SLM was used to form the two beams of an interferometer. The location of the interference fringes was a function of voltage applied to the SLM.

was expanded to illuminate the entire SLM screen and the reflections from the left and right halves of the SLM screen were combined to produce an interference pattern on a webcam sensor. The voltage applied to one half of the screen was varied between the maximum and minimum values which were programmed onto the SLM unit's EPROM.

The intensity of interference fringes at each pixel along a horizontal line was monitored while varying applied voltage from the minimum to the maximum allowable values. The maximum and minimum allowable voltages were modified until the resulting fringe shift was a full cycle (2π) with a linear relationship. By altering the range of voltages, a linear relationship between applied signal and phase delay was established as shown in figure 35.

Figure 35. Left: SLM calibration interference fringes, horizontal line along which fringe position was observed. Right: linear response of fringe position to applied voltage. Voltage increasing from minimum to maximum from top of image to bottom.

In order to establish positive control of the incident wavefront, two previously published experimental results were reproduced which relied upon wavefront phase control using a reflective SLM. These experiments included focusing light through an opaque medium [13], [14], [25] and imaging using correlation [38].

In addition, the experimental setup for focusing light through an opaque medium was slightly modified to produce two new results. Focusing backscattered light was demonstrated, which was (at the time of this experiment) a geometry in which focusing using a phase optimization method had not been attempted. Overall transmission of light through a sample was also slightly improved using a phase optimization method.

Focusing through opaque media by wavefront phase optimization was first demonstrated in 2007 by I.M. Vellekoop and A.P. Mosk [13]. In this experiment, the signal beam from a coherent source (OPSL) was reflected from the surface of an SLM. A microscope objective was then used to image this wavefront on the surface of a sample (paper and a 600 grit ground glass diffuser). A second microscope objective was used to image the back surface of the sample onto a CCD camera sensor. Just as in the original experiment, the phase delay of the wavefront was altered in systematic fashion while observing the intensity of the intended focus at the camera. The phase which resulted in the greatest amount of power at the camera was considered the optimum phase for that segment of the SLM and its value was recorded and displayed on the SLM after all segments were optimized.

This resulted in a significant improvement in measured intensity at the focal point of up to 5 times. Although intensity increases of 1000 times or more were previously reported for such an experiment [13], fine-tuning the process in order to achieve a greater improvement factor was not a goal of this reproduction. It was apparent that a greater improvement could have been achieved if necessary, but demonstrating control of the signal wavefront phase was the only outcome that was intended. Also, the dynamic range of the CCD limited the maximum improvement possible without dynamically altering the power of the signal beam during the optimization process. Without such a setup in place, the intensity improvement routinely caused the CCD electron counts to reach saturation so that no further gain could be observed.

The CCD was then placed so that it could record backscattered light from the sample. A desired focal point was selected with the backscatter and the phase optimization process was repeated, successfully focusing the backscattered light. The results of this experiment are discussed in greater detail in 3.3.

Using the same setup yet again, the camera was placed so that it could detect light on the far side of the sample. Rather than focus the light, however, the intention was to improve the total power of light delivered to the camera sensor using phase optimization. The intensity of light falling on all pixels of the camera sensor was summed, and the phase optimization process repeated while maximizing the total power. The result was an increase in the total counts by up to 13%.

Finally, resilience of focusing solutions to an angular offset (a prism phase function added to the phase delay imparted by the SLM) was tested. This was a demonstration of a principle first demonstrated by Katz *et. al.* [40]. The experiment setup was the same as that used for focusing through an opaque sample using phase optimization, except that after completion of the phase optimization a linearly increasing phase function was overlaid on top of the phase mask displayed on the SLM to achieve the focus. The results of this experiment are shown in figure 36. This demonstrates that a focus can be moved a small distance within the material by changing the incident angle of the incident wavefront, which is of great interest for imaging a small volume or for delivering therapeutic light energy to a small extended piece of tissue.

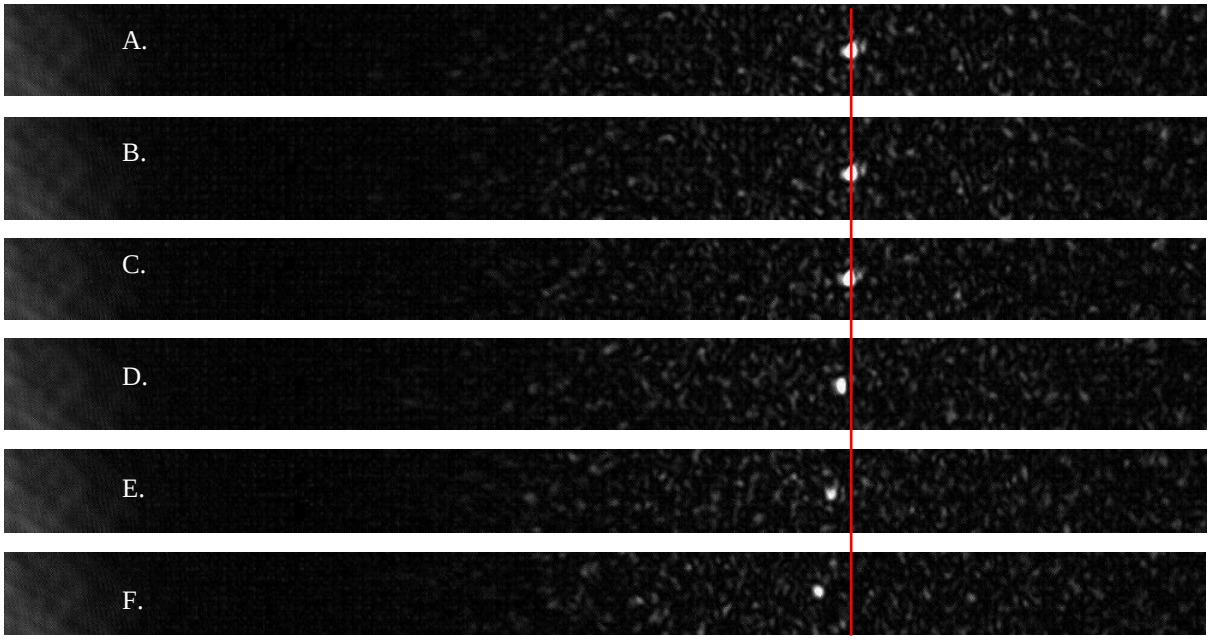

Figure 36. Incident light was focused through a scattering sample using wavefront optimization methods with direct feedback from the intended focus (A). A linearly increasing phase function which increased from right to left was then added to the SLM phase mask solution for focusing. The slope of the phase function is 0.1 cycles over the full 1920 SLM pixels (B), 0.5 (C), 1.5 (D), 3.0 (E), and 5.0 (F). The focus remains intact despite these changes, but shifts slightly to the left.

The experiments discussed in this section definitively demonstrated control of the signal wavefront. This allowed pursuit of the goal of increasing transmission through a strongly scattering medium (3.2) with confidence that the SLM would perform as expected.

Appendix 3: Calibration and Testing of Electro-Optic Modulator

The EOM used in the transmission enhancement experiment (3.2) and for focusing backscattered light by phase optimization (3.3) was a MgO doped $LiNbO_3$ crystal (Thorlabs EO-PM-NR-C4). Application of a voltage along the optical axis of the crystal induces a change in the index of refraction for light polarized along the extraordinary axis of the crystal, resulting in a phase delay proportional to the applied voltage. Maximum applied voltage for the crystal was +/- 200 V. This signal was produced by feeding a control voltage ranging +/- 10 V into a high voltage amplifier. Documentation for the EOM stated that the approximate voltage for a 2π phase shift for 488 nm light was 10 Volts. However, since the accuracy of the imparted phase shift was critical for accurately measuring the signal beam phase profile, a more precise knowledge of the relationship between applied voltage and phase delay was needed.

The relationship between applied voltage and phase delay was determined using a simple Mach-Zender interferometer with one of the two beams passing through the EOM (figure 37). The CW

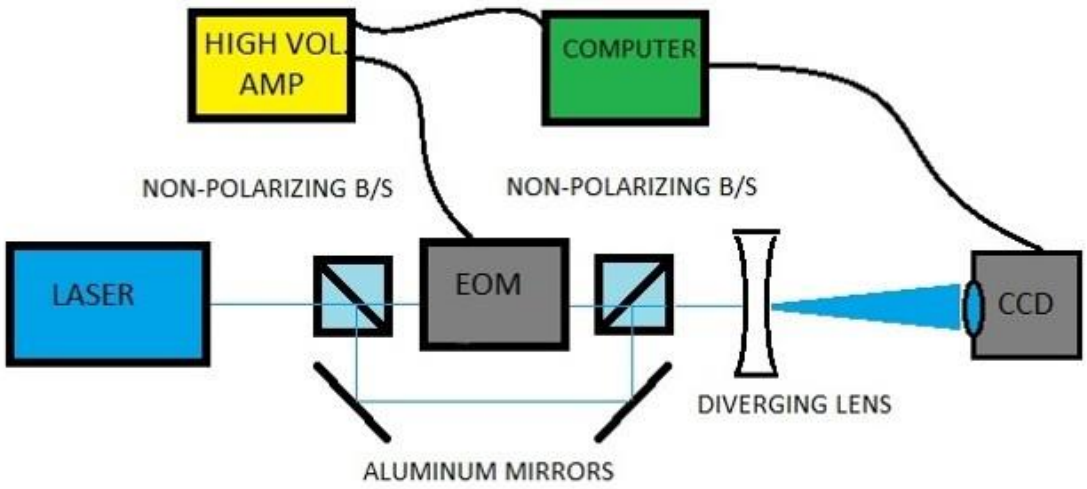

Figure 37. Schematic of electro-optical modulator calibration setup. A Mach-Zender interferometer was formed with one beam passing through the modulator. The interference fringe locations were recorded by the camera. The relationship between applied voltage and fringe location was recorded.

source was an OPSL (Coherent Sapphire 488 nm). The source beam was split by the first beamsplitter into signal and reference beams. The signal beam was passed through the EOM. Both beams were recombined at the second beamsplitter before passing through a diverging lens and falling on the sensor of a CCD camera (Andor iXon 885). The beam divergence and CCD camera distance were adjusted so that a few vertically oriented interference fringes filled the sensor.

The intensity of the interference pattern was measured along a horizontal line of pixels on the sensor. As the voltage input to the EOM was altered, the position of the interference fringes shifted on the sensor. Using 10 V as a starting point for the peak-to-peak control signal voltage, a signal was applied to the EOM and the voltage was shifted until it caused a shift in the fringe pattern of one cycle. This voltage change was taken to be the correct amount to provide a full 2π phase shift. Since shifts of $\pi/2$ were necessary in the experiment, this voltage was divided by four to give the $\pi/2$ voltage change that would be used.

It is worth noting that the EOM did not respond well to DC signals to accomplish the necessary phase shift. The shift was to be held long enough to record the resulting interference pattern on

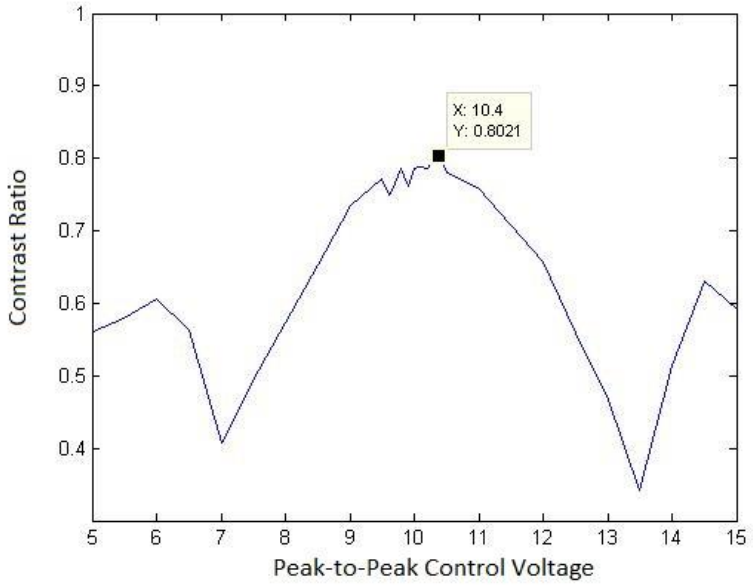

Figure 38. EOM Calibration curve. Contrast ratio of bright and dark interference fringes versus voltage.

the CCD sensor which could be as long as 100-200 ms (though the camera was capable of full frame rates of up to 30 fps, delays resulting from coordination of all components of the experiment from a common National Instruments LabView Virtual Instrument (VI) often lengthened the necessary time well beyond 33 ms). A significant shift in phase delay over time was consistently observed when a DC signal was applied and held constant on the EOM. The EOM responded more consistently to a changing signal than it did to a DC signal. Instead of a DC signal, a slowly varying square wave signal (100-1000 Hz) was applied to the EOM with a peak-to-peak amplitude equal to the full wave voltage. The EOM received a signal that switched between two control voltages which should have produced a phase delay difference of about 2π. When the difference between the two control voltages is an exact match for the full wave voltage, the location of the interference fringes will not change over time. The resulting phase delay was only momentarily different from the desired value during the rising and falling edge of the square wave (which represented a very small portion of the waveform in time). The exposure time of the data taken with the CCD camera was long enough to average out data over at least ten cycles of the input square wave so that this momentary shift in phase delay during the rising

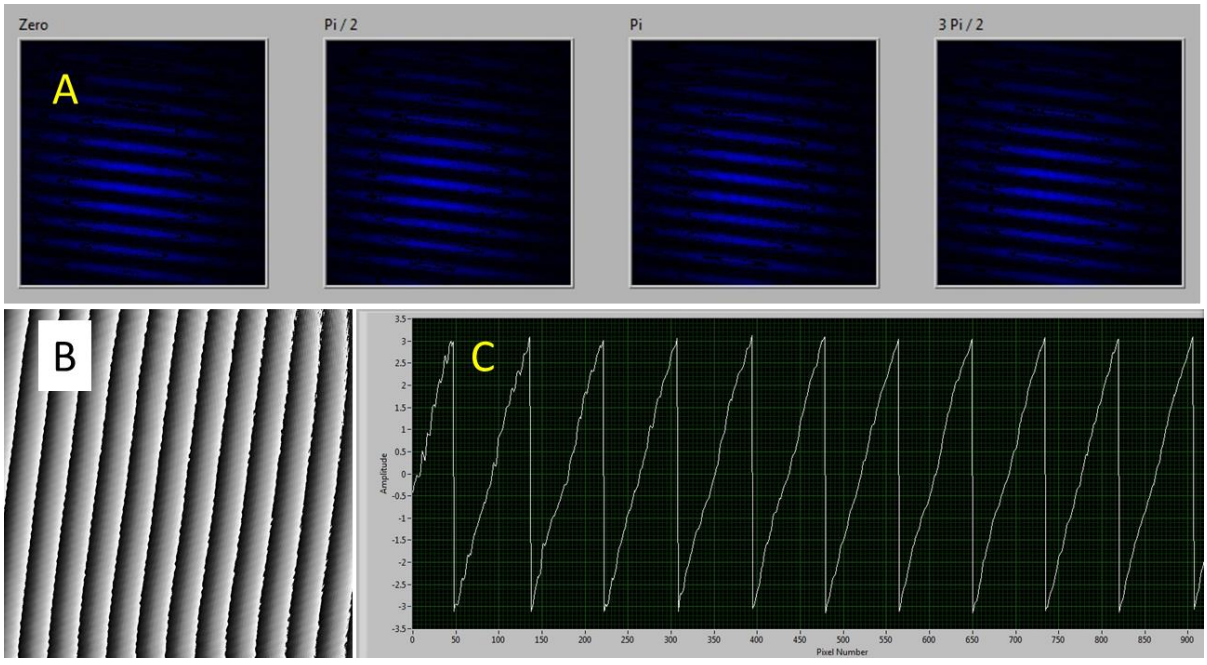

Figure 39. A. Images of the interference pattern created with the Mach-Zender interferometer, with different phases set by the EOM in the reference beam. B. The calculated phase of the signal beam. C. The phase of the signal along a horizontal line drawn through the image in B. This saw tooth pattern matches the expected pattern of linear phase increase.

and falling edge of the applied voltage square wave did not have a significant effect on the measured intensity at a given pixel.

In order to tune the peak-to-peak amplitude of the control voltage to a 2π phase shift, the contrast ratio of the bright and dark fringes displayed in the collected images on the CCD sensor was calculated. The peak-to-peak voltage was shifted to maximize the contrast ratio. When the phase shift was not equal to a full cycle, the contrast ratio between the bright and dark fringes decreased. The voltage change that resulted in the maximum contrast ratio was determined to provide the closest to a 2π phase shift (figure 38).

Once the EOM was calibrated, the same setup was used to make test measurements of a wavefront phase profile using phase shifting digital holography. In order to test the accuracy of the phase profile measurement, an interference pattern with a known phase profile was imaged on the camera sensor. The digital holographic recording method was used to measure the phase profile and the measured profile was compared with the known profile. The EOM was used to impart a phase delay to the signal arm in increments of $\pi/2$ to the signal arm, and an image of the interference pattern was recorded at each phase delay such that one image was recorded for 0, $\pi/2$, π, and $3\pi/2$ delay.

Equation 45 was applied to the recorded data to calculate the phase of the measured wavefront. In order to produce the interference pattern, the reference and signal beam were given a small tilt relative to one another in the horizontal plane. The expected phase profile in this plane was therefore a simple linear function with a slope defined by the number of wavelengths of optical path difference (obtained by counting the number of bright and dark fringe cycles in the pattern) and the width of the CCD sensor. Due to limiting the phase difference to a range of 0 to 2π, the expected output was a saw tooth pattern with spatial frequency equal to the spatial frequency of the interference fringes. Figure 39 shows that the result of this test matched the expected result, indicating that the EOM had operated as expected and that the phase-shifting digital holography method of phase measurement had been successfully employed.

Appendix 4: Measuring Signal Phase Profile with Phase-shifting Digital Holography

The phase profile of the signal wavefront was measured using phase-shifting digital holography [55]. This is a means of measuring and recording the phase using a digital camera. Interference between the signal beam, with unknown phase, and a reference beam, with known phase, is recorded four times with the reference beam changing phase each time. The recorded intensity information is adequate to calculate the unknown phase profile of the signal wavefront. The reference beam phase may be controlled with any device capable of imparting an arbitrary phase delay to the beam, but for enhancing the transmission of light (section 3.2) an electro-optic modulator was used to control the reference phase.

The reference beam and signal beam combine at the camera sensor plane. The two electromagnetic fields, which must be polarized in the same direction, combine as in equation 39. The intensity of these two combined fields is described by equation 40.

$$E_{tot} = E_r e^{i\phi_r} + E_s e^{i\phi_s} \tag{39}$$

$$I_{tot} = E_{tot}^* E_{tot} = |E_r|^2 + |E_s|^2 + 2|E_r||E_s|\cos(\Delta\phi) \tag{40}$$

$$I_1 = |E_r|^2 + |E_s|^2 + 2|E_r||E_s|\cos(\Delta\phi) \tag{41}$$

$$I_2 = |E_r|^2 + |E_s|^2 + 2|E_r||E_s|\cos(\Delta\phi + \pi/2) \tag{42}$$

$$I_3 = |E_r|^2 + |E_s|^2 + 2|E_r||E_s|\cos(\Delta\phi + \pi) \tag{43}$$

$$I_4 = |E_r|^2 + |E_s|^2 + 2|E_r||E_s|\cos(\Delta\phi + 3\pi/2) \tag{44}$$

$$\phi_s = \tan^{-1}\left(\frac{I_4 - I_2}{I_1 - I_3}\right) \tag{45}$$

The intensity values on the left hand side of equations 41-44 are gathered by shifting the phase of the reference wave using an electro-optic modulator (Thorlabs EO-PM-NR-C4) and recording interference pattern intensity on the CCD sensor. The phase is then calculated using data from the four images using equation 45.

It is possible to measure phase information of the signal by recording fewer than four interference patterns with different respective reference beam phase. However, the alternative methods that use fewer reference beam phase shifts require greater precision in the flatness of the reference beam and uniform intensity. By recording the interference pattern for all four reference beam phase delays, the experiment was made slightly less sensitive to imperfections in the reference beam. The phase delay was imparted on reference beam using an electro-optic modulator (EOM) in $\pi/2$ increments.

The accuracy of the signal beam phase profile measurement depends on the precision of the $\pi/2$ phase delay. The precision requirement of the phase delay made it necessary to perform thorough calibration and testing of the EOM prior to use. Phase shifting digital holography, the method used to measure the phase of the wavefront at the camera, requires a reference beam to form an interference pattern at the camera sensor when overlapped with the signal beam. Information about the phase of the signal is gathered from the variations in the intensity of the interference pattern as the phase of the reference beam is shifted in phase relative to the signal by 0, $\pi/2$, π, and $3\pi/2$.

Appendix 5: Selecting Polarization for Suppression of Singly Scattered and Reflected Light

Multiple scattering of light as it propagates through a material with densely packed scattering centers causes randomization of the direction of travel, phase, and polarization [52]. The number of scattering events after which the direction of the travel is randomized is known as the transport mean free path length [52]. The average length of propagation of light that is required in order to randomize the polarization of light is of interest for this experiment. This length is different for linear and circularly polarized light, and is also affected by the size of the scattering centers with respect to the wavelength of the light [52]. In the experiments discussed here, it is desirable to ignore light that is directly reflected from the surface of a sample and photons experiencing a reversal in path from in a single scattering event. It is intended to make measurements only of the light which has been backscattered through multiple scattering events. This light travels deeper into the sample in question. It has been shown that circularly polarized light maintains its polarization, on average, for a much greater propagation distance than the transport mean free path in the multiple scattering regime [52]. The chirality of this polarization is reversed when the light is reflected back from a surface (e.g., right hand circularly polarized (RHCP) light becomes left hand circularly polarized (LHCP) light) or backscattered after a single scattering event.

Control of polarization is therefore critical to this experiment so that only the photons traveling deep into the sample are selected. In addition, reflections from optics in the system which tend to be strong enough to overpower the backscattered light from the sample can be greatly reduced. The incident light is polarized horizontally, but is converted to RHCP light by means of a quarter wave plate before reaching the sample. Light that is reflected from the surface of the sample becomes LHCP, as does light that is backscattered in a single scattering event and reflections from lenses and other optics. Upon re-entering the quarter wave plate, both RHCP and LHCP light are converted to linearly polarized light separated by of 90 degrees. The LHCP light is then filtered out as the light passes through a linear polarizer before reaching the CCD sensor, greatly reducing the amount of light falling on the CCD from reflections and single scattering events.

The Jones matrix Q in equation 46 represents a quarter wave plate with angle θ of the fast axis to the horizontal, and the vector V of the initially horizontally polarized light vector is shown in equation 47.

$$Q = e^{i\frac{\pi}{4}}\begin{pmatrix} cos^2\theta + i\ sin^2\theta & (1-i)sin\theta cos\theta \\ (1-i)sin\theta cos\theta & i\ cos^2\theta + \ sin^2\theta \end{pmatrix} \tag{46}$$

$$V = \begin{pmatrix} 1 \\ 0 \end{pmatrix} \tag{47}$$

$$V_{out} = QV = \ e^{i\frac{\pi}{4}}\begin{pmatrix} cos^2\theta + i\ sin^2\theta \\ (1-i)sin\theta cos\theta \end{pmatrix} \tag{48}$$

When θ is set to 45 degrees, $\boldsymbol{V_{out}}$ becomes $(\mathbf{1} \quad -\boldsymbol{i})^{\boldsymbol{T}}$ (ignoring the constant coefficient), or RHCP. Upon reflection, this light becomes LHCP, represented by the column vector $(\mathbf{1} \quad \boldsymbol{i})^{\boldsymbol{T}}$. Upon passage back through the same quarter wave plate, the polarization of the RHCP and LHCP light is converted to $(\mathbf{0} \quad \mathbf{1})^{\boldsymbol{T}}$ and $(\mathbf{1} \quad \mathbf{0})^{\boldsymbol{T}}$, respectively. Placing a polarizer in the path of the signal with vertical transmission axis therefore transmits the light which is multiply scattered and maintains (on average) its original chirality of polarization while blocking the reflected and singly scattered light.

Polarization control is also critical to the measurement of the signal phase. In order to measure the phase of the light at the CCD sensor, a plane wave reference beam which is linearly vertically polarized is combined with the signal beam. This creates a pattern of constructive and destructive interference on the CCD sensor which is used to calculate the phase of the signal (see the following section on phase-shifting digital holography). Only two signals polarized in the same direction will interfere.

Appendix 6: Holographic Wavefront Propagation

The search for the optimal wavefront shape is conducted using an algorithm based upon the steepest descent method for finding extreme values within a function [15], [49]. To implement the algorithm, the wavefront exiting the sample is time-reversed and directed back along the same path into the sample. In order to accomplish this, the phase profile of the wavefront exiting the sample must first be measured. After the phase measurement, a phase conjugated version of the wavefront is produced and sent back into the sample (time-reversal). Phase measurement of the light and phase-conjugation of the wavefront were performed at locations separated from the sample by a distance on the order of a meter. The wavefront must travel between the three elements responsible for these processes.

This propagation introduces phase differences in the wavefront that evolve as the wave travels. While a perfect plane wave will only experience diffraction during propagation, a wavefront

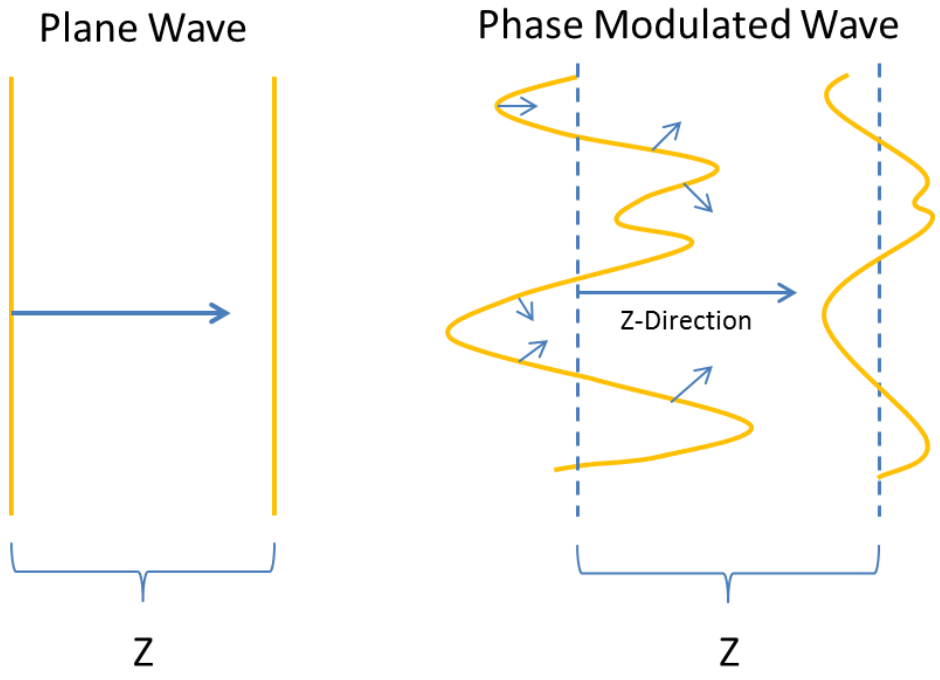

Figure 40. Left: A plane wave propagates along the z-direction, ignoring the effects of diffraction. The surface of equal phase does not change shape. Right: A spatially phase-modulated wavefront has a surface of equal phase that changes shape, which is described by angular spectrum propagation.

which is spatially phase modulated will change shape during propagation. In accordance with Huygens' Principle, each point on the wavefront can be treated as a point source of light and the total wavefront is found by integrating the effects of each point source over the entire wavefront. Phase delays or advances at each of these point sources change the shape of the envelope of the advancing wave, and the energy flow at each point is no longer strictly in along the z-axis as shown in figure 40.

For any application that involves knowing or manipulating the relative phase delays of a wavefront, its propagation must be accounted for. When measuring the phase of a wavefront a given distance z_1 from the location at which information is desired, the wavefront must be constructed using the measured phases and then propagated backward to the point of interest.

Similarly, if it is desired to shape the incident wavefront at the surface of the sample, the distance traveled between our SLM and the sample, z_2, must be considered. After choosing the shape of the incident wavefront that is desired at the sample surface, the desired wave must be constructed and propagated back to the SLM mathematically to find the phase delay that must be imparted at each segment of the SLM.

It is worth noting that the pixel size of the CCD sensor in this experiment is equal to the pixel size of the SLM so that we can match sections of both the backscattered and incident wavefronts point for point. Incidentally, this also requires alignment of the signal reflected from the SLM to the CCD sensor. In this series of experiments alignment was accomplished by displaying a diffractive optical element (a lens) on the SLM and placing the resulting focal point of the light at the center of the CCD sensor (after passage through the optical system).

In order to propagate a wavefront mathematically, it must first have a mathematical description. The wavefront can be described by its angular spectrum [22] as in equation 49.

$$U(x,y,0) = \iint_{-\infty}^{\infty} A(f_x, f_y; 0) e^{-2\pi i(f_x x + f_y y)} df_x df_y \qquad (49)$$

This completely describes the wavefront at z = 0 in terms of a sum of plane waves traveling at all possible angles with respect to the optical axis. Given that the angles of propagation with respect to the x, y, and z axes are a, b, and c, we can relate the spatial frequencies along the three axes by the direction cosines of each angle as in equation 50, where Greek symbols represent the cosine of each angle (see figure 41).

$$\alpha^2 + \beta^2 + \gamma^2 = 1 \tag{50}$$

Since $f_x = \frac{\alpha}{\lambda}$ (and likewise for each respective direction), we can rewrite this in terms of frequencies.

$$f_x{}^2 + f_y{}^2 + f_z{}^2 = \frac{1}{\lambda^2} \tag{51}$$

$$f_z = \frac{1}{\lambda}\sqrt{1 - (\lambda f_x)^2 + (\lambda f_y)^2} \tag{52}$$

Now, describing the wavefront at any point z on the optical axis:

$$U(x, y, z) = \iint_{-\infty}^{\infty} A(f_x, f_y; z) e^{2\pi i (f_x x + f_y y)} df_x df_y \tag{53}$$

We also know that U must satisfy the Helmholtz equation in the absence of sources (which we can safely assume in the system of this experiment).

$$\nabla^2 U + k^2 U = 0 \tag{54}$$

Applying this to U(x,y,z):

$$\frac{d^2}{dz^2} A\left(f_x, f_y; z\right) + \frac{4\pi^2}{\lambda^2}\left(1 - (\lambda f_x)^2 - \left(\lambda f_y\right)^2\right) A\left(f_x, f_y; z\right) = 0 \tag{55}$$

This differential equation has the simple solution:

$$A(x,y,z) = A(x,y,0)e^{\frac{2\pi iz}{\lambda}\left(\sqrt{1-(\lambda f_x)^2-\left(\lambda f_y\right)^2}\right)} \tag{56}$$

Note that for $(1-(\lambda f_x)^2-\left(\lambda f_y\right)^2) < 0$, the exponent becomes a negative real number and the spectral amplitude *A* drops off exponentially as z increases. This type of wave is called an evanescent wave and it does not propagate along the optical axis. However, we must place limits on our calculations that exclude these waves.

Finally, we can write U as an inverse Fourier transform of the spectral amplitudes at z:

$$U(x,y,z) = \iint_{-\infty}^{\infty} A(f_x,f_y;z)e^{2\pi i(f_x x+f_y y)}e^{-\frac{2\pi iz}{\lambda}\left(\sqrt{1-(\lambda f_x)^2-(\lambda f_y)^2}\right)}df_x df_y \tag{57}$$

The integrals here are limited to the region in frequency space where the radical is a real number, eliminating the evanescent waves.

In the final geometry of this experiment (after several versions were built, broken down and rebuilt), the propagation distance between the SLM and the surface of the sample, and between the surface of the sample and the CCD sensor were designed to be equal. In this special configuration, the propagation did not need to be accounted for as long as the wavefront produced at the SLM was the conjugate of the wavefront measured at the CCD sensor. Because the distances are equal, this is equivalent to time-reversing the wavefront at the CCD sensor and the evolution of its shape as it travels toward the sample is precisely the opposite of its evolution as it travels away from the sample toward the camera. Therefore by using the SLM to produce a phase-conjugated version of the wavefront sensed at the camera, the wavefront that enters the sample is a time-reversed version of the wavefront exiting the sample in the backscatter direction. Despite this special configuration, it is important to be cognizant of the effects of wavefront propagation in any design of such an experiment.

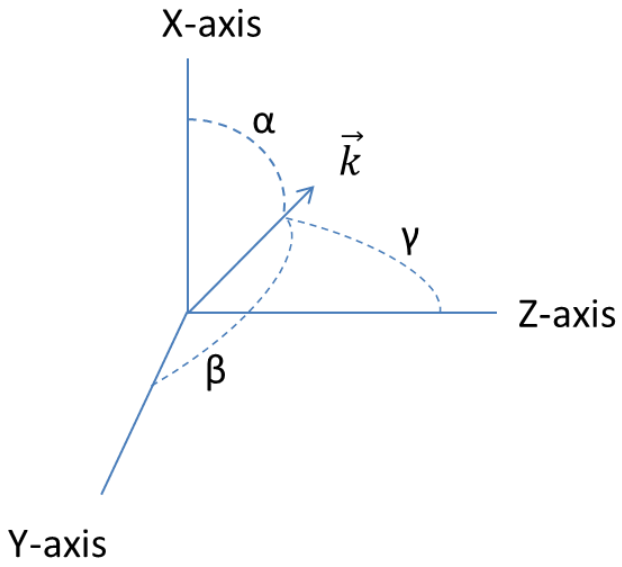

Figure 41. Direction cosines for the k-vector of a plane wave with angles a, b, and c with respect to the x, y, and z axes, respectively.

References

[1] Y. M. Wang, B. Judkewitz, C. A. DiMarzio, and C. Yang, "Deep-tissue focal fluorescence imaging with digitally time-reversed ultrasound-encoded light," *Nat. Commun.*, vol. 3, p. 928, Jun. 2012.

[2] D. Chen, B. Li, S. Cai, P. Wang, S. Peng, Y. Sheng, Y. He, Y. Gu, and H. Chen, "Dual targeting luminescent gold nanoclusters for tumor imaging and deep tissue therapy," *Biomaterials*, vol. 100, pp. 1–16, Sep. 2016.

[3] S. J. Beebe, W. E. Ford, W. Ren, X. Chen, and K. H. Schoenbach, "Non-ionizing radiation with nanosecond pulsed electric fields as a cancer treatment: in vitro studies," in *2009 Annual International Conference of the IEEE Engineering in Medicine and Biology Society*, 2009, pp. 6509–6512.

[4] P. Wizinowich, "Adaptive optics in astronomy," *Contemp. Phys.*, vol. 56, no. 4, pp. 432–450, Jun. 2015.

[5] D. L. C. Narcisse, S. T. Fiorino, and R. J. Bartell, "Optimizing the Effectiveness of Directed Energy Weapons with Specialized Weather Support," *Air Space Power J.*, vol. 23, no. 2, pp. 57–66, Summer 2009.

[6] C. Brunner, T. Peynot, T. Vidal-Calleja, and J. Underwood, "Selective Combination of Visual and Thermal Imaging for Resilient Localization in Adverse Conditions: Day and Night, Smoke and Fire: Resilient Localisation in Adverse Conditions," *J. Field Robot.*, vol. 30, no. 4, pp. 641–666, Jul. 2013.

[7] E. Leitgeb, T. Plank, M. Loschnigg, and P. Mandl, "Free space optics in different (civil and military) application scenarios in combination with other wireless technologies," 2014, pp. 1–7.

[8] J. Tang, R. N. Germain, and M. Cui, "Superpenetration optical microscopy by iterative multiphoton adaptive compensation technique," *Proc. Natl. Acad. Sci.*, vol. 109, no. 22, pp. 8434–8439, May 2012.

[9] L. Kong and M. Cui, "In Vivo Deep Tissue Imaging via Iterative Multiphoton Adaptive Compensation Technique," *IEEE J. Sel. Top. Quantum Electron.*, vol. 22, no. 4, pp. 1–10, Jul. 2016.

[10] X. Tao, O. Azucena, M. Fu, Y. Zuo, D. C. Chen, and J. Kubby, "Adaptive optics confocal microscopy using fluorescent protein guide-stars for brain tissue imaging," 2012, p. 82530M.

[11] I. M. Vellekoop, M. Cui, and C. Yang, "Digital optical phase conjugation of fluorescence in turbid tissue," *Appl. Phys. Lett.*, vol. 101, no. 8, p. 81108, Aug. 2012.

[12] M. Cui and C. Yang, "Implementation of a digital optical phase conjugation system and its application to study the robustness of turbidity suppression by phase conjugation," *Opt. Express*, vol. 18, no. 4, p. 3444, Feb. 2010.

[13] I. M. Vellekoop and A. P. Mosk, "Focusing coherent light through opaque strongly scattering media," *Opt. Lett.*, vol. 32, no. 16, pp. 2309–2311, Aug. 2007.

[14] A. P. Mosk, A. Lagendijk, G. Lerosey, and M. Fink, "Controlling waves in space and time for imaging and focusing in complex media," *Nat. Photonics*, vol. 6, no. 5, pp. 283–292, May 2012.

[15] C. Jin, R. R. Nadakuditi, E. Michielssen, and S. C. Rand, "Backscatter analysis based algorithms for increasing transmission through highly scattering random media using phase-only-modulated wavefronts," *J. Opt. Soc. Am. A*, vol. 31, no. 8, p. 1788, Aug. 2014.

[16] X. Xu, H. Liu, and L. V. Wang, "Time-reversed ultrasonically encoded optical focusing into scattering media," *Nat Photon*, vol. 5, no. 3, pp. 154–157, Mar. 2011.
[17] M. J. Purcell, M. Kumar, S. C. Rand, and V. Lakshminarayanan, "Holographic imaging through a scattering medium by diffuser-aided statistical averaging," *J. Opt. Soc. Am. A*, vol. 33, no. 7, p. 1291, Jul. 2016.
[18] A. K. Singh, D. N. Naik, G. Pedrini, M. Takeda, and W. Osten, "Looking through a diffuser and around an opaque surface: A holographic approach," *Opt. Express*, vol. 22, no. 7, p. 7694, Apr. 2014.
[19] M. J. Purcell, M. Kumar, and S. C. Rand, "Holographic imaging through a scattering medium by diffuser-assisted statistical averaging," 2016, vol. 9771, p. 97710F–97710F–7.
[20] E. Ash, "Dennis Gabor, 1900-1979," *Nature*, vol. 280, pp. 431–433, Aug. 1979.
[21] S. A. Benton and V. M. Bove, "Off-Axis 'Leith & Upatnieks' Holography," in *Holographic Imaging*, John Wiley & Sons, Inc., 2008, pp. 103–113.
[22] J. W. Goodman and R. Gustafson Steven C., "Introduction to Fourier Optics, Second Edition," *Opt. Eng.*, vol. 35, no. 5, pp. 1513–1513, 1996.
[23] L. Repetto, F. Pellistri, E. Piano, and C. Pontiggia, "Gabor's hologram in a modern perspective," *Am. J. Phys.*, vol. 72, no. 7, p. 964, 2004.
[24] O. N. Dorokhov, "On the coexistence of localized and extended electronic states in the metallic phase," *Solid State Commun.*, vol. 51, no. 6, pp. 381–384, Aug. 1984.
[25] I. M. Vellekoop and A. P. Mosk, "Phase control algorithms for focusing light through turbid media," *Opt. Commun.*, vol. 281, no. 11, pp. 3071–3080, Jun. 2008.
[26] E. N. Leith and J. Upatnieks, "Holographic Imagery Through Diffusing Media," *J. Opt. Soc. Am.*, vol. 56, no. 4, p. 523, Apr. 1966.
[27] Z. Yaqoob, D. Psaltis, M. S. Feld, and C. Yang, "Optical phase conjugation for turbidity suppression in biological samples," *Nat. Photonics*, vol. 2, no. 2, pp. 110–115, Feb. 2008.
[28] J. W. Goodman, "Wavefront-Reconstruction Imaging Through Random Media," *Appl. Phys. Lett.*, vol. 8, no. 12, p. 311, 1966.
[29] E. Leith, C. Chen, H. Chen, Y. Chen, D. Dilworth, J. Lopez, J. Rudd, P.-C. Sun, J. Valdmanis, and G. Vossler, "Imaging through scattering media with holography," *J. Opt. Soc. Am. A*, vol. 9, no. 7, p. 1148, Jul. 1992.
[30] M. A. Duguay and A. T. Mattick, "Ultrahigh Speed Photography of Picosecond Light Pulses and Echoes," *Appl. Opt.*, vol. 10, no. 9, p. 2162, Sep. 1971.
[31] N. Abramson, "Light-in-flight recording by holography," *Opt. Lett.*, vol. 3, no. 4, p. 121, Oct. 1978.
[32] N. H. Abramson and K. G. Spears, "Single pulse light-in-flight recording by holography," *Appl. Opt.*, vol. 28, no. 10, p. 1834, May 1989.
[33] E. Leith, H. Chen, Y. Chen, D. Dilworth, J. Lopez, R. Masri, J. Rudd, and J. Valdmanis, "Electronic holography and speckle methods for imaging through tissue using femtosecond gated pulses," *Appl. Opt.*, vol. 30, no. 29, p. 4204, Oct. 1991.
[34] M. Cui, "Parallel wavefront optimization method for focusing light through random scattering media," *Opt. Lett.*, vol. 36, no. 6, p. 870, Mar. 2011.
[35] D. B. Conkey, A. N. Brown, A. M. Caravaca-Aguirre, and R. Piestun, "Genetic algorithm optimization for focusing through turbid media in noisy environments," *Opt. Express*, vol. 20, no. 5, p. 4840, Feb. 2012.

[36] Y. Liu, P. Lai, C. Ma, X. Xu, A. A. Grabar, and L. V. Wang, “Optical focusing deep inside dynamic scattering media with near-infrared time-reversed ultrasonically encoded (TRUE) light,” *Nat. Commun.*, vol. 6, p. 5904, Jan. 2015.
[37] F. Helmchen and W. Denk, “Deep tissue two-photon microscopy,” *Nat. Methods*, vol. 2, no. 12, pp. 932–40, Dec. 2005.
[38] I. Freund, “Looking through walls and around corners,” *Phys. Stat. Mech. Its Appl.*, vol. 168, no. 1, pp. 49–65, Sep. 1990.
[39] J. Bertolotti, E. G. van Putten, C. Blum, A. Lagendijk, W. L. Vos, and A. P. Mosk, “Non-invasive imaging through opaque scattering layers,” *Nature*, vol. 491, no. 7423, pp. 232–4, Nov. 2012.
[40] O. Katz, P. Heidmann, M. Fink, and S. Gigan, “Non-invasive single-shot imaging through scattering layers and around corners via speckle correlations,” *Nat. Photonics*, vol. 8, no. 10, pp. 784–790, Aug. 2014.
[41] S. Kang, S. Jeong, W. Choi, H. Ko, T. D. Yang, J. H. Joo, J.-S. Lee, Y.-S. Lim, Q.-H. Park, and W. Choi, “Imaging deep within a scattering medium using collective accumulation of single-scattered waves,” *Nat. Photonics*, Mar. 2015.
[42] R. Kumar Singh, V. R. V., and A. Sharma M., “Recovery of complex valued objects from two-point intensity correlation measurement,” *Appl. Phys. Lett.*, vol. 104, no. 11, p. 111108, Mar. 2014.
[43] G. W Joseph, *Statistical optics / Joseph W. Goodman*. New York: Wiley, 1985.
[44] Z. Wang, A. C. Bovik, H. R. Sheikh, and E. P. Simoncelli, “Image quality assessment: from error visibility to structural similarity,” *IEEE Trans. Image Process.*, vol. 13, no. 4, pp. 600–612, Apr. 2004.
[45] P. C. Teo and D. J. Heeger, “Perceptual image distortion,” 1994, vol. 2179, pp. 127–141.
[46] “Mathworks,” *MathWorks*. [Online]. Available: www.mathworks.com. [Accessed: 29-Jun-2016].
[47] W. Choi, A. P. Mosk, Q.-H. Park, and W. Choi, “Transmission eigenchannels in a disordered medium,” *Phys. Rev. B*, vol. 83, no. 13, Apr. 2011.
[48] C. Jin, R. R. Nadakuditi, E. Michielssen, and S. Rand, “An iterative, backscatter-analysis based algorithm for increasing transmission through a highly-backscattering random medium,” 2012, pp. 97–100.
[49] C. Jin, R. R. Nadakuditi, E. Michielssen, and S. C. Rand, “Iterative, backscatter-analysis algorithms for increasing transmission and focusing light through highly scattering random media,” *J. Opt. Soc. Am. A*, vol. 30, no. 8, p. 1592, Aug. 2013.
[50] R. Corey, M. Kissner, and P. Saulnier, “Coherent backscattering of light,” *Am. J. Phys.*, vol. 63, no. 6, pp. 560–564, Jun. 1995.
[51] C. Barnes and J. B. Pendry, “Multiple Scattering of Waves in Random Media: A Transfer Matrix Approach,” *Proc. Math. Phys. Sci.*, vol. 435, no. 1893, pp. 185–196, 1991.
[52] F. C. MacKintosh, J. X. Zhu, D. J. Pine, and D. A. Weitz, “Polarization memory of multiply scattered light,” *Phys. Rev. B Rapid Commun.*, vol. 40, no. 13, pp. 9342–9345, Nov. 1989.
[53] *Laser Speckle and Related Phenomena*, vol. 9. Berlin, Heidelberg: Springer Berlin Heidelberg, 1975.
[54] A. Kuditcher, B. G. Hoover, M. P. Hehlen, E. N. Leith, S. C. Rand, and M. P. Shih, “Ultrafast, cross-correlated harmonic imaging through scattering media,” *Appl. Opt.*, vol. 40, no. 1, p. 45, Jan. 2001.

[55] I. Yamaguchi and T. Zhang, “Phase-shifting digital holography,” *Opt. Lett.*, vol. 22, no. 16, p. 1268, Aug. 1997.